Characterization and modeling of the human left atrium using optical coherence tomography

Theresa Huang Lye

Submitted in partial fulfillment of the

requirements for the degree

of Doctor of Philosophy

in the Graduate School of Arts and Sciences

COLUMBIA UNIVERSITY

2019

ABSTRACT

Characterization and modeling of the human left atrium using optical coherence tomography

Theresa Huang Lye

With current needs to better understand the interaction between atrial tissue microstructure and atrial fibrillation dynamics, micrometer scale imaging with optical coherence tomography has significant potential to provide further insight on arrhythmia mechanisms and improve treatment guidance. However, optical coherence tomography imaging of cardiac tissue in humans is largely unexplored, and the ability of optical coherence tomography to identify the structural substrate of atrial fibrillation has not yet been investigated. Therefore, the objective of this thesis was to develop an optical coherence tomography imaging atlas of the human heart, study the utility of optical coherence tomography in providing useful features of human left atrial tissues, and develop a framework for optical coherence tomography-informed cardiac modeling that could be used to probe dynamics between electrophysiology and tissue structure.

Human left atrial tissues were comprehensively imaged by optical coherence tomography for the first time, providing an imaging atlas that can guide identification of left atrial tissue features from optical coherence tomography imaging. Optical coherence tomography image features corresponding to myofiber and collagen fiber orientation, adipose tissue, endocardial thickness and composition, and venous media were established. Varying collagen fiber distributions in the myocardial sleeves were identified within the pulmonary veins. A scheme for mapping optical coherence tomography data of dissected left atrial tissues to a three-dimensional,

anatomical model of the human left atrium was also developed, enabling the mapping of distributions of imaged adipose tissue and fiber orientation to the whole left atrial geometry. These results inform future applications of structural substrate mapping in the human left atrium using optical coherence tomography-integrated catheters, as well as potential directions of *ex vivo* optical coherence tomography atrial imaging studies.

Additionally, we developed a workflow for creating optical mapping models of atrial tissue as informed by optical coherence tomography. Tissue geometry, fiber orientation, ablation lesion geometry, and heterogeneous tissue types were extracted from optical coherence tomography images and incorporated into tissue-specific meshes. Electrophysiological propagation was simulated and combined with photon scattering simulations to evaluate the influence of tissue-specific structure on electrical and optical mapping signals. Through tissue-specific modeling of myofiber orientation, ablation lesions, and heterogeneous tissue types, the influence of myofiber orientation on transmural activation, the relationship between fluorescent signals and lesion geometry, and the blurring of optical mapping signals in the presence of heterogeneous tissue types were investigated.

By providing a comprehensive optical coherence tomography image database of the human left atrium and a workflow for developing optical coherence tomography-informed cardiac tissue models, this work establishes the foundation for utilizing optical coherence tomography to improve the structural substrate characterization of atrial fibrillation. Future developments include analysis of optical coherence tomography imaged tissue structure with respect to clinical presentation, development of automated processing to better leverage the large amount of imaging data, enhancements and validation of the modeling scheme, and *in vivo* evaluation of the left atrial structural substrate through optical coherence tomography-integrated catheters.

Table of Contents

List of Abbreviations

$\Delta\lambda$ – bandwidth

θ_{max} – single-sided maximum scan angle

A-line – axial ine

CFAE – complex fractionated atrial electrogram

CT – computed tomography

DE-MRI – delayed-enhancement magnetic resonance imaging

DT-MRI – diffusion tensor magnetic resonance imaging

f – focal length

FD-OCT – Fourier domain optical coherence tomography

FOV_{axial} – axial field of view

$FOV_{lateral}$ – lateral field of view

FWHM – full-width half-maximum

g – anisotropy coefficient

I_{em} – fluorescent emission photon density

I_{ex} – normalized excitation photon denisty

LA – left atrium

LAA – left atrial appendage

LGE-MRI – late gadolinium enhanced magnetic resonance imaging

LIPV – left inferior pulmonary vein

LSPV – left superior pulmonary vein

LV – left ventricle

LVS – left ventricular septum

MRI – magnetic resonance imaging

n – refractive index

NA – numerical aperture

OCT – optical coherence tomography

RA – right atrium

RIPV – right inferior pulmonary vein

ROI – region of interest

RSPV – right superior pulmonary vein

RV – right ventricle

RVS – right ventricular septum

SD-OCT – spectral domain optical coherence tomography

SS-OCT – swept source optical coherence tomography

TTC – triphenyltetrazolium chloride

μ_a – absorption coefficient

μ_s – scattering coefficient

μ_t – attenuation coefficient

V_f^* – fractional level of maximum optical upstroke velocity

V_m - normalized transmembrane potential

δ_x – lateral resolution

δ_z – axial resolution

λ_0 – central wavelength

List of Figures

List of Tables

Acknowledgements

I express my sincere thanks to my advisor, Dr. Christine P. Hendon. Throughout my years in the doctoral program, she has guided me with great empathy, insight, and a true investment in my success. I am so thankful for all of the advice, encouragement, and opportunities she has provided me. Most especially, I will always be grateful to her for inspiring in me the courage to reach my goals.

I would also like to thank my lab mates, including Yu Gan, Xinwen Yao, Yuye Ling, Nathan Lin, Rajinder Singh-Moon, Alex Park, Diana Mojahed, James McLean, and Ziyi Huang. It has been a joy to come to an office filled with such amazing people each day. I am thankful for all of the help and guidance they have provided me, as well as the enjoyable day-to-day discussions, jokes, and outings.

I would also like to thank my collaborators. I am so grateful to Dr. Andrew McCulloch, Kevin Vincent, and the other members of the Cardiac Mechanics Research Group at the University of San Diego, for their invaluable help as well as their hospitality during my visits in the summer. I would also like to thank Dr. Vivek Iyer and Dr. Charles C. Marboe for their wonderful guidance on the clinical side of research.

And finally, I would like to thank my family, for all of their love and unconditional support. They have blessed me with limitless encouragement, caring, advice, and comfort. I am so thankful to them for always providing me a welcoming home to return to. There are not enough words to express my gratitude for them as they continue to support me throughout my journey.

This work is dedicated to my family.

Chapter 1 Background and Significance

1.1 Atrial Fibrillation

Atrial fibrillation is the most common major cardiac arrhythmia [1] and a significant cause of morbidity and mortality. During atrial fibrillation, abnormal patterns of electrical activation in the atria cause irregular pumping of the heart, potentially leading to serious complications such as stroke and heart failure. It is estimated to affect about 33.5 individuals world-wide, [2] and the condition is associated with a five-fold increase in the risk of stroke, [3] as well as a 1.5 to 1.9-fold increase in mortality risk. [4] Atrial fibrillation is also associated with substantial healthcare costs, with the net incremental cost per patient per year in the USA estimated to be about $8,705. [5] With the prevalence of atrial fibrillation only expected to increase in future years due to the aging population, [6, 7] atrial fibrillation poses a significant health concern.

Despite years of research, the underlying mechanisms of atrial fibrillation remain poorly understood. Atrial fibrillation is initiated and maintained by a trigger and a vulnerable substrate. [8] However, the specific, driving mechanisms of atrial fibrillation remain under debate. Several hypotheses of the electrophysiological patterns underlying the mechanisms of atrial fibrillation have been proposed over the years, including multiple reentrant wavelets, [9] a single reentrant circuit with fibrillatory conduction, [10] rapidly triggering foci, [11] rotors or spiral waves, [12] and epicardial and endocardial disassociation. [13, 14] The substrate of atrial fibrillation involves both electrophysiological remodeling, such as changes in ion channel function and refractoriness, and structural remodeling, such as fibrosis. [8]

Several different features of atrial tissue have been proposed to contribute to the arrhythmogenic structural substrate of atrial fibrillation. Due to anisotropic electrical conduction along myofiber orientation, regions of complex myofiber orientation or abrupt changes in myofiber direction may promote reentry, [14, 15] and myofiber orientation may become altered over the progression of the disease. [16] Fibrosis may similarly promote the drivers of atrial fibrillation, is associated with atrial fibrillation remodeling, and has gained significant interest as an arrhythmogenic substrate. [14, 17] The accumulation of epicardial adipose tissue has been associated with atrial fibrillation, and adipose infiltrations into the myocardium may disrupt normal electrophysiological conduction. [18] Thus, understanding the tissue structure of the atria is critical to further delineating the mechanisms of atrial fibrillation.

This thesis aims to improve the study of atrial fibrillation through the use of optical coherence tomography imaging to better define the structural substrate underlying the arrhythmia in the left atrium. The 3D substrate underlying atrial fibrillation mechanisms remains to be fully identified, limited by current imaging resolution. To better define current limitations in the imaging of atrial structure, however, it is first helpful to review the current methods used to treat atrial fibrillation. Atrial fibrillation may be treated with antiarrhythmic medicine, electrical cardioversion, or ablation procedures. [19] For this study, much of the focus will be on radiofrequency ablation.

1.2 Radiofrequency Ablation

1.2.1 Overview

Initially demonstrated by Cox et al. [20], radiofrequency ablation has become a standard therapeutic approach for atrial fibrillation. The goal of radiofrequency ablation is to interrupt or isolate areas of abnormal electrical conduction through the creation of non-conducting lesions in the atria. For the time being, ablation efforts typically focus on the left atrium. To access the heart,

a catheter is advanced through the femoral vein of the groin, where it eventually enters the right atrium from the superior vena cava. From the right atrium, the catheter is inserted through the inter-atrial septum through a procedure called transseptal puncture. The navigation of the catheter throughout the ablation procedure is typically guided through echocardiography and fluoroscopy, which are used to track the position of the catheter, identify anatomical features, and assess any complications that may arise. [21-23] Once within the left atrium, the standard approach for the placement of lesions is to encircle the pulmonary veins, called pulmonary vein isolation. This method has become the cornerstone of atrial fibrillation ablation since the discovery that arrhythmogenic, triggering ectopic beats frequently originate within the pulmonary veins. [24] Widely encircling the pulmonary veins with ablation lesions placed within the left atrial antrum, known as wide-area circumferential ablation, has been found to be an effective approach for pulmonary vein isolation. [25] Directly ablating within the pulmonary vein ostia has fallen out of favor since the observation that doing so increases the risk of pulmonary vein stenosis. [26] In addition to fluoroscopy and echocardiography, electroanatomical mapping, first demonstrated by Pappone et al. [27], is also useful for ablation guidance and lesion placement. Electroanatomical mapping combines anatomical information with electrophysiological measurements such as voltage and activation times, and allows tracking of catheter position within the cardiac chamber, typically through magnet-based systems. The anatomy of the cardiac chamber is constructed as a 3D shell and then registered with electrical measurements through sequential, catheter point-by-point mapping or simultaneous multielectrode mapping. Electroanatomical maps can also be used to tag anatomical landmarks and record the location of generated lesions. [28] The anatomical information provided by electroanatomical mapping systems can be improved by integration with computed

tomography (CT) or magnetic resonance imaging (MRI) [29], which are often carried out pre-procedurally to assess the patient's atrial anatomy and pulmonary vein morphology. [30]

1.2.2 Additional Ablation Strategies

Aside from pulmonary vein isolation, adjunctive ablation strategies have been attempted in an effort to improve outcomes. Ablation in patients with persistent or permanent atrial fibrillation often fails to provide a long-term cure, necessitating the search for additional, effective ablation targets. These approaches may be based on alternative anatomical regions of interest, such as the application of linear lesions along the left atrial roof or the mitral isthmus. [31] However, the creation of linear lesions in addition to pulmonary vein isolation has failed to show an improvement in outcomes in clinical trials [32, 33]. Ablation based on electrophysiological patterns have also been investigated, including the ablation of dominant frequency, ablation of complex fractionated electrograms (CFAEs), ablation of non-pulmonary vein foci, ablation of scar or fibrosis, and ablation of rotational activity. Dominant frequency refers to the rate of atrial activation at a particular site, which can be measured through spectral analysis of atrial electrograms. Regions with higher dominant frequency have been theorized to maintain atrial fibrillation and be targets of interest during ablation. [34] CFAEs are typically low-voltage electrograms with highly fractionated potentials or with very short cycle length, and have also been believed to play an integral part in atrial fibrillation mechanisms and act as optimal ablation targets [35]. Both dominant frequency and CFAE ablation, however, have failed to show improvement for persistent atrial fibrillation in clinical trials [33, 36, 37]. Non-pulmonary vein triggers may be identified through the administration of drugs or pacing, and ablation of such sites have shown some success, although more investigation is needed to define the optimal approach for mapping such triggers and the value of the approach on outcomes. [38] Fibrosis, which causes an increased deposition of collagen within

the myocardium, is believed to perpetuate atrial fibrillation by altering conduction velocity and anisotropy, creating blocks, or acting as anchors for reentrant waves. [17, 39] Thus, regions of fibrosis have been proposed as effective ablation targets, and may be localized through the identification of low voltage regions [40] or through MRI [41]. Atrial fibrosis as imaged by delayed-enhancement (DE) MRI was found to be associated with the recurrence of atrial fibrillation after ablation [42], and the DECAAF-2 clinical trial is currently being carried out to determine if the ablation of fibrotic regions in addition to pulmonary vein isolation can improve outcomes in persistent atrial fibrillation patients. Finally, the ablation of rotational activity, also known as focal impulse and rotor modulation (FIRM)-guided ablation, targets cyclic activations, which revolve around a core of approximately zero conduction velocity, as well as spontaneously firing focal sources. Rotors and focal sources can be mapped through the use of basket catheters. [43, 44] Body surface potential mapping approaches to identify rotors have also been developed. [45] The effectiveness of ablation of rotor and focal sources is still under investigation. [38]

1.2.3 Remaining Challenges in Radiofrequency Ablation

The optimal approaches for atrial fibrillation ablation remain to be well established. Currently, variable success after ablation has been reported, and the overall long-term, single-procedure success rate has been estimated to be about 50%. The overall long-term, multiple-procedure success rate has been estimated to be about 80%. [46] However, for patients with persistent atrial fibrillation, it has been observed that about 50% still experience arrhythmia reoccurrence after their final procedure. [47] Therefore, much work remains in improving the efficacy of ablation therapy for atrial fibrillation, especially for more advanced forms. Because tissue structure plays an integral part on electrophysiological patterns and the progression of disease, improving the understanding of atrial structure has been of interest for improving the

understanding of atrial fibrillation mechanisms. Further advances in imaging guidance are also needed to improve the identification of substrates of interest during ablation. For instance, CFAEs may arise from different sources, only some of which may be arrhythmogenic, but may be linked to underlying fibrosis. [48, 49] Low voltage areas recorded by electrocardiac electrodes may indicate fibrosis or may simply be an effect of thick endocardium. [50] For this reason, there has been significant efforts in improving the imaging of the atrium, particularly in detecting myofiber orientation and fibrosis. The tissue structure extracted from these images may also be incorporated into realistic, image-based models to further probe the effect of tissue structure on electrophysiological mechanisms.

1.3 Cardiac Imaging and Modeling

1.3.1 Atria Imaging and Electrophysiological Models

Several different imaging and modeling approaches have been applied in research to better delineate the structure of the left atrium and its effect on the mechanisms of atrial fibrillation. Due to its thin-walled structure, details of human left atrial tissue, and in particular myofiber orientation, is difficult to image with commonly used imaging modalities such as MRI, CT, and echocardiography. With respect to realistic tissue structure, early image-based models included only anatomical information of the left atrium, derived from an atlas such as the Visible Human Project [51, 52]. Alternatively, serial sectioning of atrial tissue and high-resolution imaging of each slice using a digital camera has been used to quantify fiber orientation. This method has been carried out in sheep atria, with the resulting structural information incorporated into electrophysiological models to investigate the effect of fiber orientation on electrical propagation [53]. Left atrial models used for electrophysiological simulation and incorporating image-based anatomy from MRI or CT have also been developed, but with fiber orientation derived from literature registered to the models

6

[54-57]. More recently, transmural imaging of myofiber orientation over whole human atria has been demonstrated using diffusion-tensor MRI [58]. Contrast-enhancement MRI [59] and micro-CT [60] have also been utilized to image myofiber orientation in human and canine atria, respectively, with the data incorporated into image-based models for electrophysiological simulation.

In addition to myofiber orientation, other tissue features of interest include fibrosis, adipose tissue, ablation lesions, and myocardial sleeves of the pulmonary veins. In the past few years, fibrosis has gained a significant amount of interest as a substrate of atrial fibrillation, and imaging of fibrotic regions within atrial fibrillation patients have been carried out using delayed-enhancement MRI, [41] as mentioned previously, and late-gadolinium enhanced (LGE) MRI [54]. Using LGE MRI, patient-specific atrial anatomy and fibrosis distributions have been acquired from atrial fibrillation patients and incorporated into models which may be useful for pre-ablation planning of ablation targets based on the distribution of fibrosis [61]. Additionally, fibrosis as identified from contrast-enhancement MRI has been incorporated into electrophysiological models to study the effect of fibrosis on electrical conduction [59]. Increased adipose tissue has also been found to be correlated to atrial fibrillation [18], although the majority of the focus has been on epicardial adipose tissue, which can be imaged using MRI [62] or CT [63]. Recently, however, MRI imaging of fat and fatty fibrosis within the myocardium of human atrial tissue has been demonstrated [64]. Fat within the interatrial septum has also been associated with atrial fibrillation, and has been imaged using MRI [65]. Imaging of ablation lesions has been demonstrated using MRI, which may be useful for evaluating the permanence of lesions and predicting atrial fibrillation reoccurrence post-ablation [66, 67]. Finally, the myocardial sleeves of the pulmonary veins play a

critical role in the triggering of atrial fibrillation, and imaging of the thickness of pulmonary vein layers have been carried out using intravascular ultrasound [68, 69].

1.3.2 Optical Mapping

It is useful to correlate structural characteristics to experimental electrophysiological measurements. In particular, optical mapping is a popular method with which to track the propagation of electrical propagation in cardiac tissue through the use of voltage-sensitive fluorescent dyes. Correlation of optical mapping measurements to imaged tissue features such as fiber orientation and fibrosis have enabled some insights on the impact of these features on arrhythmia mechanisms. Optical mapping measurements have also been used to inform electrophysiological model parameters or validate simulated results [15, 59]. However, because the optical mapping signal, captured only from the fluorescence that exits the tissue's surface, integrates fluorescence that originates from multiple depths, optical mapping signals may have altered morphology when compared to electrophysiological signals. Examples of this includes dual-humped optical action potential morphology due to activation from multiple layers [70] or changes in the optical action potential upstroke based on sub-surface electrical wave propagation direction [71]. Therefore, to enable better interpretation of optical mapping measurements, models that simulate the synthesis of the optical mapping signal have been developed. Image-based models of ventricular tissue have been created and used to simulate optical mapping [72-76].

1.3.3 Remaining Challenges in Left Atrial Imaging and Modeling

Several challenges remain in the detailed imaging of the human left atrium, particularly in terms of imaging resolution. The average thickness of the human left atrial wall is 3 mm, with a range from 1.5 mm to 6.5 mm. [77] Recent studies have observed differences in electrical activation patterns between the endocardial and epicardial atrial wall, sparking interest in the

electrical propagation that may occur transmurally over the depth of the atrial wall. [14, 78] The left atrial wall is composed of complex layers of myofibers that may be oriented at nearly orthogonal directions at different depths or have abrupt changes in orientation. [58, 79] Fibrosis can have different types of distributions throughout the wall, being interstitial, patchy, or diffuse. While it is has been observed that fibrosis provides an arrhythmogenic substrate, the relative effect of the specific 3D distribution of fibrosis throughout the depth of the wall remains to be determined. [50] Due to the thinness of the left atrium, current cardiac imaging modalities remain limited in their ability to resolve finer features across the heart wall, including myofiber orientation over depth in thin regions, specific distributions of fibrosis, and smaller fatty infiltrations. In light of these challenges, optical coherence tomography (OCT) may be a useful adjunctive imaging modality that can offer valuable information where other imaging modalities face difficulties. OCT has micrometer resolution, is non-destructive, and can be incorporated into imaging catheters for *in vivo* imaging. Therefore, OCT may be highly applicable for providing imaging guidance for ablation, enabling better understanding of the left atrial substrate, and informing realistic electrophysiological models.

1.4 Optical Coherence Tomography

Since its origins in the early 1990s [80], optical coherence tomography (OCT) has become a well-established imaging modality for biomedical and clinical applications. Based on low coherence interferometry, OCT images the depth profile of a tissue sample by measuring the interference between light backscattered from the sample and light reflected from a reference mirror. OCT can non-destructively image the three-dimensional microstructure of biological tissues with an imaging resolution ranging from 1 to 15 µm, penetration depths of 2 to 3 mm [81], and video rate imaging speeds [82]. OCT can also provide functional data, such as the

9

measurement of birefringence, a useful indicator of tissue organization, using polarization sensitive (PS) OCT [83]. OCT has been applied to ophthalmology [84], intravascular imaging [85], dermatology [86], gynecology [87], and other clinical and research fields.

1.4.1 Time Domain Optical Coherence Tomography

The basic mechanism of OCT is based on the Michelson interferometer. The first type of OCT system developed was Time Domain (TD) OCT, and a simplified schematic of a TD-OCT setup is provided in Figure 1.1. Light from a broadband, low coherence light source is directed towards a beam splitter, which directs light towards the sample arm containing the sample to be imaged and the reference arm containing a mirror. Light incident upon the sample is backscattered due to discrete reflecting particles within the sample as well as changes in refractive index. Light from both arms are reflected back towards the beam splitter, where the beams recombine and are then collected by the detector. For TD-OCT, the detector is a single-channel photoreceiver.
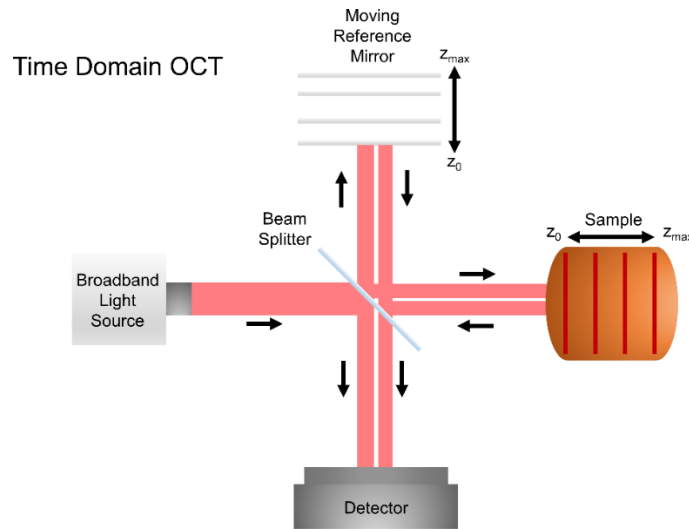
Figure 1.1. Time domain OCT system schematic. In this example, the depth of the sample ranges from z_0 to z_{max}. The reference mirror is axially scanned over an equivalent distance to capture the reflectivity profile of the tissue sample.

The interference pattern of light from the reference and sample arms can only be resolved when the optical path length difference between the two beams, determined by the position of the mirror and the depth in the tissue from which the light was backscattered, is less than the coherence length of the light source. For a given position of the reference mirror, an interference fringe burst is generated corresponding to a localized depth within the tissue. For a fixed x-y position on the sample, the reference mirror can be translated with a piezoelectric stage to generate an interferogram containing a fringe burst pattern corresponding to the interference from multiple depths. This interference burst pattern can then be demodulated to generate an intensity depth profile of the sample, called an A-scan. This procedure is represented in Figure 1.2, which shows the detected interferogram and corresponding A-line, post-demodulation, corresponding to four discrete reflectors equally spaced throughout the depth of an imaged sample.
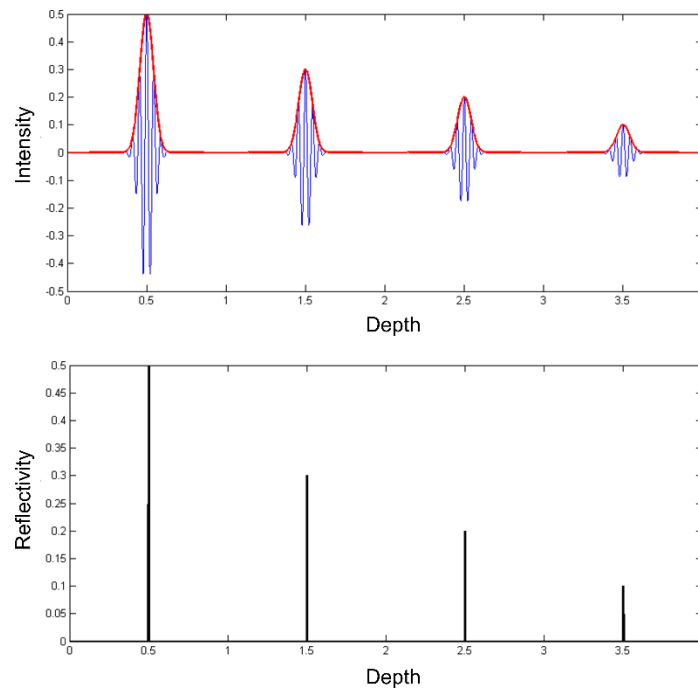
Figure 1.2. Simple OCT interferogram (blue) and A-line after demodulation (red). The corresponding, true reflectivity of the sample over depth is given below.

Galvo mirrors are used to scan the beam over the sample in lateral dimensions. The acquisition of multiple A-lines can be composed into a two-dimensional image, called B-scans. Scanning in both x and y lateral dimensions enables the generation of three-dimensional image volumes, as shown in Figure 1.3.
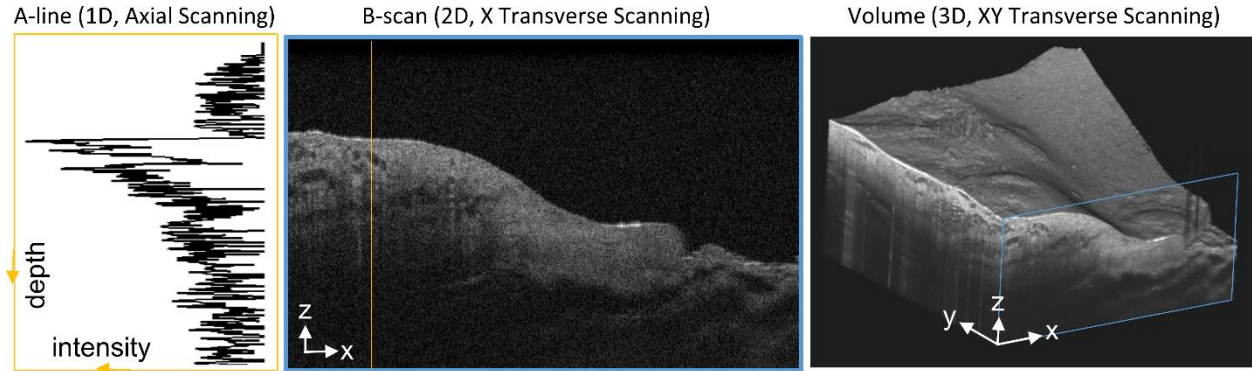
Figure 1.3. Examples of acquired OCT data. The orange line corresponds to A-line location within the B-scan, while the blue box corresponds to the B-scan location within the 3D image volume.

1.4.2 Fourier Domain Optical Coherence Tomography

Developed after the creation of TD-OCT, Fourier Domain (FD) OCT captures the interference pattern in the spectral domain instead of the time domain. FD-OCT has been demonstrated theoretically and experimentally to have superior sensitivity than TD-OCT, enabling higher speed imaging applications [88-90]. FD-OCT is divided into two sub-categories: spectral domain (SD) OCT, in which a spectrometer and array detector are used for detection, and swept-source (SS) OCT, or optical frequency domain imaging (OFDI), in which a wavelength-swept light source is used for illumination and a single or small number of photoreceivers detect the interference signal over time. Basic schematics of a SD-OCT and SS-OCT setup are provided in Figure 1.4.
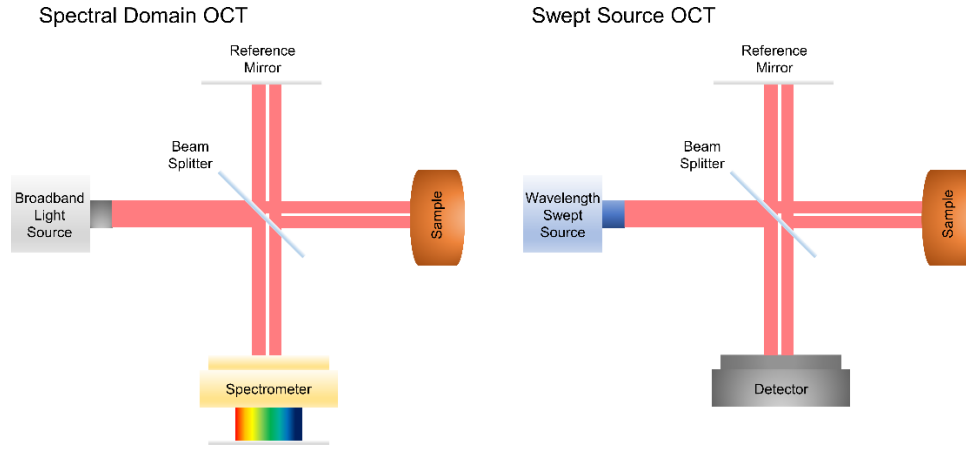
Figure 1.4 Spectral domain and swept-source OCT system schematics.

In FD-OCT, the reference arm remains stationary and is fixed at a distance equivalent to the approximate location of the sample. The full depth profile of the tissue sample at a given x-y location is encoded within the detected interferogram, which is collected in the spectral domain. The spectral interferogram collected by the detector must be pre-processed and inverse Fourier transformed to obtain the intensity depth profile of the sample. The basic signal processing steps for this procedure are as follows. First, the DC component of the spectral interferogram must be removed, which occurs primarily due to the reference mirror. The DC component can be removed by detecting a signal with only the reference mirror, and no sample present in the sample arm, and using the resulting signal as a template for the DC component and subtracting it from subsequently detected signals. Second, the spectrum must be converted from wavelength domain to wavenumber domain. Finally, the spectral interferogram must be Fourier transformed to construct the A-line.

1.4.3 Optical Coherence Tomography Parameters

The axial resolution of both TD- and FD-OCT systems, δz, is governed by the light source's central wavelength λ_0 and full-width at half-maximum (FWHM) bandwidth $\Delta\lambda$.

13

Equivalently, the axial resolution is proportional to the coherence length of the light source, which is the FWHM of its coherence function. Assuming a Gaussian spectrum, the equation for axial resolution is given by:

$$\delta z = \frac{2\ln(2)}{\pi} \frac{\lambda_0^2}{\Delta\lambda} \tag{1.1}$$

The lateral resolution of an OCT system, δx, is defined as the FWHM of the point spread function of the sample arm beam at the focal plane. It is determined by the central wavelength of the light source, λ_0, and the numerical aperture, NA, of the objective lens.

$$\delta x = 0.37 \frac{\lambda_0}{NA} \tag{1.2}$$

The axial field of view, FOV_{axial}, or depth of focus of an OCT system is defined as the FWHM of the confocal axial response function, which is dependent on the center wavelength of the light source, λ_0, and the numerical aperture, NA, of the objective lens.

$$FOV_{axial} = \frac{0.565\lambda_0}{\sin^2\left(\frac{\sin^{-1}(NA)}{2}\right)} \tag{1.3}$$

Lateral resolution and axial field of view are inversely proportional, and there is a tradeoff between the two parameters in OCT system design. The lateral field of view, $FOV_{lateral}$ of an OCT system is dependent on its individual lateral scanning mechanism. However, assuming the scanning mechanism has a maximum scan angle of θ_{max} through the input aperture of the

objective lens and that the objective lens has a focal length, f, the $FOV_{lateral}$ can be given by the following. [91]

$$FOV_{lateral} = 2f\theta_{max} \qquad\qquad (1.4)$$

1.5 Cardiac Applications of Optical Coherence Tomography

Due to its high resolution, fast imaging speeds and non-destructive imaging capabilities, the use of OCT to image cardiac microstructure has increased over the past two decades. Currently, the primary applications have been the imaging of heart tissue structure in small animal models, especially the imaging of myofiber organization, and the monitoring of radiofrequency ablation lesion formation using OCT-integrated catheter designs. The imaging of cardiac tissue structure in large animal models, and in particular, OCT imaging of the human heart, has also been of recent interest.

1.5.1 OCT Imaging of Cardiac Structure in Animal Models

OCT has been used to image myofiber orientation, small animal heart morphology, and the organization of the cardiac conduction system. OCT imaging and extraction of myofiber orientation has been demonstrated using both intensity-based [92-98] and polarization sensitive methods [83, 99-103] in both small and large animal hearts. In some cases, optical clearing [94, 96] or serial sectioning [97] have been employed to improve imaging depth. Myofiber disorganization and variability identified through OCT have been correlated to regions of infarction and cardiomyopathy in mouse or rat ventricles [83, 102, 103]. Through the use of stitching algorithms to combine multiple OCT image volumes encompassing the whole heart, morphological parameters such as heart size, wall thickness, and mass have also been measured

for diseased and normal small animal hearts [102, 104]. Structural features of the cardiac conduction system, including the Purkinje network [105], the atrioventricular node [93, 106, 107], and sinoatrial node [107] have been investigated using OCT in the rabbit and canine heart. OCT measurements of myofiber orientation in the sinoatrial node, atrioventricular node, and right ventricular free wall have been correlated to fluorescent measurements of electrical conduction, enabling better understanding of the influence of myofiber orientation on cardiac function [93, 106, 107]. Biomechanical characterization of cardiac tissue has also been carried out using shear wave imaging OCT [108].

1.5.2 OCT Imaging for Radiofrequency Ablation Guidance

With its high imaging speed and resolution, OCT has been proposed as a real-time imaging guidance tool for ablation procedures for atrial fibrillation. OCT-integrated catheters have been developed [109-112] and imaging of myocardial features have been demonstrated *in vivo* in swine hearts [113, 114]. OCT is able to identify tissue contact between the probe and the cardiac wall [110, 113, 114], as myocardial features become more apparent with the displacement of blood that occurs at probe contact. The location and development of ablation lesions can be tracked with OCT by the appearance of the birefringence artifact band, which is a dark band in the myocardium that disappears within regions of ablation lesions [109, 110, 115]. However, because the birefringent artifact may fluctuate in an *in vivo* setting [114], PS-OCT approaches to identifying the ablation lesion have been proposed as a more sensitive indicator [111, 112, 116]. OCT imaging during ablation may also be able to provide information of tissue structural changes indicative of complications occurring during energy delivery, such as the formation of tears within the ablated region [113, 115]. Tissue features such as fat and vessels may also be identified during epicardial ablation [109].

1.5.3 OCT Imaging of the Human Heart

There have been a few studies of OCT imaging in the human heart. In 2009, general features such as myofiber organization from small regions from the human right atrium, left and right ventricles, atrioventricular node, and sinoatrial node were presented. [117] In 2016, different tissue types within human left atrial tissue, including dense collagen, loose collagen, fibrotic myocardium, adipose tissue, and normal myocardium, were imaged and analyzed using an automatic classification scheme. [118] An ultra-high resolution OCT system has been developed and shown to image detailed tissue features such elastic fibers, collagen fiber bundles, adipose tissue, myofibers, and chordae tendineae in the human ventricular septum. [119] A high resolution cross-polarization OCT system also showed distinguishing features between endocardial scar, thickened endocardium, fibrosis, and ablation lesions in the right ventricular septum. [116]

These imaging studies focused on small regions of the human heart chambers, without providing a comprehensive study of the distribution of different tissue types throughout the chamber or analyzing the tissue features identified with OCT in relation to cardiac anatomy. Because the dynamics of atrial fibrillation are closely tied to atrial anatomy and spatial distribution of structural features, it is necessary to identify tissue features in the context of the whole atrial anatomy. More comprehensive imaging is necessary to determine the full utility of OCT in improving our understanding of the structural substrate of atrial fibrillation. Additionally, the use of OCT to inform structurally realistic cardiac models for simulating electrophysiological dynamics has not yet been explored despite the high-resolution structural information OCT can offer.

1.6 Objectives

There exists a need to better define the structural substrate of atrial fibrillation, including depth-resolved information on myofiber orientation, fibrosis, and adipose tissue. OCT imaging can provide valuable, high-resolution information on tissue microstructure, and advances have already been made in applying OCT to cardiac imaging and atrial fibrillation ablation guidance. However, comprehensive imaging of the human atria with OCT and the integration of OCT imaging data in electrophysiological modeling, like those that exist for MRI and CT, remain to be established. This information could provide further guidance on the application of OCT to the treatment of atrial fibrillation. Therefore, the objectives of this study are as follows: (1) to comprehensively image the human left atrium with OCT, providing a detailed overview of the tissue and image features that can be expected in OCT imaging of the human left atrium, and provide these features within the context of the whole left atrial anatomy, and (2) to develop a modeling workflow to integrate OCT imaging data of atrial tissue into tissue-specific, cardiac models for electrophysiological and optical mapping simulation. The thesis is organized as follows. Chapter 2 provides an overview of the OCT image features of the human left atrium and pulmonary veins and the distribution of imaged tissue features throughout the chamber. The OCT imaging data of the human left atrium will also be discussed in the context of a whole human heart OCT imaging atlas. Chapter 3 describes the modeling workflow for integrating structural features extracted from OCT into models for electrophysiological and optical mapping simulation. Chapter 4 provides several applications of the modeling workflow to OCT-derived models of cardiac tissue incorporating myofiber orientation, ablation lesions, and different tissue types. Chapter 5 will summarize the thesis and describe future aims.

Chapter 2 Comprehensive Characterization of the Human Left Atrium with Optical Coherence Tomography

2.1 Introduction

Detailed imaging of tissue structure in the human left atrium is a growing area of research for improving the understanding and treatment of atrial fibrillation. With the acknowledgement that complex interactions with tissue microstructure across the atrial wall may maintain arrhythmia mechanisms [14, 78, 120], there have been significant efforts in improving the resolution of imaging in the human atria as described previously in Chapter 1.3. Through these imaging studies, as well as from information gathered from histological studies, a general understanding of left atrial features potentially contributing to atrial fibrillation mechanisms has been developed, with particular attention paid to the influence of myofiber orientation and fibrosis. An overview of tissue features of interest and their relevance as potential structural substrates of atrial fibrillation is briefly provided below to establish the current body of knowledge before exploring OCT imaging of the human left atrium.

2.1.1 Myofiber Orientation in the Left Atrium

Myofiber orientation in the human left atrium has been described as being composed of one to three layers, [79] with the myofiber layers blending into one another or, in contrast, angled nearly orthogonally to one another with abrupt changes in orientation over depth. [121] Myofiber orientation within the left atrium has been noted to be heterogeneous, with dispersion of transmural fiber orientation varying over different regions of the left atrium. The inferior and anterior sides of the left atrium and areas near the pulmonary veins were reported to typically have higher

transmural dispersion, while the lateral wall below the left pulmonary veins had lower dispersion. [58] Additionally, several studies have commented that a generalized pattern of myofiber orientation can be observed across the left atria of different hearts, but local variations and exceptions to typical patterns were frequently noted. [58, 121, 122] Regions of complex myofiber orientation and abrupt changes in fiber angle have been associated with arrhythmia dynamics, such as anchoring of high-frequency drivers [15] and activation time dispersion. [53] Remodeling of transmural fiber orientation associated with atrial fibrillation, as observed in goat atria, has been proposed to contribute to dissociation of endocardial and epicardial electrical activity. [16] On the contrary, differences in left atrial myofiber orientation of atrial fibrillation patients compared to healthy patients were not found in a small sample size of human left atria as imaged by DT-MRI. [58] Remaining questions on the influence of myofiber orientation on atrial fibrillation, especially as part of a transmural three-dimensional substrate, and the variability and potential remodeling among different individuals suggests a need for high-resolution, personalized imaging to further probe the effect of myofiber organization on arrhythmia.

2.1.2 Fibrosis in the Left Atrium

The extent of fibrosis in the atria, as imaged with DE-MRI, has been shown to be a significant indicator of ablation outcomes. [42] However, further research is needed to define the specific relationship between fibrosis and atrial fibrillation, and particularly the influence of different densities of fibrosis on arrhythmia dynamics. Fibrosis can exist in categories based on their distribution, such as interstitial, diffuse, compact, and patchy fibrosis, as shown in Figure 2.1, although the distinction between categories is a blurry one.
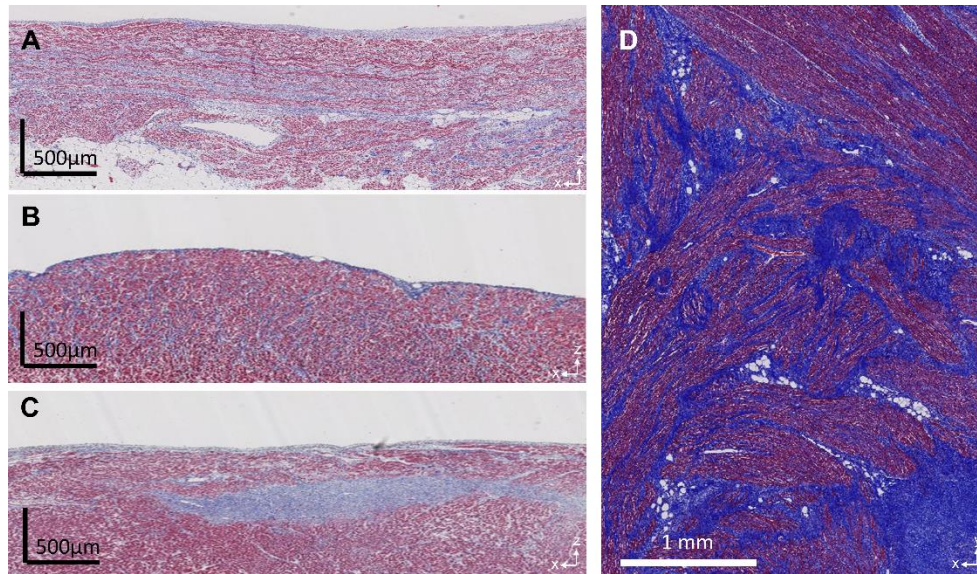
Figure 2.1. Trichrome histology slides of different distributions of fibrosis. Collagen is indicated by blue, and myocardium is indicated by red. A, Interstitial fibrosis. B, Diffuse fibrosis. C, Compact fibrosis. D, Patchy fibrosis.

Currently, the influence of compact and diffuse fibrosis has not been demonstrated to significantly contribute to atrial fibrillation dynamics. However, several histological studies have identified the influence of patchy and interstitial fibrosis on atrial fibrillation propagation. Patchy fibrosis has been reported through optical mapping experiments and computer simulation to be involved in arrhythmogenic behavior by anchoring reentrant waves and causing conduction delays and fractionation. [123] Interstitial fibrosis has been reported to be more abundant in goat models of long term or chronic atrial fibrillation, and have been proposed to support dissociation between epicardial and endocardial electrical patterns and cause anisotropic slowing of conduction. [124, 125] Gadolinium-enhanced (GE) MRI has imaged interstitial fibrosis in the human right atria, which were determined to cause transmural activation delays and anchor reentrant drivers, [14] while correlation of LGE-MRI imaging to optical mapping experiments and simulations has shown that atrial fibrillation drivers clustered around the borders of fibrotic atrial regions. [17] These studies support that patient-specific and three dimensional distributions of fibrosis have a

21

significant influence on arrhythmia dynamics. However, detailed imaging of fibrosis distributions across the left atrial wall has not yet been demonstrated.

2.1.3 Other Structural Substrates of Atrial Fibrillation

Other features of interest relevant to atrial fibrillation include adipose tissue, as well as anatomical structures such as the pulmonary veins and the atrial septum. Increased epicardial adipose as well as interatrial fat have been associated with atrial fibrillation, [65] and increased epicardial adipose tissue has been found to be a predictor of radiofrequency ablation recurrence. [126] Epicardial fat may infiltrate into the myocardium and has been theorized to influence conduction, [18] but the effect of intra-myocardial adipose deposits within the human atria on electrophysiological patterns have not yet been well-studied.

The pulmonary veins have become highly relevant to atrial fibrillation after the discovery that ectopic beats originating from the myocardial sleeves of the pulmonary veins are often the initial triggers for atrial fibrillation, particularly for paroxysmal atrial fibrillation. [24] As identified from histology, the pulmonary veins are internally composed of venous media and an external fibro-fatty adventitia. The transition from left atrial tissues to the pulmonary veins is a gradual one, and myocardial extensions from the left atrium into the pulmonary veins can extend as far as 25 mm into the vein. [127, 128] A thin fibrofatty or loosely fibrous layer has been observed between the venous media and the myocardial sleeves. [129, 130] A representative histology slide showing the pulmonary vein structure is given in Figure 2.2.
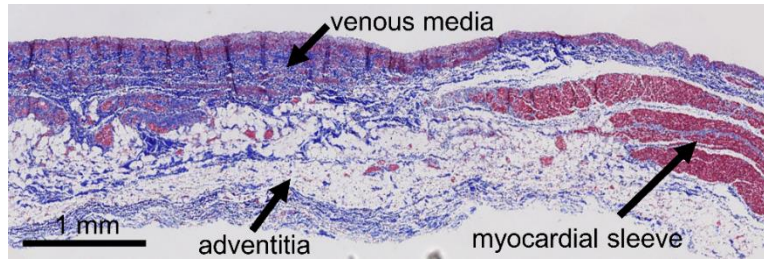
Figure 2.2. Pulmonary vein structure.

Reentry is often cited to anchor around the pulmonary veins, [131] and from a structural viewpoint, may be influenced by the heterogeneous myofiber orientation and fibrosis that can be commonly found around and inside the pulmonary veins. Histological studies have shown that the myocardial sleeves can have complex myofiber arrangement with crossing and mesh-like patterns [127, 130]. Studies in canines have shown regions of myofiber complexity correlated to electrical conduction disturbances, [132, 133] while arrhythmogenic high-frequency potentials have been associated with thickened PV walls [69]. AF patients have also been reported to have higher degrees of discontinuity, hypertrophy, and fibrosis within their PV myocardial sleeves [128].

The interatrial septum in normal developed hearts contains the remnants of the valve of the foramen ovale, which was originally an open channel in which blood could flow in the developing heart. During radiofrequency ablation, the left atrium is accessed by puncturing the thinnest part of the septum, the fossa ovalis, which is typically composed of endocardium on both sides with myocardium in between. [134] From the left atrial side, the septum is difficult to identify from the other walls of the left atrium other than by the appearance of a small crescent wedge or through transillumination to identify the thin region of the fossa ovalis. [121] The interatrial septum has been noted as one of the most common locations where non-pulmonary vein triggers of atrial fibrillation can be found. [38]

2.1.4 OCT Imaging of the Human Left Atrium and Objective

OCT imaging guidance for radiofrequency ablation of atrial fibrillation has been under investigation over the past few years, with OCT-integrated catheters for lesion monitoring having been developed and tested *in vivo* in swine hears. [112-114] However, while there have been a few studies focused on imaging specific features within human hearts, such as different tissue types, [118] lesions, [112] and features of the conduction system, [117] there is a lack of comprehensive OCT imaging data covering the whole human left atrium. Understanding the spatial distribution of tissue features as imaged by OCT in the context of the whole left atrial anatomy can provide a better understanding of the applicability of OCT to mapping the structural substrate of atrial fibrillation. Furthermore, OCT imaging of the human left atrium contributes to a whole human heart OCT imaging atlas, such as those that currently exist for intravascular OCT [135] and retinal OCT imaging [136]. Such an atlas, more generally speaking, can guide future cardiac applications of OCT. Therefore, the objective of this chapter is to provide a detailed overview of OCT imaging features in the human left atrium, assessing the capability of OCT to image important structural features, as well as provide insight on an overall cardiac OCT imaging atlas.

2.2 Methods

2.2.1 Tissue Acquisition

Diseased human hearts (n=21) were acquired under an approved protocol from the National Disease Research Interchange (NDRI). The inclusion criteria for the protocol was based on the following diagnoses: end stage heart failure, cardiomyopathy, coronary heart disease, amyloid, atrial fibrillation, and myocardial infarction. NDRI received consent for all donors. All specimens were de-identified and considered not human subjects research, according to the Columbia University Institutional Review Board Under 45 CFR 46. Donor characteristics are provided in

Table 2.1. The average age was 60 years, with a range of 43 to 77 years. There were 12 female and 9 male donors. Two donors had a history of atrial fibrillation, 7 had congestive heart failure, 3 had myocardial infarction, and 3 had valvular heart disease. Recovery of hearts was completed within 24 hours after death, and the hearts were delivered to the lab while submerged in an ice-cold phosphate-buffered saline bath. From the 21 hearts, 11 left superior pulmonary veins, 9 right superior pulmonary veins, 11 left inferior pulmonary veins, and 8 right inferior pulmonary veins were imaged. Nine pulmonary veins were imaged with surrounding ablation lesions, created using the commercial RFA system, Stockert 70 (Biosense Webster, Diamond Bar, CA), to evaluate OCT imaging of lesions within human atrial tissue.

Table 2.1 Heart donor characteristics.

Heart #	Age	Sex	Cardiovascular Disease History
1	54	M	HTN
2	43	M	HTN, HLD, CHF
3	58	F	HTN
4	67	F	HTN, HLD
5	52	M	MI
6	62	M	HTN, HLD, CAD
7	62	M	CHF, VHD, AF, VT, PVD
8	54	F	PVD
9	77	F	CAD, HTN, CHF, AF, PVD
10	70	F	CHF, HTN
11	46	F	HTN, CAD, MI
12	67	M	MI, HTN, HLD
13	59	F	HTN
14	67	M	CHF, VHD, HLD
15	58	M	CAD, CHF, HTN, HLD
16	68	M	HTN, CAD, HLD
17	62	F	HLD, CAD
18	56	M	VHD, HCM, HTN
19	55	M	CHF
20	58	F	VHD
21	69	M	HTN, CAD, HLD

2.2.2 Dissection Protocol

Upon arrival to the lab, the left atrium and pulmonary veins were isolated from the rest of the heart. Afterwards, the left atrium and pulmonary veins were dissected to flatten the tissues for imaging with OCT. Excluding the initial 6 hearts, which were used for establishing the optimal dissection procedure or for imaging smaller regions of interest, the left atria were dissected with the following procedure to enable flattening of the tissues with the least amount of cuts and to facilitate easy identification of anatomical features after dissection. An example of the dissection procedure is depicted in Fig 2.3. The left atrium was halved, separating the left pulmonary veins from the right pulmonary veins as shown by the dotted black line in the left-most panel of Fig 2.3. Afterwards a longitudinal cut was made along the side of each vein and into the left atrium, as represented by the dotted red line in Fig 2.3. This dissection opened up the vein while keeping the venoatrial junction intact. The flattened tissues were pinned to a corkboard for imaging. The tissues were submerged in a 10:1 phosphate buffered saline solution to prevent the tissue from drying when imaging over larger regions. Due to the left atrial appendage's highly trabeculated surface and the limitations of OCT's imaging depth, the left atrial appendage was not imaged. Three hearts followed a modified dissection procedure as the left atrial tissues were torn upon arrival to the lab.
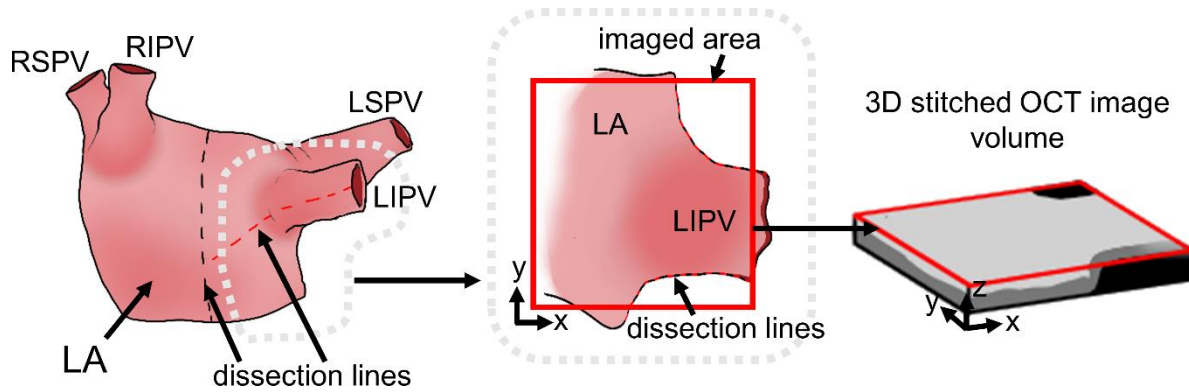
Fig 2.3 Diagram of the dissection procedure and orientation of OCT image volume relative to the tissue. A representative example of the LIPV flattened for imaging is shown. RSPV = right superior pulmonary vein, RIPV = right inferior pulmonary vein, LSPV = left superior pulmonary vein, LIPV = left inferior pulmonary vein.

2.2.3 Imaging Protocol

All tissues were imaged fresh with no prior fixation to evaluate the applicability of imaged tissue features to *in vivo* imaging. The tissues were imaged with the TELESTO I (Thorlabs GmbH, Dachau, Germany) spectral-domain OCT system, which has an axial resolution of 6.5 μm, lateral resolution of 15 μm, and imaging depth of 2.51 mm in air. The system uses a matched pair broadband superluminescent diode light source, with a center wavelength of 1325 nm and a bandwidth of over 150 nm. It uses a linear InGaAs array-based spectrometer. Its maximum axial line rate is 91 kHz, and imaging was carried out at 28 kHz. The OCT-IMM3 immersion-style sample z-Spacer (Thorlabs GmbH, Dachau, Germany) was used to image the tissues while submerged in a phosphate buffered saline solution, as shown in Figure 2.4. Overlapping, 3D image volumes were obtained to cover large regions of tissue. The image volumes were captured with pixel sizes ranging from 5.0 to 6.3 μm in the lateral dimension and 4.9 μm in the axial dimension, in air. Sizes of the image volumes ranged from 3.0 to 5.0 mm in the lateral dimension and 2.51 mm in the axial dimension in air.

27
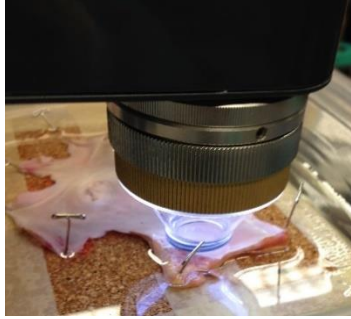
Figure 2.4. OCT imaging of human left atrial tissue with the OCT-IMM3 immersion-style sample z-Spacer.

2.2.4 Histology

After imaging, the tissues of the imaged areas were cut into blocks and placed in 10% formalin for at least 24 hours fixation before being transferred to 20% ethanol. The blocks had maximum x-y dimensions of 40 mm by 30 mm, and 5 μm thick levels were obtained from each block with a maximum of 3 mm between each level. The levels were obtained in the same orientation as the OCT B-scans, except for select regions where levels in the *en face* view were also obtained to enable comparisons of fiber orientation between OCT and histology. The tissues were stained with Masson's Trichrome, and a Leica SCN400 (Leica Microsystems, Wetzlar, Germany) slide scanner with x40 magnification was used to digitize the histology slides. Afterwards, different tissue types were identified from the slides by a cardiovascular pathologist blinded to the OCT images. Histology slides were matched to OCT images acquired from the same location that the histology block had been excised from. Locations of the histology blocks and OCT volumes were determined based on camera images taken during the cutting of the histology blocks and white light images acquired by the TELESTO I system that depicted the field of view within each OCT volume.

2.2.5 Image Processing

2.2.5.1 Image Stitching

Overlapping image volumes were registered and stitched into composite image volumes to better visualize the tissue features. First, the image volumes were manually registered in the *en face* plane (x and y-dimensions) based on matching tissue surface features in the white light images and known lateral translations between each volume during imaging. Custom MATLAB software was used to manually align overlapping white light images and determine the lateral offsets between each consecutive, overlapping pair of image volumes.

The tissue surfaces also need to be aligned in the axial dimension. If the tissues were imaged without the z-Spacer, the tissue surfaces were manually aligned from a sampling of overlapping B-scans from the image volumes to be stitched. If the tissues were imaged with the z-Spacer, however, the contact glass of the z-Spacer deformed the tissue surface, making alignment of the tissue surfaces difficult. Therefore, to ensure the tissue surfaces were axially aligned in stitched image volumes where the z-Spacer was used, the tissue surfaces of each volume were flattened to a uniform depth by surface detection and subsequent shifting of the image pixels. Surface detection was carried out on individual B-scans in all image volumes. First, the B-scan was median filtered with a 3 x 3 kernel to smooth speckle noise. Afterwards, the filtered B-scan was thresholded to separate the image background from the tissue regions. The threshold was empirically determined from a subset of B-scans, and the same threshold was applied to all image volumes. The tissue surface and the contact glass from the z-Spacer are both highly reflective, leading the contact glass of the z-Spacer to be segmented along with the tissue region and interfering with surface detection. Because the contact glass can be seen as a thin, primarily horizontal straight line within the B-scan, the z-Spacer contact glass signal was removed from the

thresholded image by morphological opening using a 15 x 1 rectangular structuring element. With the contact glass signal removed, the tissue surface remains in the segmented image. Therefore, the pixel location of the maximum intensity in each column was taken as the axial position of the tissue surface. The detected tissue surface was smoothed by a 1D median filter with a kernel size of 25. After the location of the tissue surface in a B-scan was determined, the pixels of each column were shifted up the number of pixels necessary to place the tissue surface at a uniform depth throughout the image.

After the lateral offsets between consecutive, overlapping pairs of image volumes were determined and the tissue surfaces of all image volumes were aligned, the image volumes could be stitched together to form the composite image volume. The placement of each image volume in the stitched domain was determined by solving a linear system of equations formed from the known lateral offsets. The coordinates of the origin for an image volume i can be denoted as (x_i, y_i, z_i). The offsets in the x, y, and z dimensions between the origins of consecutive, overlapping image volumes i and i+1 can be denoted as $Dx_{i(i+1)}$, $Dy_{i(i+1)}$, and $Dz_{i(i+1)}$ respectively. Given n individual image volumes and selecting a minimum x_i, y_i, and z_i, $3(n-1)$ unknowns needed to be determined to identify each volume's location in the stitched domain. A set of $3(n-1)$ equations of the forms $x_i - x_{i+1} = Dx_{i(i+1)}$, $y_i - y_{i+1} = Dy_{i(i+1)}$, and $z_i - z_{i+1} = Dz_{i(i+1)}$ could be created from the known lateral offsets, and the system of equations was solved in matrix form. Once the location of each image volume in the stitched domain was determined, stitching was carried out using multiband blending methods as have been described in prior work [137] to smooth the transitions between image volumes. Gain compensation was applied as necessary to some stitched volumes based on image quality. For larger stitched volumes, the stitched image volumes were downsampled by three to decrease computational burden and improve ease of visualization. For

visualization, a uniform contrast adjustment was applied over the entirety of each B-scan or *en face* image until the image features were clear. Representive resulting stitched image volumes are provided in Figure 2.5.
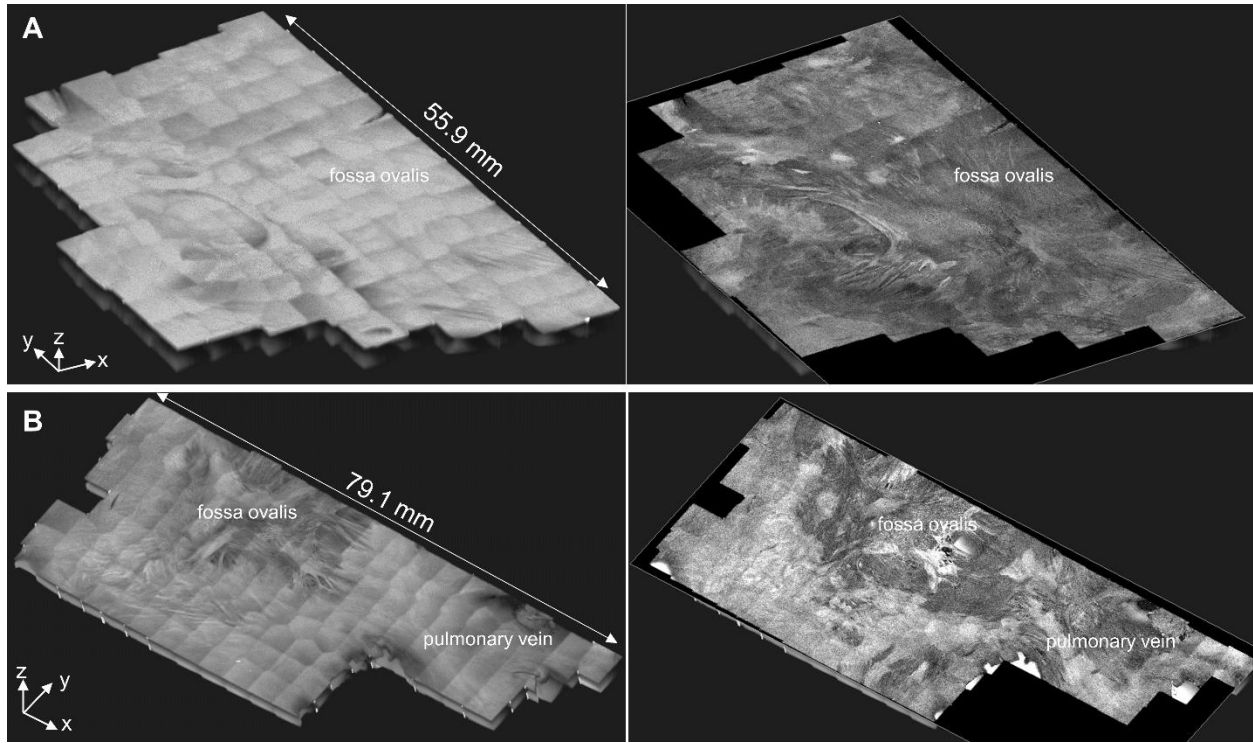
Figure 2.5. 3D reconstructions of stitched image volumes from regions taken from A, Heart 9# and B, Heart #13. The left column shows the endocardial surface of the tissue, while the right column shows views at sub-endocardial depths, demonstrating sub-surface structural detail.

2.2.5.2 Endocardial Thickness Quantification

Because the visibility of myocardial features such as myofiber orientation and collagen fibers in OCT is sensitive to the thickness of overlying connective tissue, measurements of endocardial thickness were acquired to identify the maximum endocardial thickness under which myocardial features could be seen within this OCT system's imaging depth. Such measurements also enabled comparison between histology and OCT measurements of endocardial thickness. Measurements

were obtained from the venoatrial junctions, where fiber orientation and collagen fibers could be commonly observed in OCT. Because variations of endocardial thickness occur around a single venoatrial junction, measurements of endocardial thickness were obtained from three points per pulmonary vein. These points were taken from regions where fibrosis and fiber orientation were visible at the venoatrial junction as determined from the *en face* OCT images. Three measurements were measured manually from OCT B-scans, calculated using a refractive index of 1.4 for atrial tissue, with another three measurements acquired from corresponding histology images for comparison.

2.2.5.3 Adipose Tissue Quantification

Adipose was manually segmented with IMOD [138] within each *en face* image where adipose was present. The presence of adipose was determined by a brightly spotted or "honeycomb" pattern, typically with a background of decreased intensity than surrounding myocardium. Adipose thickness was determined by summing the segmented voxels in the axial direction and converting the summed values to real dimensions based on the axial resolution. Overall adipose tissue volume was computed for each left atrium in which all major regions of the left atrium were imaged with OCT. Additionally, because the interatrial septum in particular was found to contain significant adipose deposits, the adipose tissue volume in only the septum region was computed.

2.2.5.4 Myofiber and Texture Quantification

The distribution of collagen fibers in the myocardium varied from region to region, particularly in the myocardial sleeves of the pulmonary veins. To provide a quantitative measure of these differences, texture analysis was carried out in the myocardial regions of representative pulmonary veins. A 4.0 x 8.6 x 0.1 mm region of interest was extracted from the myocardial region of the pulmonary veins. Within each B-scan in the 3D region of interest, the local range, standard

deviation, and entropy were computed with a 3 x 3 kernel, and these values were averaged over the entire region of interest. Fiber orientation angles were also extracted from each *en face* image over depth in the region of interest, using a previously described gradient-based method [95]. The circular standard deviation was calculated from all of the extracted angles in the 3D region of interest to quantify variation in fiber orientation. Fiber orientation angle extracted using the gradient-based method was also plotted against depth to quantify transmural trends. For overall fiber orientation trends over large regions, fiber orientation was demarcated manually based on visual striations observed within the *en face* OCT images at a single representative depth.

2.2.5.5 Registration of OCT Maps to Atrial Anatomy

Registration of white light and *en face* OCT images to a 3D left atrium model was carried out to facilitate interpretation of image features of dissected tissue with respect to overall left atrial anatomy. Registration was carried out in the open-source, 3D computer graphics software Blender. The registration procedure is depicted in Figure 2.6. A 3D left atrium model from the Continuity 6 online database, developed by the Cardiac Mechanics Research Group of the University of California San Diego, was used as a reference left atrium model. [139]

White light images were mapped to the model first because anatomical landmarks used for registration could be more easily identified in the white light images as opposed to the OCT images. Knowledge of the location of cuts made during dissection, as well as anatomical landmarks, such as the pulmonary veins and left atrial appendage, facilitated the wrapping of the white light images of the dissected tissues back into a 3D form. The mapping was carried out using Blender's UV mapping interface, where white light images were manually registered to the appropriate faces of the mesh. To provide a smooth visualization, histogram equalization and illumination correction were carried out for the white light images of each heart. Illumination

correction was accomplished by converting the white light images from RGB to the HSV domain. Within the HSV domain, the average illumination, calculated as the average of the V channel, was computed over the entire white light image. Regional illumination was then computed by Gaussian filtering the V channel with a 200 x 200 kernel and a 100 pixel standard deviation. The regional illumination was replaced by the uniform, average illumination by subtracting the Gaussian filtered V channel from the original V channel and adding the overall average of the original V channel.

After the white light images were registered to the model, OCT *en face* images could be manually registered to the white light images based on anatomical landmarks and the shape of the imaged region, and then subsequently registered to the model with an identical procedure. The *en face* OCT images simply replace the texture data of the model in lieu of the white light images. Similarly, any parameters derived from the OCT images, such as adipose tissue thickness and fiber orientation, could be registered to the 3D model with the same approach.
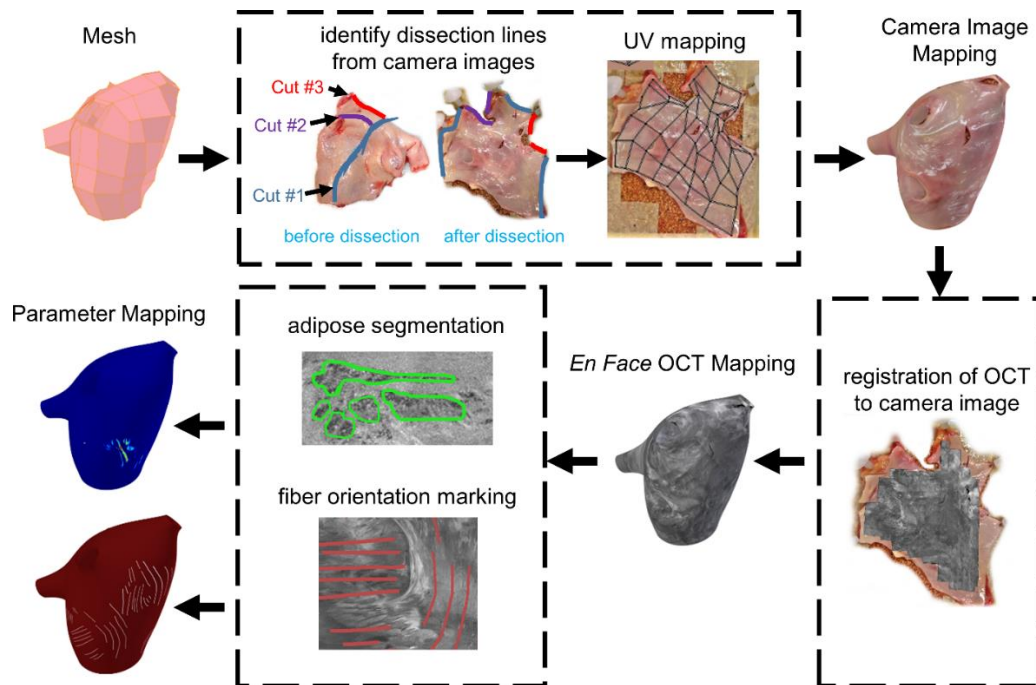
Figure 2.6 Overview of registration of OCT image maps to the 3D model.

2.2.5.6 Statistical Analysis and Whole Human Heart Cardiac Atlas

The left atrial imaging data acquired within this study was also combined with OCT imaging of other chambers, including the right atria and ventricles. The combined dataset contains OCT images obtained from 50 human hearts, and this full dataset comprises the whole human cardiac OCT imaging atlas. The same OCT imaging system as previously described was used to obtain the data from the other chambers. For this study, about two to three image volumes were selected per chamber for each heart. Histology was obtained as previously described and registration of OCT and histology was performed by two investigators, blind to the classification results, under the guidance of a pathologist. Overall, 573 pairs of OCT-histology matches were made in the full cardiac atlas.

Based on the OCT-histology pairings, features from regions with known tissue types were extracted. In each OCT image, key features including attenuation coefficient, contrast, correlation, energy, homogeneity, standard deviation, skewness, and kurtosis were calculated. Attenuation coefficients, μt, was measured based on a previously described model. [140] Attenuation coefficient characterizes how easily a material or medium can be penetrated by a beam of light. Contrast, correlation, energy, and homogeneity were extracted from gray level co-occurrence matrices (GLCM). These features quantify texture patterns within OCT images, such as local variation, joint pixel distribution, and uniformity. In addition, statistics of pixel distribution; such as standard deviation, skewness, and kurtosis; were included. The tissue types included in this study were collagen, normal myocardium, adipose, and fibrotic myocardium. The feature extraction was performed in a region of interest from each B-scan with a size of 320 by 160 µm. Statistical differences between groups were examined using ANOVA analysis, in Prism 8, GraphPad. The features were input to a classifier that has been previously described. [118]

2.3 Results

2.3.1 Endocardium

In general, the endocardium in OCT was characterized by a highly backscattering, homogeneous layer on the tissue surface. When the entire thickness of the endocardium was within the imaging penetration depth, a sharp transition from the highly backscattering upper layer to a lower intensity region underneath could be observed, indicating a transition to myocardial tissue as shown in Figure 2.7A. This distinct boundary between the upper layer of connective tissue and the myocardium underneath can also be applied to myocardium underneath venous media. Because the venous media and endocardium blend at the venoatrial junction, connective tissues overlying myocardium will hereafter always be referred to as endocardium for simplicity, unless it is necessary to distinctly specify the presence of venous media.

The boundary between the endocardial and myocardial layers enabled identification of endocardial thickness. However, if the endocardium was thicker than the penetration depth, a gradual fall-off of intensity in the upper layer was observed instead, as shown in Figure 2.7B. Significant myointimal thickening, consisting of a layer of loose collagen and myointimal cells on the tissue surface, could be identified by a second, highly backscattering layer with a well-delineated boundary with the endocardial layer underneath, as shown in Figure 2.7C.

36
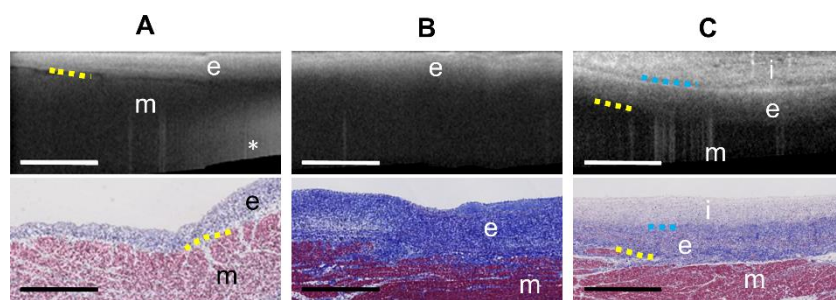
Figure 2.7. OCT B-scans (top) and corresponding Trichrome histology (bottom), showing OCT image textures and layer patterns corresponding to different endocardial and myocardial compositions. A, Endocardium with thickness within OCT depth penetration. B, Endocardium with thickness beyond OCT depth penetration. C, Endocardium with myointimal thickening. Dotted yellow lines show representative regions of transition between the endocardium and myocardium. Dotted blue lines show representative regions of transition between loose collagen with myointimal cells and the endocardium. Scale bars represent 1 mm. e = endocardium; m = myocardium; i = loose collagen and myointimal cells; asterisk = imaging artifact from the sample z-Spacer.

2.3.2 Adipose

Adipose tissue is highly recognizable within OCT images with a distinct "honeycomb" texture that can also become a speckled or brightly dotted texture if further from the imaging focus. Within the OCT imaging data of the whole human left atrium, adipose tissue could typically be observed in specific locations, which are summarized in Figure 2.8. Adipose tissue was often seen in a thin layer underneath the venous media and above the myocardium within the myocardial sleeves, shown in Figure 2.8A, as well as in the fibrofatty adventitia of the pulmonary veins as seen in Figure 2.8B. Adipose tissue was also markedly visible at the septum. Adipose tissue could exist in large pockets that transmurally spanned the atrial wall in thinner regions, shown in Figure 2.8C, and was particularly prominent inside and around the crescent wedge at the edge of the fossa ovalis. More generally, adipose tissue could be seen distributed throughout the interatrial septum in small pockets of varying sizes, as demonstrated in the adipose tissue thickness map of Figure 2.8E. These pockets could be seen directly underneath the endocardium within OCT, although could be connected to larger volumes of adipose tissue when compared to histology as shown in Figure 2.8F.
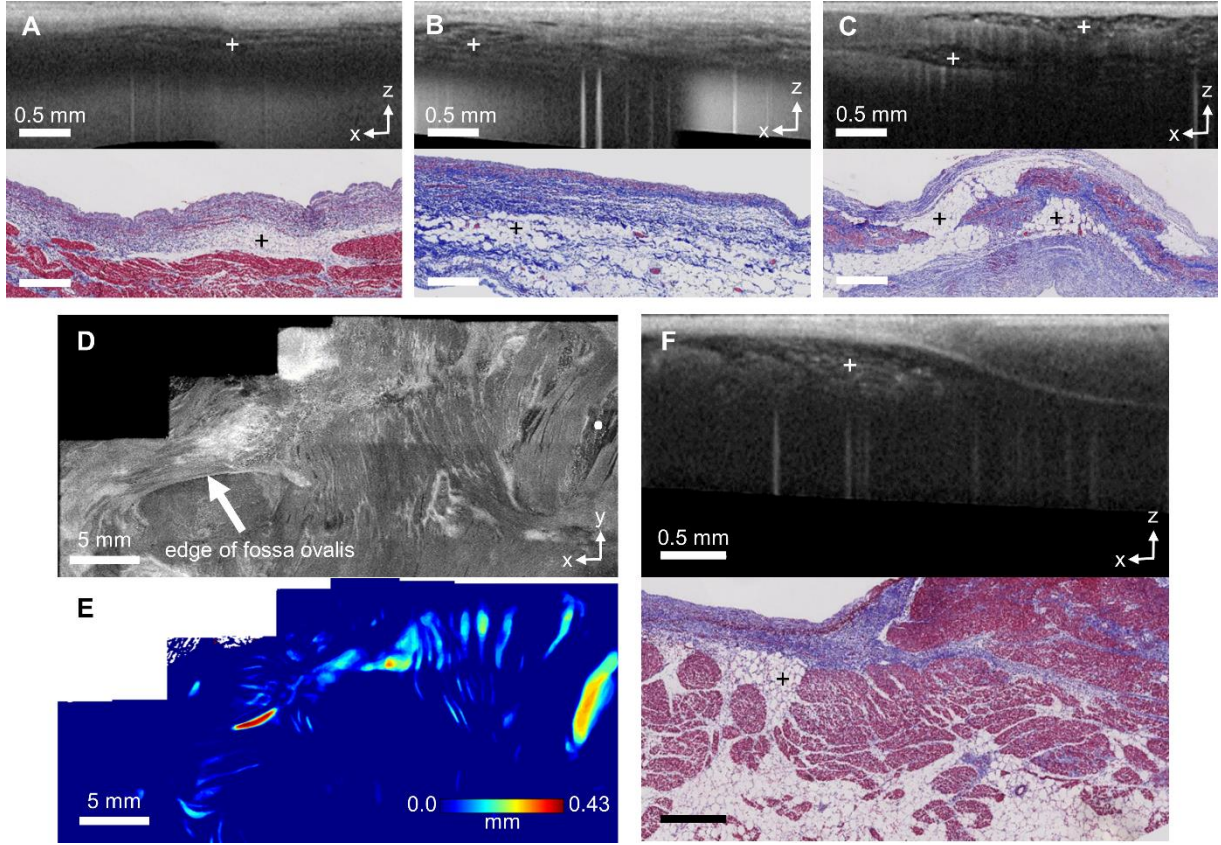
Figure 2.8. Adipose distributions in human left atrial tissue. A, OCT B-scan (top) and histology (bottom) of adipose overlying a myocardial sleeve in a pulmonary vein. B, OCT B-scan (top) and histology (bottom) of adipose from the fibro-fatty adventitia. C, OCT B-scan (top) and histology (bottom) of adipose tissue within the edge of the fossa ovalis. D, *En face* OCT image at the fossa ovalis, shown 0.26 mm from the endocardial surface, showing adipose tissue distributed over a wide area. The white dot corresponds to the location of the B-scan shown in F. E, Corresponding adipose thickness map to D. F, OCT B-scan (top) and histology (bottom) of adipose near the fossa ovalis. The crosses indicate regions of adipose tissue.

The amount of adipose tissue as imaged by OCT was variable among hearts, particularly at the septum due to the large amount of adipose tissue observed there. Adipose tissue was proliferous in some left atria and almost non-existent in others. The total thickness and volume of adipose across comprehensively imaged left atria is provided in Table 2.2. The maximum thickness of adipose tissue, about 0.4 mm, was typically limited by the imaging depth of OCT. Note that

38

variability in total adipose tissue volume over the whole heart could depend on the length of the pulmonary veins that were still intact upon heart acquisition, which varied from specimen to specimen. However, the total volume of adipose tissue specifically within the region of the interatrial septum also varied greatly. Representative registrations of adipose tissue thickness maps to the left atrium model are shown in Figure 2.9. As described previously, adipose tissue could be seen to cluster primarily around the septum, with some distributions around the pulmonary veins. Adipose tissue distant from these two locations were only observed in heart #14, shown in Figure 2.9E, which showed significant amounts of adipose tissue spanning a large distance of the left atrial wall underneath the left superior pulmonary vein and adjacent to the left atrial appendage.

Table 2.2. Adipose Measurements

Heart #	Max Thickness (mm)	Total Volume (mm^3)	Total Volume at Septum (mm^3)
9	0.36	4.82	4.82
10	0.26	2.01	1.69
12	0.42	18.10	5.69
13	0.38	11.77	7.52
14	0.40	28.74	11.57
15	0.20	1.42	1.26
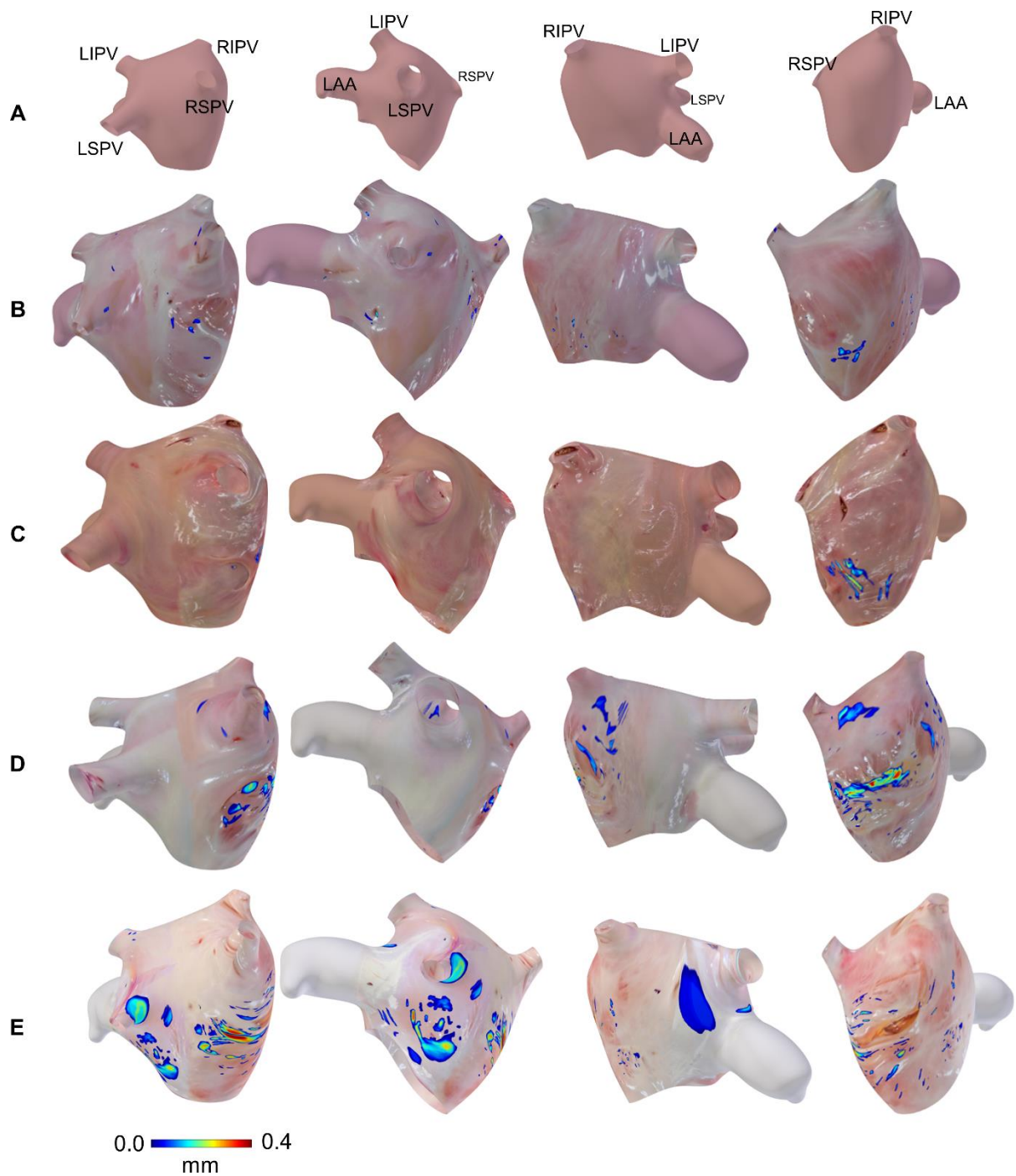
Figure 2.9. Adipose thickness distributions in human left atria, as extracted from endocardial OCT images and superimposed on a 3D left atrium model. The adipose thickness is shown as a color map, while areas where adipose was not seen instead show camera images of the left atrial tissue. The models are shown in four views to show the entirety of the left atrium. A, Reference model, showing the location of the pulmonary veins and left atrial

appendage relative to the model's orientation. B, Adipose thickness distribution from Heart #15. C, Adipose thickness distribution from Heart #9. D, Adipose thickness distribution from Heart #13. E, Adipose thickness distribution from Heart #14.

2.3.3 Myofiber Orientation and Collagen fibers

Collagen fibers within the myocardium could be identified by backscattering strands within regions of myocardium. Figure 2.10 shows a stitched image region where fiber organization could be identified at sub-endocardial levels. Figure 2.10A shows an *en face* image still within the endocardium, showing a smooth pattern. Figure 2.10B displays a region deeper within the tissue, revealing the fiber information, which is also seen in a B-scan view in Figure 2.10C. However, fiber orientation could not be identified in regions where the endocardial thickness was beyond the imaging penetration depth, as shown in Figure 2.10D.
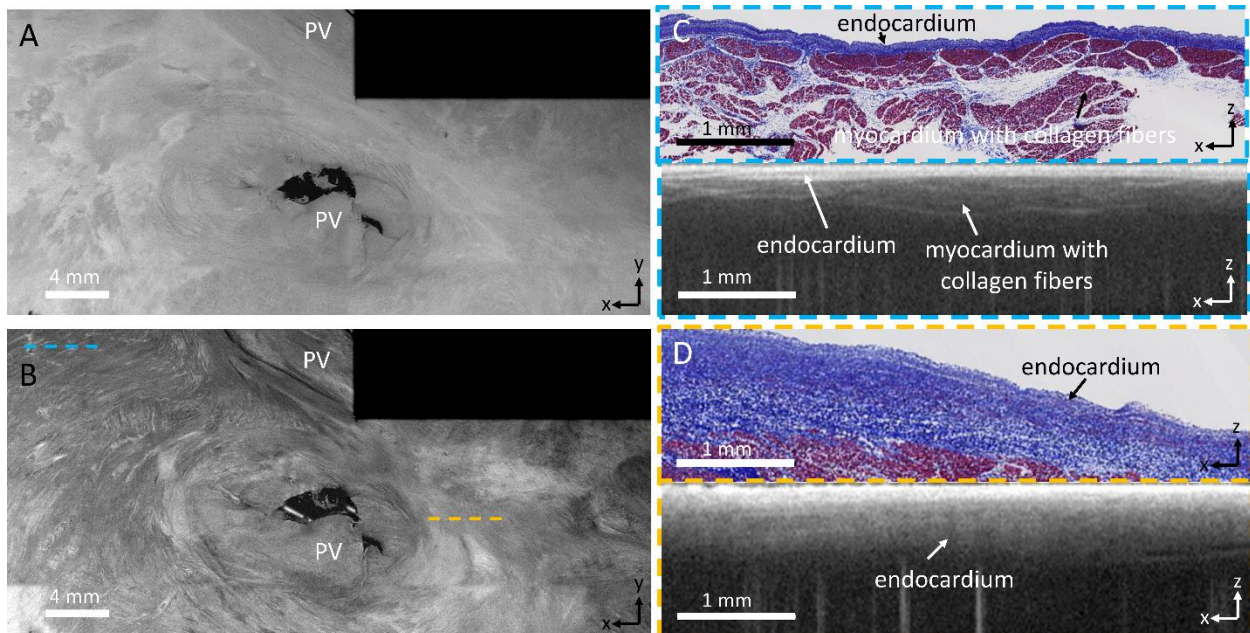
Figure 2.10. A, *En face* OCT image, 0.07 mm and B, 0.27 mm from the endocardial surface. C, histology and corresponding stitched OCT B-scan in region with rich collagen fiber information; D, histology and corresponding stitched OCT B-scan with thick endocardium and less fiber information.

41

When shown in the *en face* view, striations within the OCT images could be correlated to fiber orientation seen in corresponding *en face* histology images, demonstrated in Figure 2.11A-B. *En face* views revealed myofiber and collagen fibers wrapping around pulmonary veins in different directions, as shown in Figure 2.11C-D. In particular, in Heart #11, transmural changes in myofiber orientation could be clearly observed, shown in Figure 2.11E-F where the fiber orientation changed by nearly 60° at different depths. The extracted profile of fiber orientation over depth shown in Figure 2.11G shows an abrupt change in fiber orientation, which is consistent with prior findings of transmural left atrial myofiber patterns. [58]
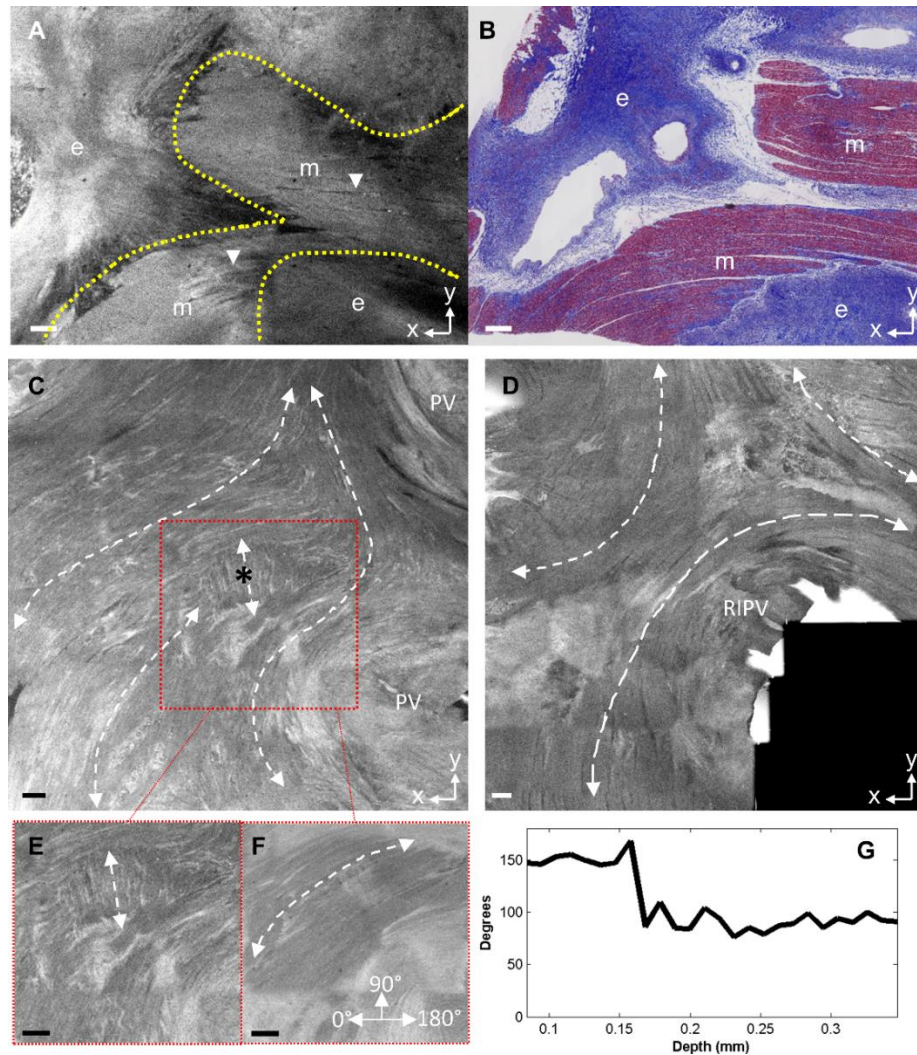
Figure 2.11. *En face* OCT and histology images, showing fiber orientation. A, OCT *en face* image, shown 0.39 mm from the tissue surface. B, Corresponding *en face* histology image. Dotted yellow lines in the OCT image show boundaries between regions of endocardium and myocardium. White arrowheads indicate striations indicative of fiber orientation in OCT. C, OCT *en face* image, shown 0.30 mm from the tissue surface. D, OCT *en face* image, shown 0.38 mm from the tissue surface. E, Region within the dotted red box shown in C, at a depth of 0.29 mm. F, Region within the dotted red box shown in C, at a depth of 0.17 mm. G, Fiber angle over depth at the point indicated by the black asterisk in C. White double-sided arrows indicate general fiber orientation trends. All scale bars indicate 1 mm.

To obtain a measure of the maximum endocardial thickness under which myocardial features could be visualized with this OCT system, measurements of endocardial thickness were obtained in regions where fiber orientation could be seen in the *en face* OCT images of pulmonary vein myocardial sleeves. Out of 32 pulmonary veins in which measurements were made, 23 veins had areas of sufficiently thin endocardial thickness to observe fiber orientation in the *en face* images of the venoatrial junction. In 3 left superior, 2 left inferior, 3 right superior, and 1 right inferior pulmonary vein, fiber orientation was unable to be observed in the *en face* OCT images at the venoatrial junction. The endocardial thickness measurements are shown in Table 2.3. The average thickness under which fiber orientation could be observed was 0.28±0.06 mm as measured from OCT, and 0.31±0.08 mm as measured from histology, overall for all veins. The range of measurements were 0.15 to 0.43 mm and 0.12 to 0.47 mm for OCT and histology, respectively.

Table 2.3 Endocardial Thickness, where Myocardium within OCT Imaging Depth

	Thickness (mm)			
	LSPV (n=15)	LIPV (n=18)	RSPV (n=15)	RIPV (n=15)
OCT	0.28±0.04 (0.2 to 0.39)	0.30±0.05 (0.22 to 0.41)	0.28±0.07 (0.15 to 0.39)	0.28±0.06 (0.20 to 0.43)
Histology	0.30±0.09 (0.13 to 0.47)	0.35±0.05 (0.25 to 0.43)	0.30±0.09 (0.13 to 0.43)	0.32±0.07 (0.20 to 0.44)

Values are given as mean ± standard deviation (range). LIPV: left inferior pulmonary vein; LSPV: left superior pulmonary vein; RIPV: right inferior pulmonary vein; RSPV: right superior pulmonary vein; OCT: optical coherence tomography

Representative mappings of fiber orientation, as extracted from manual measurements, to the 3D left atrial model are presented in Figure 2.12. Given OCT's imaging depth, fiber orientation information could most often be extracted from the septal region and around the pulmonary veins. Consistent with findings from gross inspection and DT-MRI, fibers often wrapped circumferentially around the pulmonary vein ostia [58, 121]. Within hearts #13 and #14, fiber orientation wrapping around the right pulmonary veins with obliquely running fibers between the pulmonary veins and fiber orientation circumferential to the waist of the left atrium underneath, as seen on the far right in Figure 2.12D and E, is also consistent with observations from DT-MRI data. [58] Overlapping fiber bundles could be seen in high detail, such as seen in the inset of Figure 2.12B and in the corresponding OCT *en face* image in Figure 2.21.
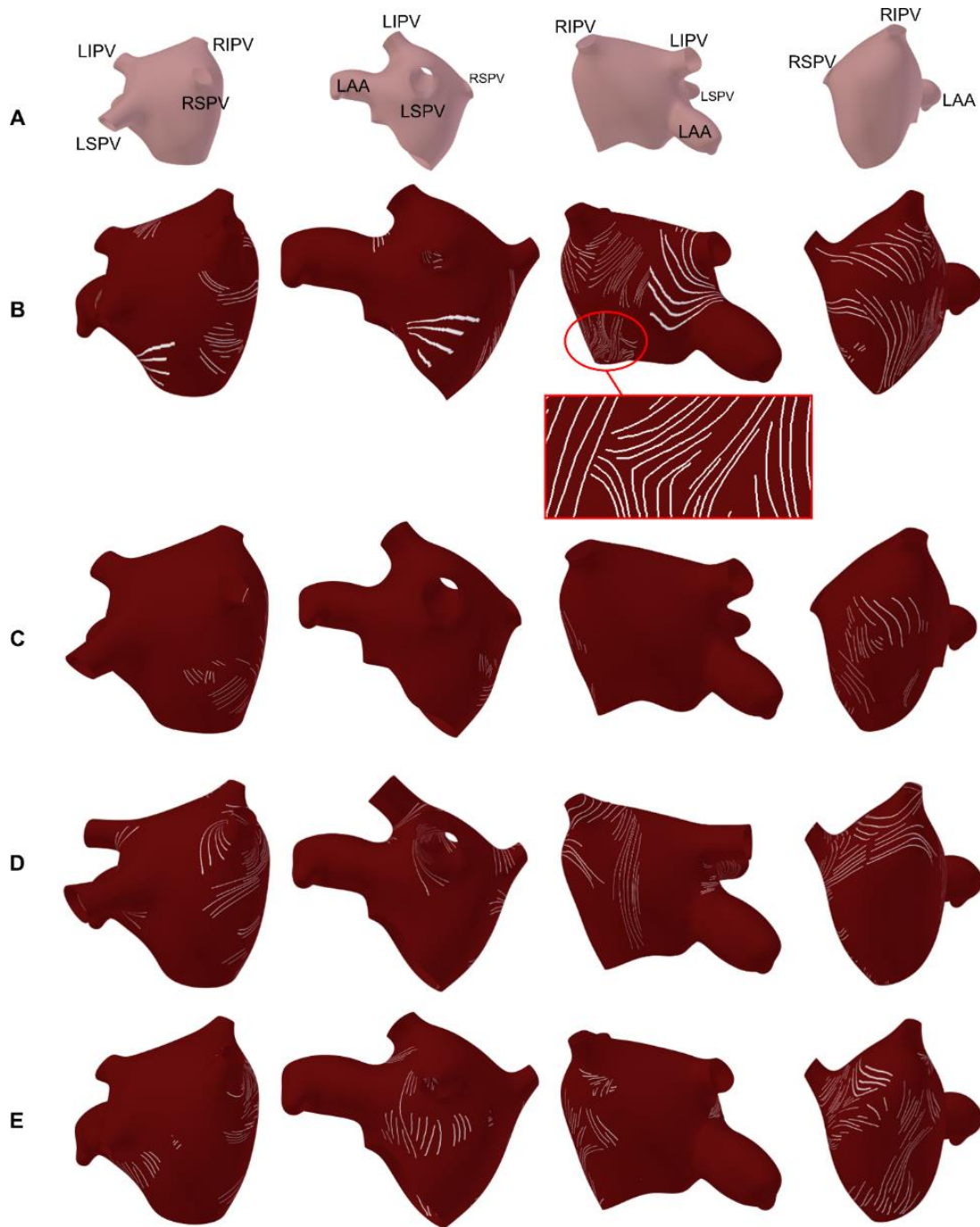
Figure 2.12. Fiber orientation in the human left atria, as extracted from OCT images and superimposed on 3D anatomical models. A, Reference model, showing the location of the pulmonary veins and left atrial appendage relative to the view. B, Fiber orientation from Heart #15. C, Fiber orientation distribution from Heart #9. D, Fiber orientation distribution from Heart #13. E, Fiber orientation distribution from Heart #14.

2.3.4 Pulmonary Veins

In regions of the pulmonary veins consisting of the venous endothelium, media, and adventitia, the OCT images typically showed a more heterogeneous texture and a deeper penetration depth with a gradual fall-off of intensity. The specific texture of the venous tissues could vary between pulmonary veins based on the composition and density of fibrous tissues within the region. For example, in Figure 2.13A, the venous media and adventitia have a speckled appearance, while Figure 2.13B instead shows a highly backscattering upper layer with additional bands underneath. Finally, some pulmonary veins consisting of dense connective tissue had a more homogeneous texture and gradual signal fall-off, similar to regions of thick endocardium as shown in Figure 2.13C.
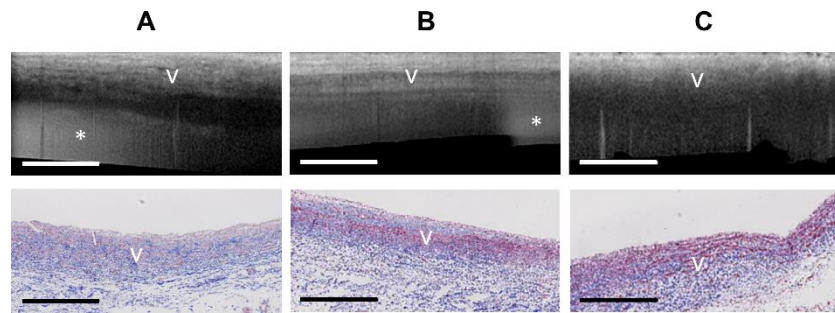
Figure 2.13 OCT B-scans (top) and corresponding Trichrome histology (bottom), showing differences in OCT image texture corresponding to venous media and adventitia with different densities and distributions of connective tissue. A, Venous media and adventitia with a speckled image texture in OCT. B, Venous media and adventitia with a layered image texture in OCT. C, Venous media and adventitia with a smooth homogeneous image texture. Scale bars represent 1 mm. v = venous media; asterisk = imaging artifact from the sample z-Spacer.

Given the distinct image features of different tissue compositions as described above, regions of myocardial sleeves could be differentiated from pulmonary vein regions containing only venous endothelium, media, and adventitia. The transition from myocardium to adventitia, where the myocardial sleeve ends, could typically be identified by at least one of two ways. First, the

sharp boundary between the endocardium and myocardium became more diffuse when entering regions containing only venous media and adventitia, often accompanied by an increase in penetration depth. Second, a more heterogeneous image texture was typically seen with venous media and adventitia compared to endocardium and myocardium. Representative examples are described below, showing how the myocardial sleeves, as well as fibrosis and variations in endocardial thickness, could be observed.

In Figure 2.14, the distinct layer boundary disappears and the penetration depth increases once entering the region of only venous endothelium, media, and adventitia, as seen towards the right of the B-scan of Figure 2.14B. The *en face* view in Figure 2.14A also shows a clear difference in texture and backscattering between the myocardial region on the left and the region without myocardium on the right of the dashed green line. Collagen distributed between myofibers, as seen from histology, were identifiable by highly backscattering strands within OCT, with the parallel directionality of the fibers clearly defined. The 3D ROI from which texture and fiber orientation statistics were extracted is represented in the x-y and x-z planes by the blue boxes in Figure 2.14A and Figure 2.14B. The mean local range in the myocardial ROI was 5.37, the mean local standard deviation was 1.81, and the mean local entropy was 3.07. The circular standard deviation of extracted fiber orientation angles was 17.03°.
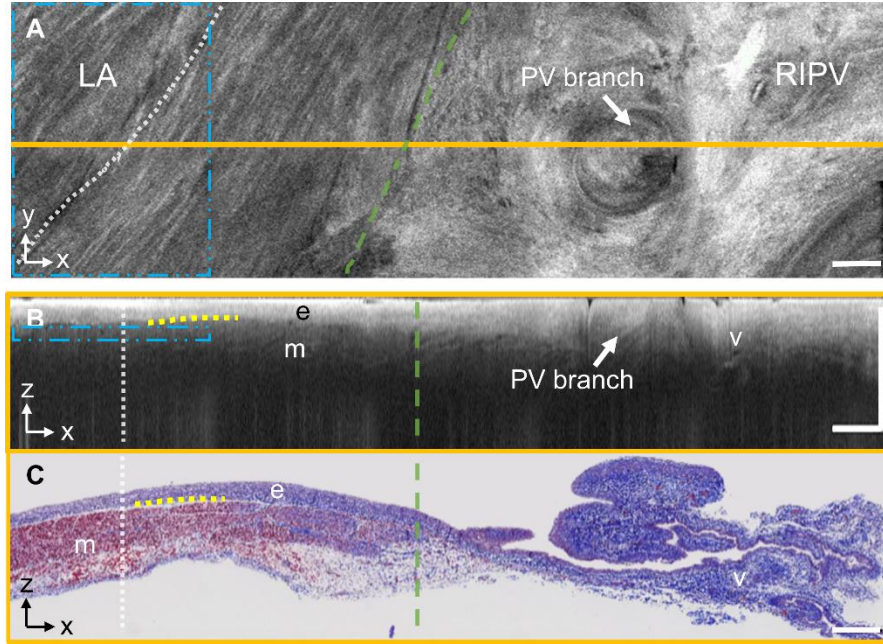
Figure 2.14. OCT imaging of a venoatrial junction and corresponding histology, showing change in depth penetration near the end of the myocardial sleeve. A, Stitched *en face* region, shown 0.34 mm from the tissue surface. B, Stitched B-scan corresponding to the orange line in A. C, Corresponding Trichrome histology to B. Dotted white lines show the approximate location of the PV ostia. Dashed green lines show the approximate area of transition from myocardium to venous media and adventitia. Dotted yellow lines show representative regions of transition between the endocardium and myocardium. The blue dotted boxes represent the 3D ROI from which texture and fiber orientation statistics were calculated. All scale bars indicate 1 mm. LA = left atrium, RIPV = right inferior pulmonary vein; e = endocardium; m = myocardium; v = venous media.

In Figure 2.15, the region containing only venous endothelium, media, and adventitial tissues has a more heterogeneous texture, with more variations in intensity and an almost hatched pattern as seen in the *en face* view of Figure 2.15A. The change in image texture is also noticeable in the B-scan shown in Figure 2.15B, where the region without myocardium includes additional bands underneath the upper layer.
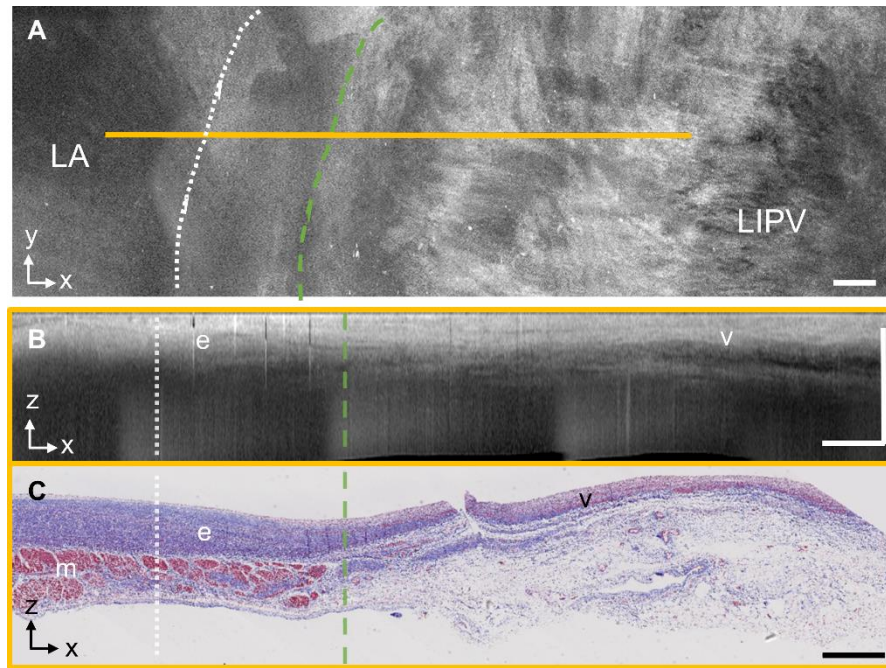
Figure 2.15 OCT imaging of a venoatrial junction and corresponding histology, showing change in image texture near the end of the myocardial sleeve. A, Stitched *en face* region, shown 0.50 mm from the tissue surface. B, Stitched B-scan corresponding to the orange line in D. C, Corresponding Trichrome histology to E. Dotted white lines show the approximate location of the PV ostia. Dashed green lines show the approximate area of transition from myocardium to venous media and adventitia. Dotted yellow lines show representative regions of transition between the endocardium and myocardium. All scale bars indicate 1 mm. LA = left atrium, LIPV = left inferior pulmonary vein; e = endocardium; m = myocardium; v = venous media.

As demonstrated previously in Figure 2.13, different pulmonary veins had different textures corresponding to the venous endothelium, media, and adventitia, and other pulmonary veins had a speckled or striated texture as opposed to the hatched pattern seen above. A representative example is shown below in Figure 2.16. Adipose pockets were often observed. Note again the increase in depth penetration and diffuse fall-off, as demonstrated in the B-scan.
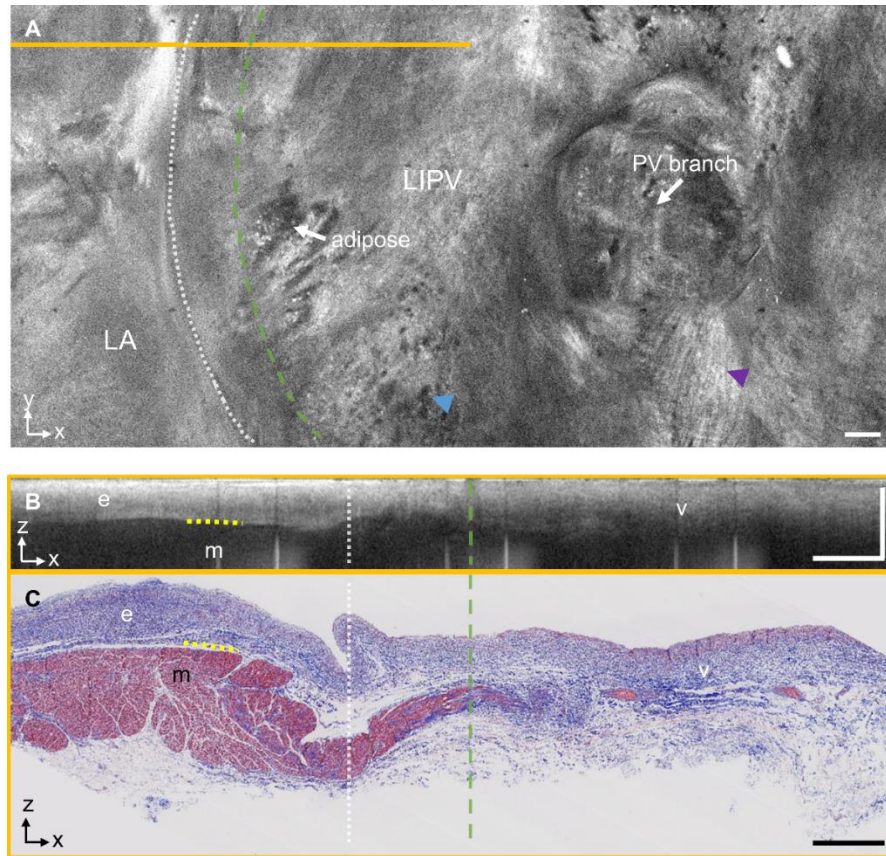
Figure 2.16 OCT imaging and corresponding histology of a venoatrial junction. A, Stitched en-face region, shown 0.51 mm from the tissue surface. B, Stitched B-scan corresponding to the orange line in A. C, Corresponding Trichrome histology to B. Dotted white lines show the approximate location of the pulmonary vein ostia. Dashed green lines show the approximate area of transition from myocardium to venous media and adventitia. Dotted yellow lines show representative regions of transition between the endocardium and myocardium. The blue and purple markers indicate speckles and striated textures, respectively. LA = left atrium; LIPV = left inferior pulmonary vein; e = endocardium; m = myocardium; v = venous media.

Another representative case showing distinct collagen fiber structure at the venoatrial junction is given in Figure 2.17. With OCT imaging, fibrotic myocardium could be identified past the pulmonary vein ostium and inside the venous region. The endocardial thickness could be seen to abruptly decrease inside the pulmonary vein area and significant focal thickening of endocardium was observed near the ostium, as seen in both the *en face* view in Figure 2.17A and

B-scan view in Figure 2.17B. Again, fibrotic collagen fibers could be identified by bright strands. Within this pulmonary vein, the fibrotic collagen fibers varied more greatly in size and directionality compared to those shown in Figure 2.14A. Similar patterns of complex fibrosis were observed in the LSPV and LIPV of heart #13. The depth penetration increases at the far right of the B-scan in Figure 2.17D, signaling the end of the myocardial sleeve and transitioning to a region containing only the endothelium, venous media, and adventitial tissues. The 3D ROI from which texture and fiber orientation statistics were extracted is represented in the x-y and x-z planes by the blue boxes in Figure 2.17C and Figure 2.17D. The mean local range in the myocardial ROI was 4.88, the mean local standard deviation was 1.65, and the mean local entropy was 2.89. The circular standard deviation of extracted fiber orientation angles was 35.17°.
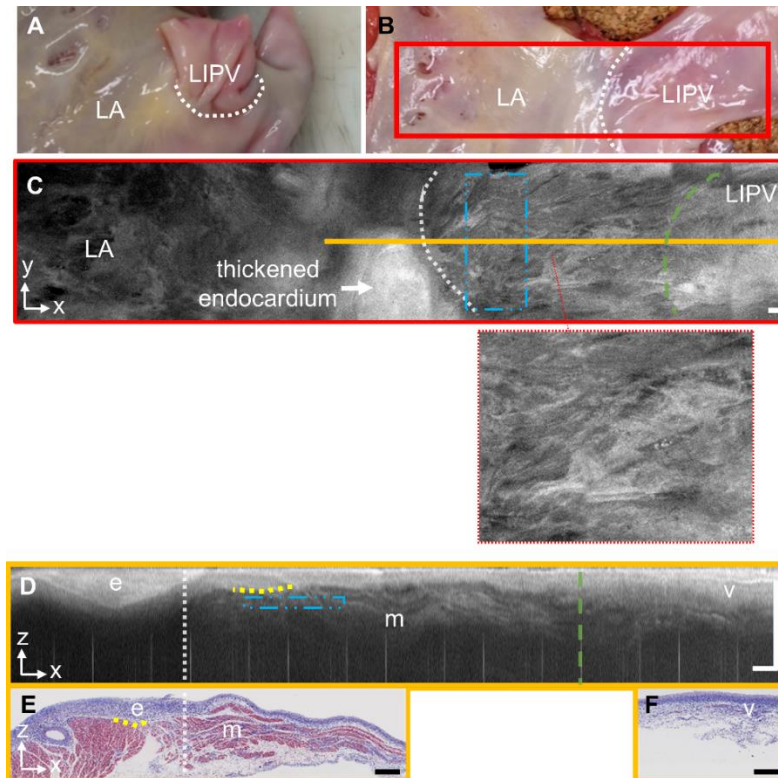
Figure 2.17. OCT imaging of a venoatrial junction and corresponding histology, showing changes in endocardial thickness and depth penetration, as well as fibrosis. A, LIPV, prior to dissection. B, LIPV from A, post-dissection. C,

51

En face region, shown 0.39 mm from the tissue surface, corresponding to the red box in B. A zoomed in view of a sub-region is shown to show details of the fibrosis patterns. D, Stitched B-scan corresponding to the orange line in C. E & F, Corresponding Trichrome histology to D. Dotted white lines show the approximate location of the PV ostia. Dashed green lines show the approximate area of transition from myocardium to transmural connective tissue. All scale bars indicate 1 mm. Dotted yellow lines show representative regions of transition between the endocardium and myocardium. The blue dotted boxes show the ROI from which texture and fiber orientation statistics were calculated. LA = left atrium; LIPV = left inferior pulmonary vein; e = endocardium; m = myocardium; v = venous media.

Endocardial thickness and composition of the venous media and adventitia varied between pulmonary veins and among different regions of a single pulmonary vein. There were some cases in which it was difficult to distinguish the myocardial sleeves from venous regions without myocardium. Figure 2.18 presents two representative cases. In Figure 2.18A, the increase in depth penetration due to myointimal thickening could deceptively be interpreted as a region consisting of only venous endothelium, media, and adventitia despite myocardium being present underneath. In Figure 2.18C, the upper layer boundary becomes more diffuse, but the penetration depth remains similar throughout, making identification of the end of the myocardial sleeve unclear. The ability to differentiate regions of myocardial sleeves to regions without myocardial sleeves, based on qualitative OCT image features, was generally determined for each pulmonary vein by a single observer not blinded to the histology. Out of 32 pulmonary venoatrial junctions, it was determined the myocardial sleeves could be differentiated from venous regions without myocardial sleeves in 18 cases while 6 cases were ambiguous. In the remaining 8 cases, the pulmonary veins had been cut short such that only the myocardial sleeves could be imaged, with no transition to venous regions without myocardium, and thus were not counted.
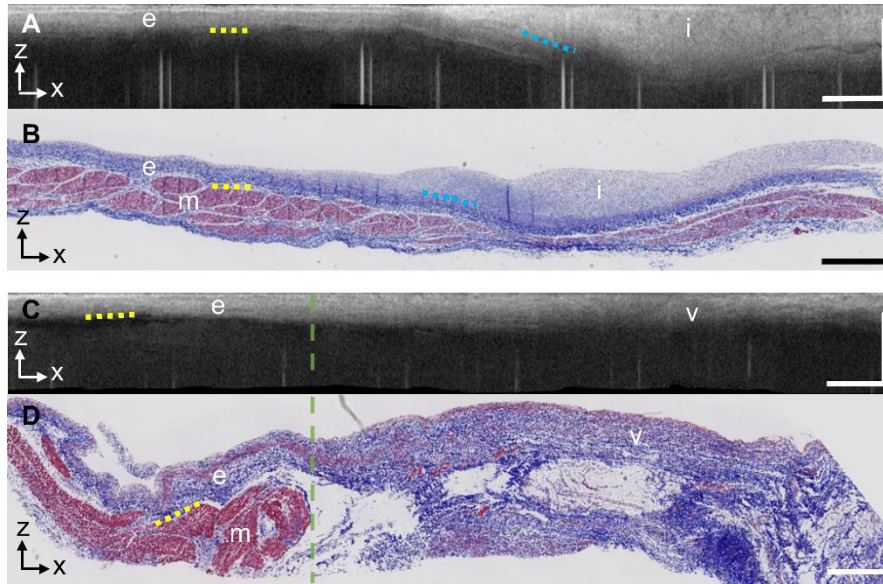
Figure 2.18. Cases where identification of pulmonary vein sleeves is ambiguous in OCT imaging. A, OCT B-scan near the LIPV from heart #15. B, Corresponding Trichrome histology to A. C, OCT B-scan near the LSPV from heart #12. D, Corresponding Trichrome histology to C. Dotted yellow lines show representative regions of transition between the endocardium and myocardium. Dotted blue lines show representative regions of transition between loose collagen with myointimal cells and the endocardium. Dashed green lines show the approximate area of transition from myocardium to transmural connective tissue. All scale bars indicate 1 mm. e = endocardium; m = myocardium; i = loose collagen and myointimal cells.

In a few hearts, the adventitial side of the pulmonary vein was also imaged with OCT, and a representative figure is given in Figure 2.19. From the adventitia, OCT is able to capture the profuse regions of adipose tissue, covered by a layer of loose collagen, as well as the fibrous areas devoid of adipose, which are represented in OCT by a homogeneous region with a diffuse fall-off.
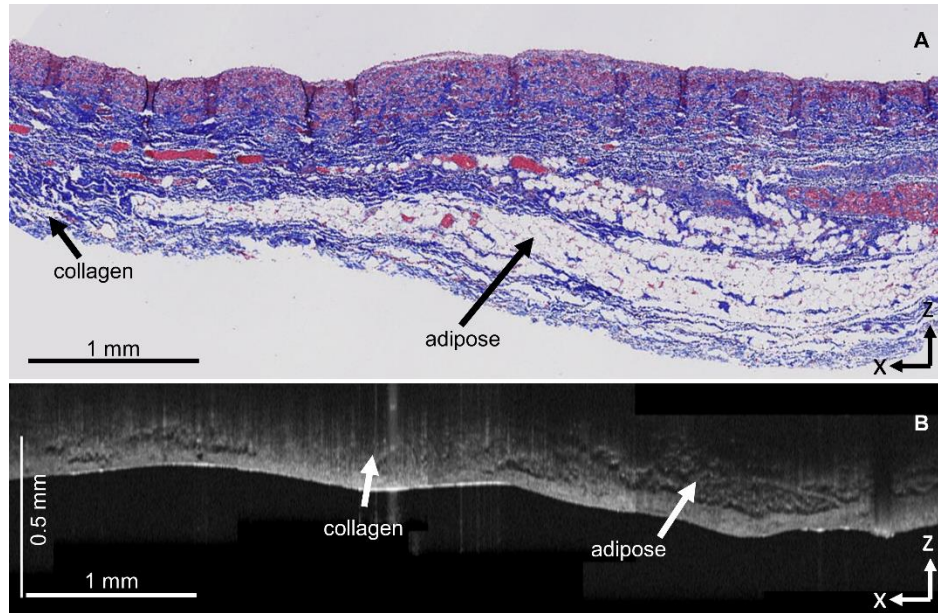
Figure 2.19. OCT imaging of the adventitial side of the pulmonary vein. A, Trichrome histology, and B, Corresponding OCT image.

2.3.5 Interatrial Septum

As described above, adipose tissue was often observed at the septum. The amount of adipose tissue at the septum could vary widely. In particular, it was noted in certain hearts, regions of abundant adipose and fibrous tissue at the fossa ovalis, visible from the white light images, could be imaged in more detail with OCT. A representative example is provided in Figure 2.20.
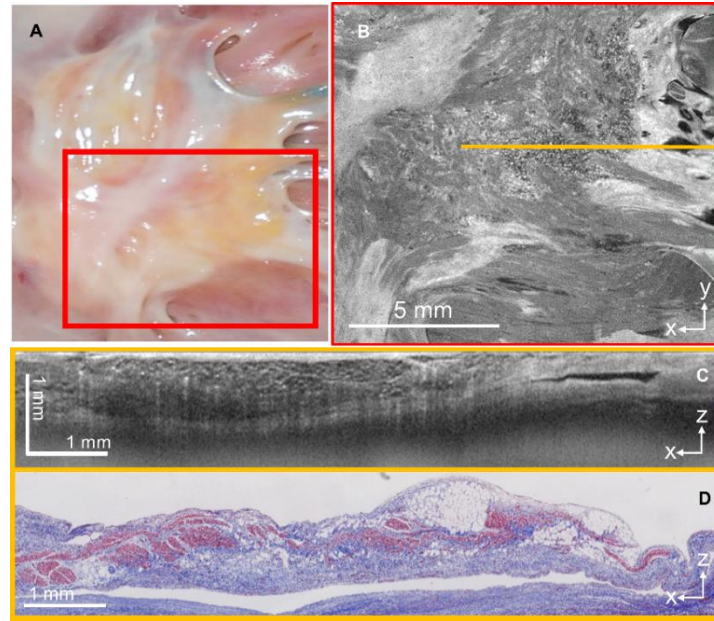
Figure 2.20. Representative example of significant amounts of adipose and fibrotic tissue at the fossa ovalis. A, Camera image of region of interest at the fossa ovalis. B, *En face* OCT image of the region depicted in the red box in A. C, OCT B-scan of the orange line in B. D, Corresponding histology to C.

Fiber orientation could also often be seen in varying patterns at the septum, with overlapping fiber bundles as observed in Figure 2.21.
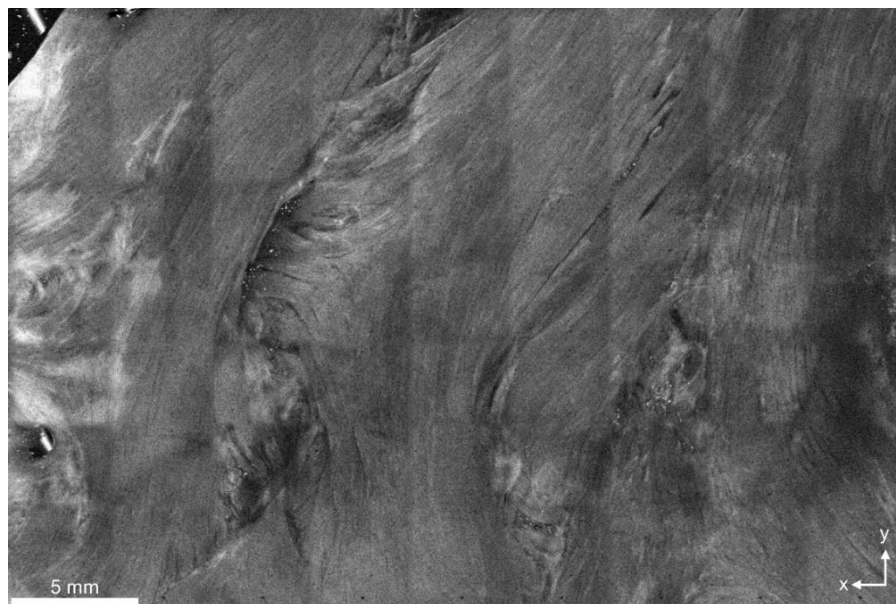
Figure 2.21. Fiber orientation as seen at the septum, shown 0.37 mm from the endocardial surface.

Notably, unlike in most regions of the left atrium, a transmural view of the left atrial wall could be seen in thinner regions of the fossa ovalis, as shown in Figure 2.22. The brighter layers of connective tissue could be seen on both sides of the myocardium.
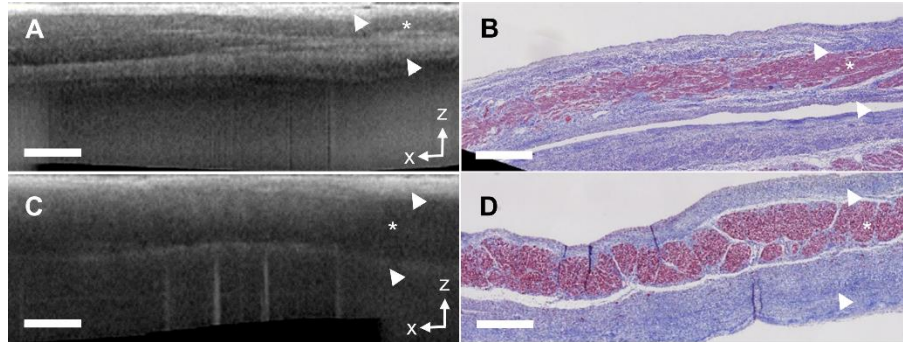
Figure 2.22. Structures at the left atrial fossa ovalis as seen transmurally by OCT. A, OCT B-scan at the edge of the fossa ovalis. B, Corresponding histology to A. C, OCT B-scan at the fossa ovalis. D, Corresponding histology to C. Scale bars indicate 0.5 mm. Asterisks indicate regions of myocardium. Arrowheads point to the endocardium on both sides of the wall.

2.3.6 Ablation Lesions

While work has been done in identifying ablation lesions using OCT, the imaging of ablation lesions within human left atrial tissue has not yet been evaluated. Therefore, a preliminary study of OCT imaging of ablation lesions in the human left atrium was carried out. Within OCT, the ablation lesions could correspond to regions of slightly greater penetration depth, as shown in Figure 2.23. However, the features were subtle and may not correspond to the full width of the lesion. The features of the ablation lesion were also dependent on the surrounding endocardial thickness and composition. While image processing may be able to reveal more unique characteristics, functional OCT modalities such as PS-OCT may be able to provide further useful information.

56
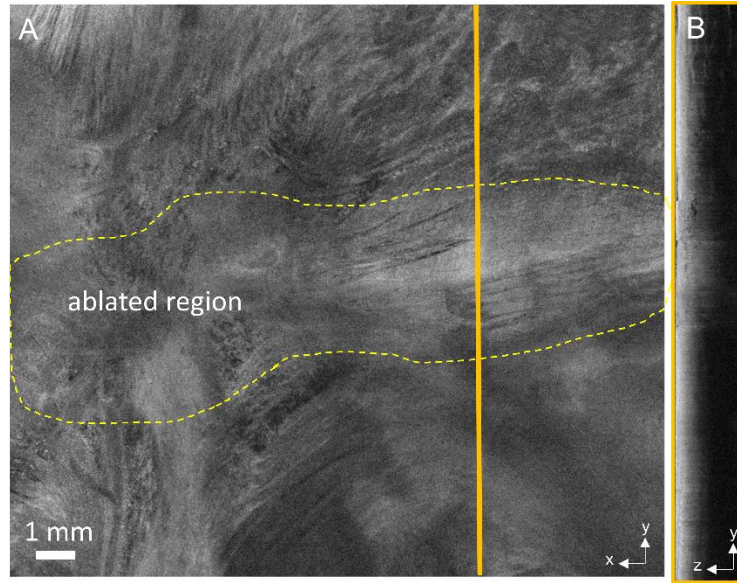
Figure 2.23. OCT imaging of ablation lesions within human left atrial tissue. A, *En face* OCT image, shown 0.38 mm from the endocardial surface. B, B-scan corresponding to the orange line in A.

2.3.7 Whole Human Cardiac Atlas

OCT imaging of the human left atrium contributes to a larger dataset including OCT imaging data from 50 human hearts. The donor characteristics for the whole human cardiac OCT dataset is provided in Table 2.4. Image features from OCT imaging of all chambers were evaluated both quantitatively and qualitatively.

Table 2.4. Donors Characteristics for Whole Human Cardiac OCT Atlas

Characteristic	Value
N	50
Demographic Profile	
Age in yrs, median (interquartile range)	62 (57.3– 67.0)
Female, n (%)	23 (46.0)
BMI, median (interquartile range)	30.4 (25.71 –36.01)
Medical History, n (%)	
Heart Failure	10 (20.0)
Cardiomyopathy	7 (14.0)
Coronary artery disease	11 (22.0)
Myocardial infarction	7 (14.0)

Atrial fibrillation	5 (10.0)
Chronic obstructive pulmonary disease	17 (34.0)
Diabetes	16 (32.0)
Hypertension	34 (68.0)
Cause of death, n (%)	
Cardiac arrest	17 (34.0)
Cardiopulmonary arrest	6 (12.0)
Respiratory arrest	3 (6.0)
Respiratory failure	4 (8.0)
Chronic obstructive pulmonary disease	3 (6.0)
Congestive heart failure	3 (6.0)

2.3.7.1 Features within Ventricles

Examination of ventricular OCT images revealed unique features for various tissue types as shown in Figure 2.24. Figure 2.24 A-F show images from ventricular free wall and Figure 2.24 G-L show images from the ventricular septum. In healthy hearts as shown in Figure 2.24A, D and G, L, the endocardium exhibited a narrow and highly backscattering band at the uppermost region of the tissue. The myocardium regions revealed a homogenous pattern in a darker region underneath. Fibrous infiltration was observed in both ventricular free wall and septum, as shown in Figure 2.24B, E and H, K, with rich collagen content within the myocardium. In diseased hearts with scar, a thickened endocardium as shown in Figure 2.24C, F was observed. In OCT, the scar region was represented by a highly backscattering region with a heterogeneous distribution of collagen density indicated by slightly varying intensity. In addition, adipose tissue, which is clearly identifiable by a honeycomb texture, occasionally exists in the ventricular septum, as shown in Figure 2.24I, L. The appearance of adipose tissue in the ventricle can be associated to arrhythmogenic cardiomyopathy.
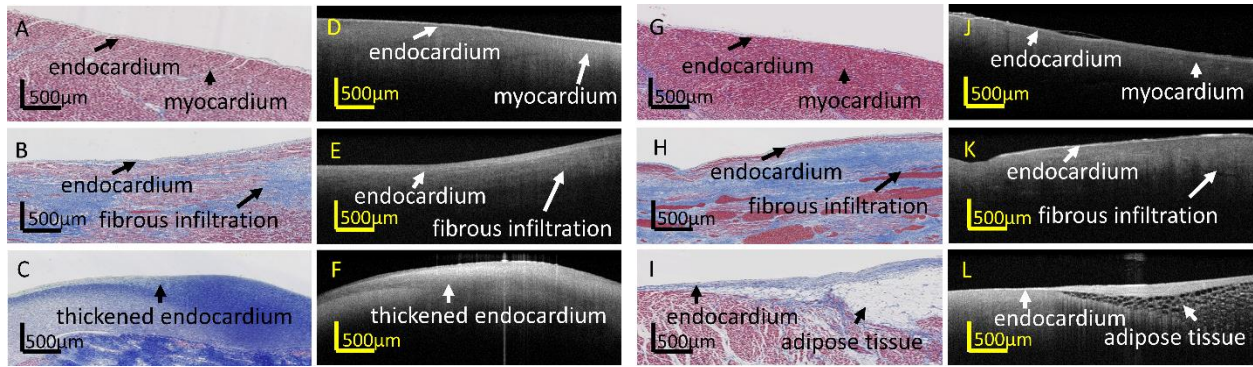
Figure 2.24. OCT images and corresponding histologic images of multiple substrates within (A-F) ventricular free wall and (G-L) ventricular septum.

2.3.7.2 Features within Right Atria

In the right atria, Figure 2.25, the endocardial band is typically narrower than those in left atria but thicker than those in ventricle. Due to the thinner endocardium, which allows photons to penetrate deeper, the myocardium in the right atria often corresponds to a higher intensity in OCT than in the left atria. Adipose tissue, again displaying a honeycomb structure, could also be observed in the right atria.
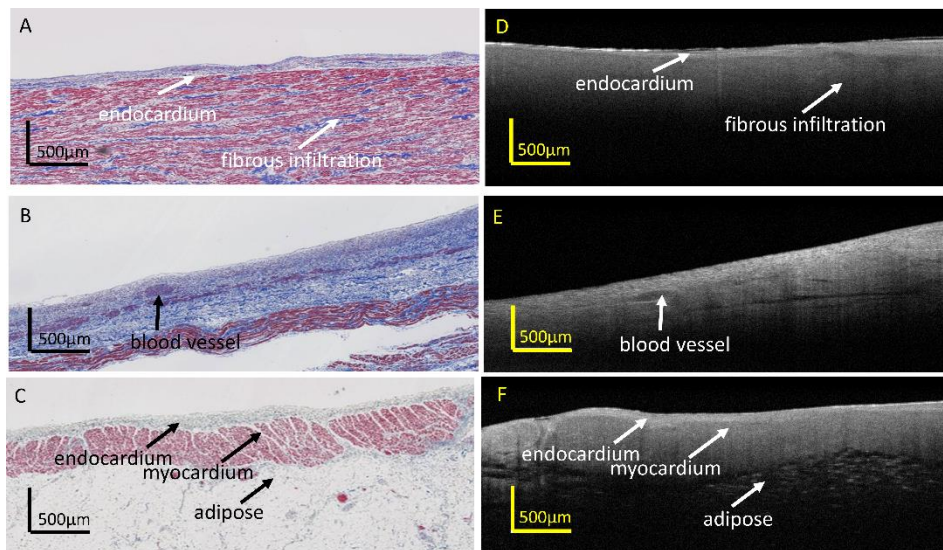
Figure 2.25. OCT images and corresponding histologic images of multiple substrates within the right atrium.

59

2.3.7.3 Fibrosis from All Chambers

Over the whole human heart, we visually observed different OCT image features when fibrosis was present in myocardial regions. Collagen within the myocardium could sometimes be seen in OCT images as higher intensity regions. For example, as shown in Figure 2.28A, E, collagen fibers running alongside the myofibers could be seen in OCT as bright, discrete strands. This is also demonstrated within the *en face* images of Figure 2.28I and J, with bright striations and patches corresponding to collagen regions. However, in other cases, fibrosis patterns were seen corresponding to decreased penetration depth, as shown in Figure 2.28(B-D, F-H). Fibrotic regions with low backscattering in comparison with the surrounding myocardial region could be seen for both diffuse and compact fibrotic regions, as seen in Figure 2.28(B-D, F-H). In some cases, corresponding OCT features to fibrosis as seen from histology were not visually apparent, such as seen in the above Figure 2.25D.
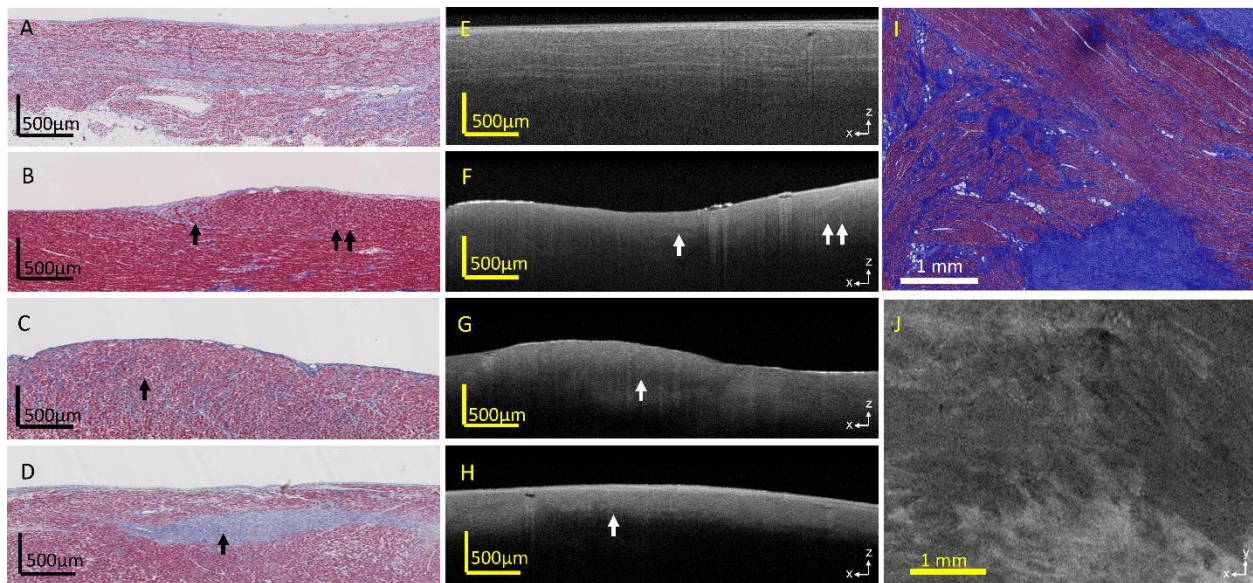
Figure 2.26. OCT images and the corresponding histologic images of fibrosis, showing various fibrosis patterns. A, E, Interstitial fibrosis, with collagen fibers running alongside myofibers; B, F, low level of diffuse fibrosis; C, G,

higher level of diffuse fibrosis; D, H, compact fibrosis region. Panels I-J show fibrosis as seen in the *en face* plane. (A, E, I, J) are from the atria and (B-D, F-H) are from the ventricle.

2.3.7.4 Statistical Analysis

We performed a statistical comparison of quantitative features extracted from the OCT images. We first compared the difference in OCT images from different chambers. Three representative features from optical properties (attenuation coefficient), texture (correlation), and pixel distribution (standard deviation) are presented in Figure 2.27. In general, we found the features had a strong correlation with the different chambers. For example, in attenuation coefficient, Figure 2.27A, features were significantly different except the pairs that were from the same chamber (left ventricle vs left ventricular septum, right ventricle vs right ventricular septum) and the same type of chamber (left atrium vs right atrium and left ventricle vs right ventricle). Other similarities, such as left ventricular septum vs left atrium and right ventricle vs right ventricular septum, were also identified by correlation and standard deviation, with these two chambers showing no significant difference in the multi-comparison test after ANOVA for these features. Notice that no single extracted feature could uniquely identify a chamber. There was no significant difference when comparing left ventricular septum vs right atrium in correlation and left atrium vs right ventricle in standard deviation.
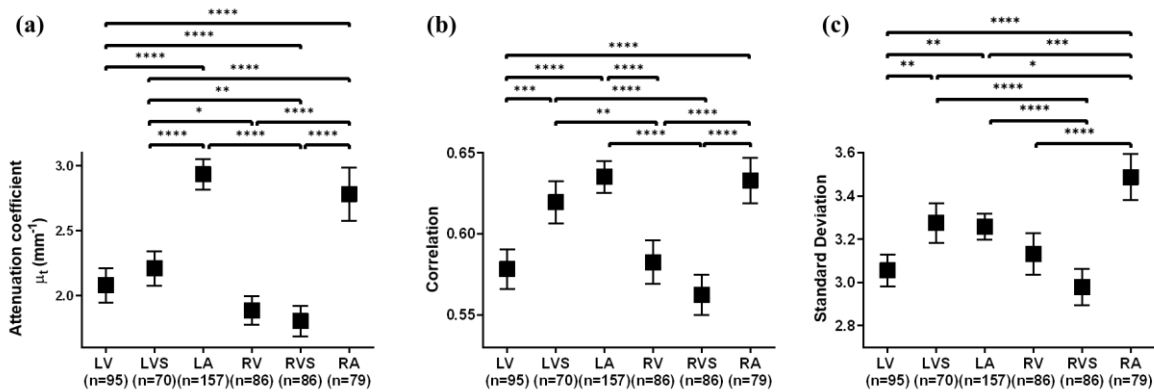
Figure 2.27. Statistical analysis of three representative features. A, attenuation coefficient, B, texture correlation, and
C, standard deviation, extracted from human cardiac OCT images. Comparisons were made within all chambers.

We also examined the difference in quantitative features among different tissue types. Figure 2.28 shows the statistics within atria (A-C) and ventricles (D-F). We found that adipose tissue was significantly different from all other tissue types in attenuation coefficient, correlation, and standard deviation in both the atria and ventricles. In ventricle, collagen and fibrotic myocardium were not significantly different in correlation, but were significantly different in attenuation coefficient and standard deviation (both p<0.001).
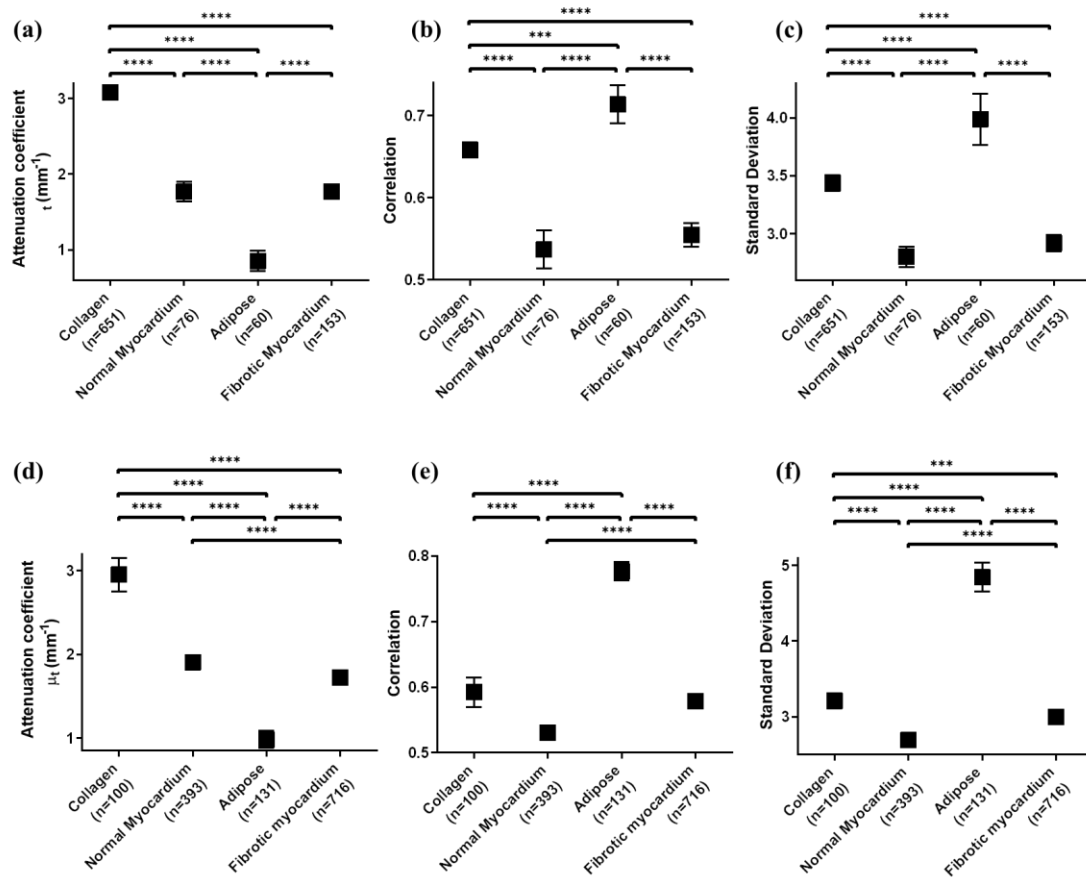
Figure 2.28. Statistical analysis of three representative features. A, D, attenuation coefficients, B, E, texture correlation, and C, F, standard deviation, extracted from human cardiac OCT images. Comparisons were made within all substrates in (A-C) atria and in (D-F) ventricle.

2.4 Discussion

This study is the first, to the authors' knowledge, to present comprehensive OCT imaging data of the whole human left atrium, which is also a subset of a whole human cardiac OCT imaging atlas. Given its high-resolution, OCT is capable of providing details of cardiac tissue structure that cannot be captured by current cardiac imaging modalities. The human cardiac OCT imaging atlas described within this study provides a basis for future OCT applications in investigating diseases of the human heart. Imaging criteria and distributions for different tissue types including myocardial sleeves, venous media, adipose tissue, endocardial and myointimal thickening, and fibrosis were provided for the human left atrium and pulmonary veins. OCT imaging of human left atrial tissue could provide additional information of the structural substrate of atrial fibrillation and potentially assist in guiding atrial fibrillation ablation procedures. Additionally, the cardiac OCT imaging atlas provides a reference for training future interpretation and processing of cardiac OCT imaging data. Rules for identifying tissue features from the OCT imaging data, developed from this study, are provided in the Appendix.

2.4.1 Applications to the Study of Atrial Fibrillation

There has been recent interest in the use of OCT to guide atrial fibrillation ablation therapy, specifically in imaging of ablation lesion formation [111-114, 116]. Using OCT-integrated catheters, regions of complex fiber orientation or fibrosis imaged by OCT could be associated to electrical conduction patterns, *in vivo*. Given the varying biophysical properties of different tissue compositions, endocardial thickness, fibrosis, adipose tissue, and myointimal thickening could

63

also be taken into consideration when choosing ablation targets. OCT imaging of the human left atrium could also be applied to basic science applications, such as correlating the tissue structure identified by OCT to certain disease states, given a larger sample size of hearts with atrial fibrillation. The tissue structure identified by OCT data could also be incorporated into tissue-specific, electrophysiological models to better understand the influence of tissue microstructure on atrial fibrillation dynamics, as will be described in the following chapters.

2.4.2 Influence of Imaging Depth

The main limitation of OCT is its imaging depth, which is determined by attenuation from optical scattering and absorption within the tissue [81]. Limitations are also posed by the OCT system sensitivity, which was 100 dB at 28 kHz with a roll-off of 5 dB at 2.26 mm for this imaging system. In the case of cardiac tissue, imaging of myocardial features of interest such as fiber orientation and fibrosis is limited by the thickness and density of overlying endocardium or venous media. In this study, it was found that myocardial features could be visualized under overlying endocardial thicknesses averaging 0.28 mm for OCT measurements and 0.31 mm for histology measurements, respectively.

OCT enables identification of endocardial thickness with resolution that cannot be achieved by other commonly used cardiac imaging modalities. In areas of thicker endocardium, however, the lower boundary of the endocardial layer in OCT disappears, limiting the ability to accurately measure endocardial thickness. Nonetheless, the knowledge of when the endocardium exceeds a certain thickness could still be useful for understanding the properties of tissue being ablated. For *ex vivo* applications, OCT imaging of the transmural atrial wall could be made possible through the use of optical clearing, imaging from both endocardial and epicardial surfaces, or thick sectioning of the tissue.

For investigation of detailed tissue architecture *in vivo*, however, initial applications of OCT may be most suitable for imaging the pulmonary veins and the interatrial septum. The maximum thickness of overlying connective tissue under which myocardial features could be seen were 0.43 mm for OCT and 0.47 mm for histology. The thickness of the endocardium and venous media at the venoatrial junction has been determined from ultrasound and histology to range from 0.05 to 1.7 mm at the venoatrial junction and decrease to a range of $0.0 - 0.3$ mm at 2 cm from the orifice towards the lung hilum [68]. Therefore, OCT is still applicable for a considerable range at the pulmonary veins. Furthermore, as demonstrated in this study, OCT imaging can penetrate the majority of the thickness of the thin region of the fossa ovalis.

2.4.3 Tissue Architecture of the Venoatrial Junction

The structure of the pulmonary vein myocardial sleeves have been identified through histological studies to be highly complex. Ho et al. described an intricate arrangement of both circular and longitudinal myofiber bundles, with gaps and fibrosis commonly observed within the myocardial sleeves [127]. The structure of the pulmonary veins are also variable among different hearts and between individual veins. Saito et al. in particular identified some pulmonary veins having a more regular and aligned arrangement of myofibers, while others had non-uniform, crossing patterns [130]. Due to its complicated and unique structure, high resolution imaging is needed to fully capture the pulmonary vein structural substrate. This study demonstrated that OCT is able to image similar myocardial sleeve features as seen from histology. In particular, OCT was able to visualize the orientation and density of myofibers and collagen fibers, which varied between veins. For instance, the parallel organization of myofibers and collagen fibers seen in Figure 2.14 can be contrasted to the more complex organization seen in Figure 2.17. Quantitative analysis showed that the myocardial and collagen fiber region seen in Figure 2.14 had higher average local range,

standard deviation, and entropy, but lower circular standard deviation of fiber angles than the region from Figure 2.17. This was likely because the myocardial and collagen fiber region seen in Figure 2.14 consisted of thinner, yet more organized fibers, in contrast to the larger and more disorganized collagen fibers seen in Figure 2.17. Such analysis shows promise of quantitative metrics of fiber and fibrosis complexity from OCT images in the future. Finally, fiber orientation running in crossing directions were observed over different depths, as demonstrated in Figure 2.11.

2.4.4 Tissue Architecture at the Interatrial Septum

The leading cause of aborted transseptal puncture procedures has been cited to be difficulty in identifying the location of the fossa ovalis. [141] As it was shown within this study that thin regions of the fossa ovali can be identified and imaged transmurally with OCT, it is possible that OCT imaging could be used as an adjunctive tool to assist in the identification of the fossa ovalis for transspetal puncture. Furthermore, the septum has been reported as one of the common locations for non-pulmonary foci for atrial fibrillation. [38] As myofiber orientation as well as significant distributions of adipose tissue could frequently be identified at the interatrial septum with OCT, it is possible that OCT could provide further information useful for understanding structural influences on arrhythmia dynamics. Increased adipose at the interatrial septum is associated with atrial fibrillation. [65, 142] While catheter-based, *in vivo* OCT imaging would only able to determine distributions of adipose tissue near the surface, further study could potentially delineate if the total volume of OCT-imaged adipose correlates to the overall adiposity of the interatrial septum.

2.4.5 Limitations and Future Work

With regards to *in vivo* applications, a limitation is that this study was carried out *ex vivo*. *In vivo* imaging would pose additional challenges due to heart and catheter motion, as well as the need for

real-time mapping and stitching to visualize large fields of views. Thus, future *in vivo* studies would be required to determine if the same features described in this study can be visualized during ablation. Prior studies in swine, however, have demonstrated the capability of OCT-integrated catheters to image the atrial endocardium and myocardium *in vivo* [113, 114].

Additionally, while the majority of the left atrial tissue was imaged for mapping, due to the manual nature of imaging and limitations of the imaging setup, some regions of tissue were not imaged at the edges of the tissue. Furthermore, the size and morphology of human hearts differ, including the left atria. Therefore, more precise mapping to atrial geometry would require personalized meshes of the left atria, such as could be obtained from MRI or CT.

During image pre-processing, it is possible that the contact glass surface of the sample z-Spacer, when completely adjacent with the endocardial surface, could not be distinguished from the endocardium, potentially affecting endocardial measurements in some cases. As an estimate of the potential error, the thickness of the z-Spacer surface seen in OCT was measured from one B-scan and found to be about 0.04 mm.

In this study, endocardial thickness measurements were sampled from three different points within the regions of interest to characterize the overall trend. Representative quantitative myofiber texture and angle measurements were also taken from selected ROIs. In the future, automated methods [95, 118, 143] can be more comprehensively applied to quantitatively evaluate endocardial thickness and other tissue features, such as myointimal thickening and fiber orientation, over the entire imaged region. Further studies would also be needed to more quantitatively assess the accuracy of OCT in identifying tissue features when compared to histology.

67

For the whole human heart cardiac atlas, statistical analysis was carried out on small regions of interest within each B-scan. More discriminating features could be possible by carrying out statistical analysis on fully segmented OCT image volumes. The data from the human cardiac OCT imaging atlas can also be analyzed further to identify correlations between imaged tissue structures and disease. Finally, only a few donors in the left atrial imaging study had a history of atrial fibrillation, and additional OCT imaging in hearts from donors with atrial fibrillation would be necessary to determine further applicability to atrial fibrillation ablation.

2.5 Conclusion

This study demonstrated that OCT can provide detailed visualization of tissue architecture in the human left atrium. Structural features such as myocardial sleeves, fiber orientation, fibrosis, adipose tissue, endocardial thickness, and myointimal thickening were identified from the OCT images and mapped to left atrial geometry. Imaging of detailed tissue architecture could assist in the guidance of ablation procedures and improve the understanding of the structural substrate of atrial fibrillation. More generally, OCT imaging of cardiac tissue over the whole human heart could provide useful information of pathological structures relevant to cardiovascular disease.

Chapter 3 Workflow for the Development of OCT-Informed Cardiac Models

3.1 Introduction

Optical mapping is an experimental technique that uses voltage-sensitive dyes to track changes in transmembrane potential in cardiac tissue using fluorescence. Optical mapping can be carried out on cultured myocyte monolayers, [144] sections of cardiac tissue, [145] or on whole hearts through panoramic mapping techniques. [146] During optical mapping, cardiac tissues are stained with voltage-sensitive dyes which bind to the cardiac cell membranes. The magnitude of fluorescence emitted by the dye at a specific emission wavelength changes with the depolarization and repolarization of the cardiac cell, thus providing a signal that is proportional to changes in transmembrane potential. Therefore, cardiac action potentials can be tracked by collecting emitted fluorescent light at the target emission wavelength through the use of optical filters. The most popular dyes are the styryl dyes, such as Di-4-ANEPPS and Rh-421 [147-149]. An optical mapping setup requires a light source, such as tungsten-halogen bulbs, laser light, or light-emitting diodes; a detector, such as photodiode arrays, charge coupled device cameras, and complementary metal-oxide semiconductor cameras; and optical filters to reduce background light and obtain the desired excitation and emission wavelengths. [148]

While optical mapping enables tracking of the spatiotemporal dynamics of cardiac electrophysiology, there have been differences observed between electrode recordings and optical mapping recordings of action potentials. For example, the optical action potential typically has an elongated upstroke compared to the electrical action potential, with the optical action potential having been recorded to be about up to five times longer than its electrical counterpart. [150] Other

discrepancies have been observed in the optical mapping signals, such as elevated resting potentials during arrhythmia, [151] dual-humped action potentials, [152] and decreased magnitude of virtual electrode polarization induced by defibrillation-strength shocks. [75] These phenomena are related to the scattering and integration of the optical mapping signal over depth and have prompted further investigation into how optical mapping signals manifest. For this reason, computational models that simulate optical mapping signal synthesis have been developed. Such models have enabled further insights in how the morphology of optical mapping signals relate to subsurface electrophysiological distributions. For example, Hyatt et al. discovered through computer simulation, and later through verification with optical mapping experiments, that the shape of the optical action potential upstroke is related to the angle of propagation of the subsurface electrophysiological wave relative to the tissue surface. [71, 153] Bishop et al. identified, through simulations of arrhythmia and optical mapping on an anatomically realistic rabbit ventricular model, that the location of phase singularities were shifted in optical mapping signals compared to the transmembrane potential distributions. [74] Findings such as these enable improved interpretation of optical mapping signals, and open up possibilities of extracting valuable intramural information of electrical patterns from optical mapping signals.

Optical mapping models are developed by combining electrophysiological simulations with optical simulations of excitation and fluorescent emission. Optical simulations have been carried out using photon diffusion theory. [71] However, Monte Carlo photon scattering simulations have been shown to provide more realistic results, [154] and are more useful for models incorporating complex, heterogeneous tissue structure. [76] The majority of prior optical mapping models have been developed with simplistic shapes and homogeneous tissue regions. However, realistic tissue models are critical for understanding electrophysiological dynamics. In

this chapter, we develop a modeling workflow for creating tissue-specific optical mapping models derived from OCT imaging. The general workflow for simulating optical mapping in OCT-characterized atrial models is described in Figure 3.1. Structural features, such as fiber orientation, location of ablation lesions, and distribution of different tissue types, were extracted from the OCT volumetric data of the tissues and used to develop the tissue-specific models. After construction of the models, electrophysiology and excitation photon scattering were simulated, and the resulting transmembrane potential and excitation photon density data were used to generate the fluorescent sources that produce the optical mapping signal. In the final step, fluorescent light propagation was simulated to produce the optical mapping signal in the atrial tissue models.
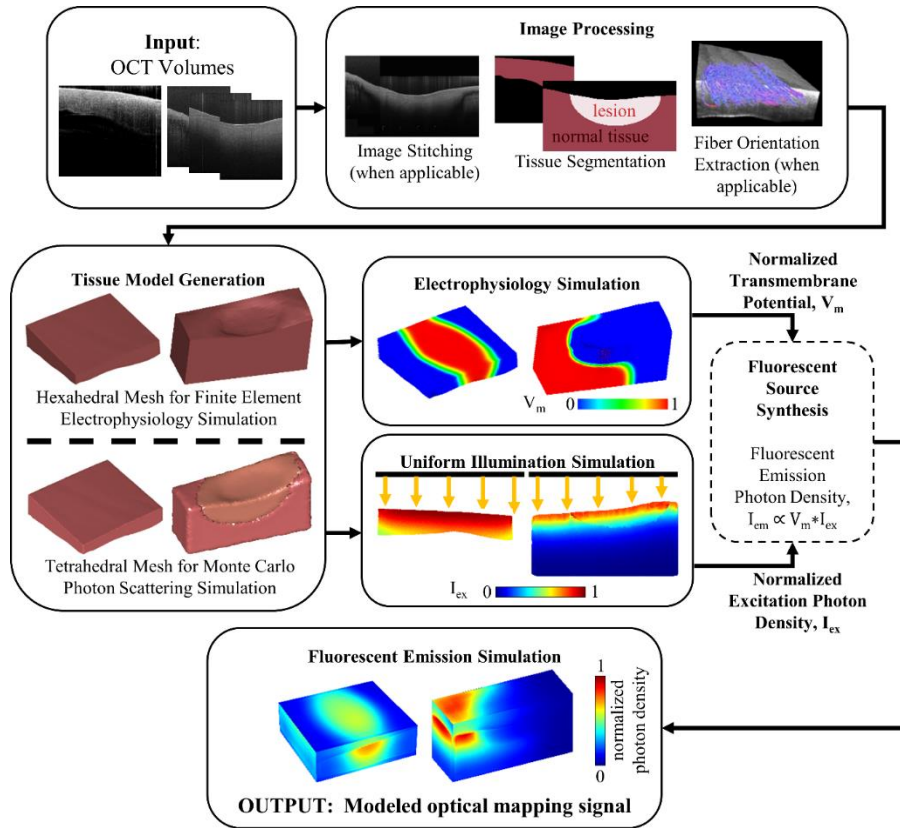
Figure 3.1 Flow diagram for optical mapping modeling of atrial tissue as derived from OCT images. V_m is normalized transmembrane potential, I_{ex} is normalized excitation photon density, and I_{em} is fluorescent emission photon density.

3.2 Image Processing

3.2.1 Tissue Geometry and Tissue Composition Extraction

Tissue geometry and composition must first be extracted from the OCT images to be incorporated into the mesh geometry and model parameters. This includes extraction of the tissue surfaces and features including myofiber orientation and distribution of different tissue types. Extraction of tissue geometry is carried out through the detection of the tissue surfaces. The identification of tissue surfaces from OCT images can typically be accomplished using gradient and thresholding techniques due to the high contrast between the background and surface of the tissue in OCT. The specific parameter and processing steps of tissue surface detection, however, may vary between different OCT image volumes based on the imaging system used and the presence of artifacts. More detailed steps will be provided for each specific dataset in Chapter 4. Myofiber orientation can be extracted using a previously described automated method. [95] The lateral boundary of ablation lesions can be estimated using previously described image processing techniques [115] or through manual segmentation. The appearance of the birefringence artifact, which disappears in regions of ablated tissue, [109, 110, 115] or the decreased contrast between the endocardium and myocardium, as well as the disappearance of collagen fibers within the lesion, can be used as features to identify the lesion contours in the lateral dimensions. Currently, there is no method to estimate lesion depth from OCT. Therefore, lesion depth must be estimated from triphenyltetrazolium chloride (TTC) staining and histology. Regions of myocardium, endocardium, and adipose tissue can be segmented manually based on the known image features of those tissue types.

3.2.2 Lesion Contour Estimation

For modeling, the shape of the lesion was estimated from the lateral boundaries as derived from OCT imaging and the maximum depth of the lesion as identified from TTC and histology.

Elliptical arcs were used to estimate the contour of the lesion in depth, based on the ellipsoidal shape of lesions as reported in literature [155], as well as from individualized observations of each lesion sample. For non-transmural lesions, the maximum depth of the lesion was assumed to be at the center of the lesion. For each B-scan, points on the outer boundaries of the lesion in the x-dimension were identified, as well as a point located midway between the two outer boundary points and at the desired depth of the lesion for the current B-scan. From these three points, two quarter-elliptical arcs were used to estimate the lesion contour in depth, with the ends of one arc being the leftmost boundary point and the maximum depth point, and the ends of the second arc being the rightmost boundary point and the maximum depth point. The maximum depth for each B-scan was similarly constructed by two elliptical quarter-arcs, except with the elliptical arcs joined to the boundary points in the center of the lesion in the y-dimension. This is illustrated in Figure 3.2.
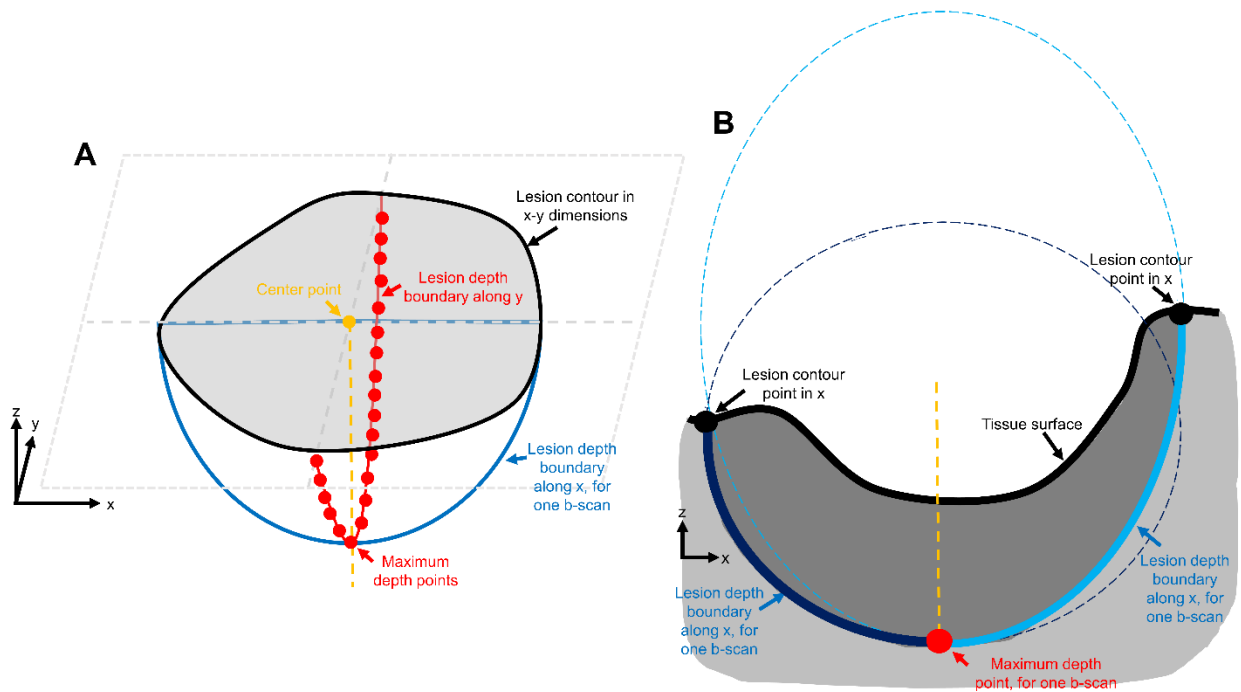
Figure 3.2. Lesion depth boundary estimation for non-transmural lesions. A, Overall depth boundary estimation. B, Depth boundary estimation for a single B-scan.

For transmural lesions, the lateral boundary of the lesion at the upper surface of the tissue was assumed to be the same as on the bottom surface of the tissue. Therefore, for each B-scan, the lesion boundary in depth was estimated using two half-elliptical arcs, with the end points of the arcs located on the upper and lower surfaces of the tissue. The increase in the lateral boundary seen half-way through the depth of the lesion was estimated from TTC and histology and was the minor axis of the elliptical arc. This is illustrated in Figure 3.3.
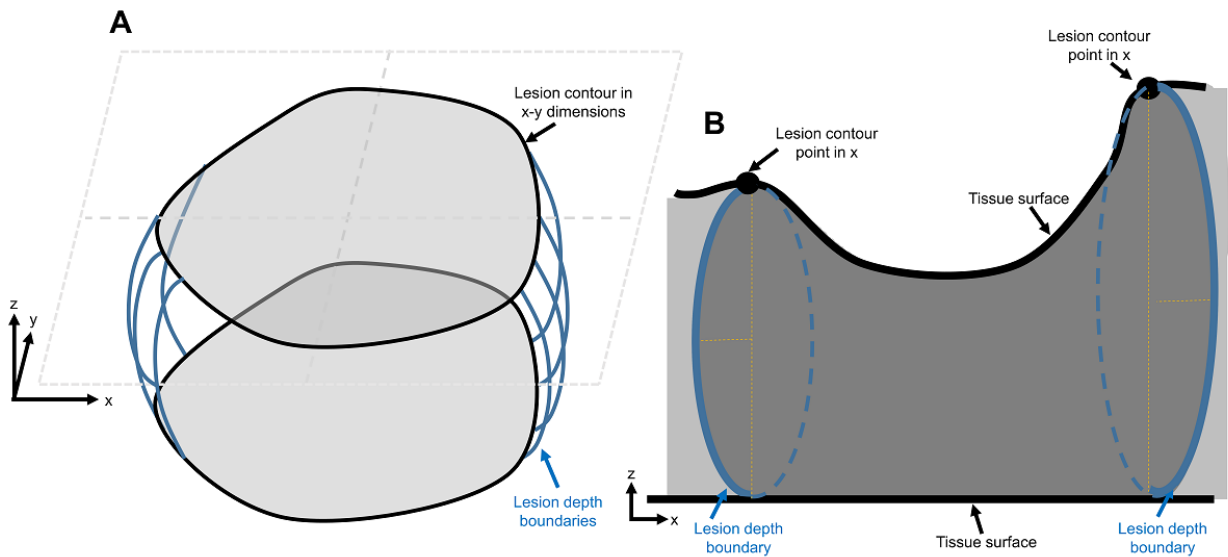
Figure 3.3 Lesion depth boundary estimation for transmural lesions. A, Overall depth boundary estimation. B, Depth boundary estimation for a single B-scan.

3.3 Mesh Generation

Once the tissue geometry is extracted from the OCT image volume, a mesh must be created with the same geometry. Two different simulation schemes were used for electrophysiological

simulation and photon scattering simulation. For the electrophysiological simulation, Continuity 6 [156], a multi-scale modeling finite element package distributed by the National Biomedical Computation Resource, was used. Continuity 6 uses a hexahedral mesh for simulation. For photon scattering simulation, the Monte-Carlo optical simulator TIM-OS [157] was used. TIM-OS uses a tetrahedral mesh for simulation. Therefore, both a hexahedral mesh and a corresponding tetrahedral mesh were required for the modeling workflow.

3.3.1 Hexahedral Mesh

The nodes of the hexahedral mesh corresponding to the tissue surfaces were generated by sampling the segmented tissue surface data with the desired node spacing. The desired spacing of the nodes was dictated by the desired conduction velocity and convergence parameters, as will be discussed in Section 3.4. After the mesh surfaces of the upper and lower surfaces of the tissue were generated, the mesh was divided in the axial direction by refining within Continuity 6. Discretization of the mesh in the axial direction was non-uniform because of variations in thickness of the tissue. Therefore, the mesh was refined in the axial dimension such that the maximum distance between two adjacent nodes in the axial direction was equal to or less than the element edge length used for the lateral dimensions. Myofiber orientation could be fitted to the mesh using the built-in Continuity 6 fitting module or through 3D interpolation, with the angle data being extracted as a set of points, each with an x-y-z coordinate within the model spatial domain and the corresponding angle value. Assignment of different tissue types could be accomplished in a similar fashion. This basic hexahedral mesh generation procedure is depicted in Figure 3.4.

Tissue segmentation   Unrefined mesh   Axially Refined mesh   Distribution of fitting data points
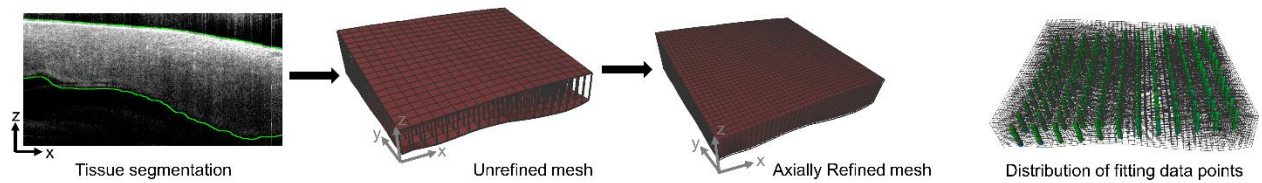
Figure 3.4 Hexahedral mesh generation procedure.

3.3.2 Tetrahedral Mesh

Tetrahedral meshes were generated with the open-source 3D surface and volumetric generator, iso2mesh [158]. The edge length of the tetrahedron was set to be on the order of the step-size of a photon packet, which is determined by the optical absorption and scattering parameters of the medium. [159] Each tetrahedral mesh of cardiac tissue was generated with a surrounding rectangular region of perfusate, as shown in Figure 3.5. This was accomplished by generating a surface mesh corresponding to the tissue geometry as well as a surrounding rectangular surface mesh, merging the two surface meshes, and converting to a volumetric mesh. The optical parameters of the perfusate were set such that the light was not absorbed within the perfusate region and was only scattered forward in a straight line, with the anisotropy coefficient $g = 1$, as has been done in previous optical mapping models using TIM-OS. [76] The refractive index of the perfusate region was set to 1.3. The models also included a region of air surrounding the perfusate that had a refractive index of 1.
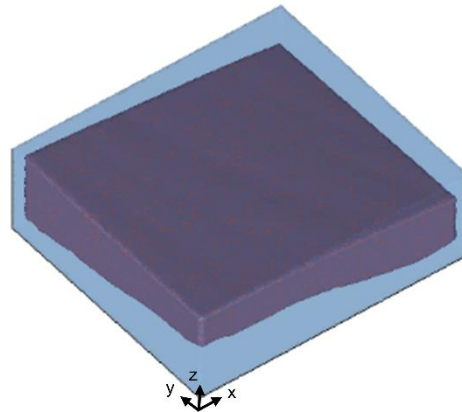
Figure 3.5 Tetrahedral mesh of cardiac tissue with surrounding perfusate.

3.4 Electrophysiological Modeling

The Fenton Karma ionic model with atrial parameters was used with the monodomain model for all electrophysiology simulations. [160, 161] The necessary mesh discretization for a desired conduction velocity was determined by first testing electrophysiological simulations on a 3D rectangular strip. The 3D rectangular strip was swept over different element step sizes while maintaining the same aspect ratio, 100 by 8 by 4 elements. For a given diffusivity, discretizations of the mesh ranging from about 0.05 to 2 mm element step sizes were tested with a planar wave traveling from one end of the strip to the other. The resulting conduction velocity was computed for each element step size by measuring the activation times along the length of the strip, and the maximum element step size with which the conduction velocity converged, or smaller, could be used for simulations. Because diffusivity is proportional to the square of the conduction velocity, the diffusivity for a new desired conduction velocity could be identified based on one known diffusivity and corresponding converged conduction velocity. For different tissue types, the diffusivity of nodes within different tissue regions could be adjusted accordingly. If necessary, further tuning was carried out for each individual model by additional adjustments of element and time step sizes.

3.5 Optical Mapping Modeling

The transmembrane potential data from the electrophysiology simulations are coupled with simulated excitation photon density data and then used as input to a fluorescent light scattering simulation to model the optical mapping signals. The Monte-Carlo optical simulator TIM-OS [157] was used to compute light scattering in tetrahedral meshes corresponding to the tissue geometry.

3.5.1 Simulation of Tissue Excitation

During optical mapping, the tissue is first illuminated to excite the fluorescent dye. To simulate uniform illumination, photons were emitted from the upper surface of the perfusate, which was a flat layer positioned over the tissue mesh, with a uniform photon density. The number of photons emitted per triangle element was determined by a given excitation photon density, or number of photons emitted per unit area for illumination, scaled by the area of the triangle. To determine the excitation photon density necessary for a converged simulation, the maximum allowable number of photons emitted per element was swept from about 10 to 100,000 photons. The simulation was run 5 times for each maximum emitted photon value. The standard deviation of the resulting volumetric fluence in the tissue mesh was computed for each parameter value, and convergence was determined when the overall standard deviation was about equal to or less than 0.05. The resulting photon density within the tetrahedral elements represented the illumination intensity stored within the tissue.

3.5.2 Simulation of Fluorescence Emission

Following illumination, the fluorescence of the voltage-sensitive dye must be simulated to synthesize the optical mapping signal. The intensity of fluorescent emission from a specific location within the tissue is proportional to the magnitude of excitation light and transmembrane potential at that location. To simulate fluorescent emissions, photons were emitted in an isotropic fashion from each tetrahedron in the mesh. The number of photons emitted per tetrahedral element was calculated by scaling a maximum fluorescence photon density, or maximum number of photons emitted per unit volume for fluorescent emission, by the tetrahedron's normalized excitation photon density, normalized transmembrane potential, and the tetrahedron volume. To obtain the normalized excitation photon density, the volumetric fluence stored within each tetrahedron from the illumination simulation was subsequently scaled from 0 to 1 by normalizing

78

with respect to the maximum volumetric fluence within the tissue region of the mesh. To obtain the normalized transmembrane potential, the voltage at that location was also scaled from 0 to 1, normalized with respect to the maximum action potential voltage. The voltage assigned to a tetrahedron was determined by interpolation of the 3D distribution of voltage as calculated on the hexahedral mesh to the centroids of the elements of the tetrahedral mesh. For each point in time in the electrophysiological propagation simulation, a separate field of fluorescent sources needed to be generated for another Monte Carlo fluorescent photon scattering simulation due to the changing voltage distribution.

3.6 Conclusion

We have developed a workflow for generating OCT-derived, tissue specific models for electrophysiological and optical mapping simulation. The workflow can be applied to OCT imaging data of any cardiac tissue, including tissues with heterogeneous composition. With the provided methodology, OCT-informed optical mapping models can be utilized to investigate the relationship between complex tissue structure as imaged by OCT and electrophysiological function, as well as enable more direct comparisons to optical mapping experimental data through optical mapping simulations. With the high resolution imaging of OCT, OCT-informed modeling provides the potential to investigate the functional influence of tissue microstructure in more detail compared to current image-based models.

Chapter 4 OCT-Informed Models of Atrial Tissue with Electrophysiology and Optical Mapping Simulation

4.1 Introduction

To investigate structure-function dynamics with OCT, structural information from OCT has been used in combination with optical mapping. In a study by Hucker et al., tissue specific structure identified by OCT imaging was correlated to multilayer electrical conduction and the location of reentry cores during arrhythmia. Different fiber orientation patterns seen at different depths of the tissue, as imaged by OCT, could be correlated to the electrical activation patterns observed from optical mapping. Additionally, the location of optically mapped reentry cores were associated with tissue regions where shifts in dominant fiber angle distributions were identified at different tissue depths by volumetric OCT imaging. [107] Thus, structural information from OCT has been demonstrated to assist in the interpretation of optical mapping signals. The correspondence between optical mapping measurements and OCT structural information motivates the development of OCT-informed computational models for optical mapping simulation, which may enable more precise correlations of experimental 2D optical mapping data to 3D imaging data. As interpretation of optical mapping signals may be complicated by interactions with heterogeneous tissue structure, [72, 76] tissue-specific, computational modeling of optical mapping has been developed to enable a deeper understanding of the influence of structural heterogeneities on the formation of optical mapping signals.

Prior modeling studies have investigated the effects of ventricular tissue thickness, fiber orientation, and tissue geometry on optical mapping signals. The influence of varying tissue

thickness on optical signal morphology, in slab models ranging from 2.5 to 10 mm thickness, as well as in models simulating trabeculation of the ventricular endocardium, have been previously investigated. [153, 154, 162] The effect of ventricular fiber orientation patterns has been analyzed in slab models [71, 145, 154] and cylindrical models. [153] Whole rabbit ventricular models, with ventricular anatomy and fiber orientation informed by serial sectioning, have been used to assess the effect of tissue structure on optical signal morphology during pacing, arrhythmia, and defibrillation. [72, 74, 75] Additionally, a model of a rabbit ventricular wedge, using high-resolution MRI to inform tissue geometry and histologically-informed fiber orientation, has been developed to investigate the effect of tissue structure, specifically vein cavities, on the optical signal [76]. To the authors' knowledge, there are currently no optical mapping models focusing on atrial structure or utilizing the high-resolution three-dimensional structural information that can be offered by OCT.

In this chapter we present, to our knowledge, the first use of high-resolution OCT volumetric data to develop tissue-specific atrial models. We developed atrial models including tissue-specific fiber orientation extracted from OCT imaging, ablation lesions which utilized OCT to determine the lesion boundaries within the tissue geometry, and heterogeneous tissue types including adipose and endocardium. Four different swine atrial samples and one human left atrial sample were used to demonstrate the incorporation of OCT-derived structural features into optical mapping models.

4.2 Methods

4.2.1 Tissue Acquisition and Dissection Protocol

Swine and human atrial tissues were acquired for modeling. Fresh swine hearts were obtained from a local butcher. Diseased human hearts were acquired under an approved protocol from the

National Disease Research Interchange. Recovery of human hearts was completed within 24 hours after death, and the hearts were delivered to the lab while submerged in an ice-cold phosphate-buffered saline bath. From the hearts, tissue regions up to about 8.5 mm in lateral dimension were dissected for imaging. In this study, five different models were developed from the tissue samples: (1) a model of swine left atrial tissue with tissue-specific fiber orientation and tissue geometry as extracted from OCT, (2) a model of swine left atrial tissue from a larger stitched region, including an area of sharp myofiber orientation change, (3) a model of swine right atrial tissue with a non-transmural lesion region, (4) a model of swine right atrial tissue with a transmural lesion region, and (5) a preliminary model of human left atrial tissue incorporating endocardial, adipose, and myocardial tissues. For simplicity, these models will be referred to as the (1) left atrium fiber-1 model, (2) left atrium fiber-2 model, (3) the non-transmural lesion model, (4) the transmural lesion model, and (5) human left atrial model. The left atrium fiber-1 and left atrium fiber-2 models were developed to investigate the influence of OCT-derived, tissue-specific fiber orientation on the transmural electrophysiological propagation and corresponding optical signal. The lesion models were developed to investigate the behavior of the optical mapping signal within lesions areas. The human left atrial model was developed to investigate the influence of different tissue types incorporated into the model.

4.2.2 Imaging Protocol

Volumetric OCT image sets were acquired from the tissue samples, *ex vivo*. The tissue samples for the left atrium fiber-1, left atrium fiber-2, and human left atrial models were imaged using the commercial spectral domain OCT system, TELESTO (Thorlabs GmbH, Dachau, Germany). The TELESTO OCT system has a 15 μm and 6.5 μm lateral and axial resolution, respectively, and a 2.51 mm imaging depth in air. The left atrium fiber-1 dataset was acquired from the epicardial

side, while the left atrium fiber-2 and human left atrial dataset was acquired from the endocardial side. For the lesion models, two right atrial tissues were first ablated on the endocardial surfaces using the commercial RFA system, Stockert 70 (Biosense Webster, Diamond Bar, CA). The image sets for the RF ablated tissues were then acquired from the endocardial side using a custom-built ultrahigh resolution OCT system, with 5.52 μm and 2.72 μm lateral and axial resolution, respectively, and 1.78 mm imaging depth in air [119]. This OCT system was used for imaging the ablated tissues because the TELESTO system did not capture the birefringence artifact that could be used to detect the ablation lesion in the OCT images.

Multiple overlapping image volumes were acquired to cover larger regions of tissue for the left atrium fiber-2 and lesion models. When necessary, the overlapping image volumes were histogram matched to equalize the contrast between separate volumes and stitched together manually. Consecutive stitched B-scans were averaged by 3 to improve the visualization of tissue features. When necessary, stitched image volumes were downsampled by 3 to reduce the computational load during image processing. Trichrome histology and triphenyltetrazolium chloride (TTC) staining were carried out on the ablated tissue samples to reveal lesion characteristics beyond the sampling depth of the OCT system. Figure 4.1 shows the OCT image volumes used to inform the left atrium fiber-1, non-transmural, transmural lesion, and human left atrial models, displaying the tissue geometry of the data. For the left atrium fiber-2 data, the entire thickness of the tissue was not within the OCT system's imaging depth and fiber orientation could only be observed within a limited region of myocardium underneath the endocardial surface. Therefore, the tissue geometry was not included in the left atrium fiber-2 model and only an electrophysiological simulation was carried out on the left atrium fiber-2 model.
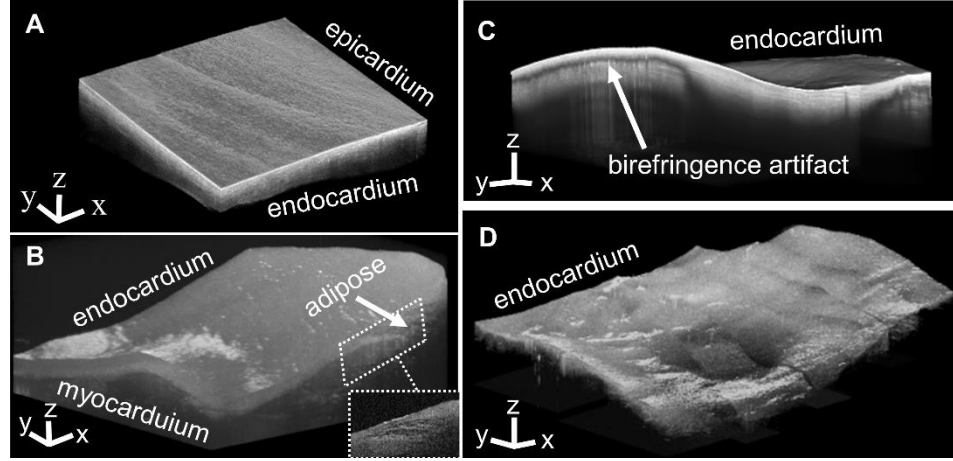
Figure 4.1. OCT imaging of atrial tissues. A, Swine left atrial tissue OCT image volume for the left atrium fiber-1 model. B, Human left atrial OCT image volume for the human left atrial model. C, Swine right atrial tissue OCT image volume with a non-transmural lesion for the non-transmural lesion model. D, Swine right atrial tissue OCT image volume with a transmural lesion for the transmural lesion model.

4.2.3 Image Processing

Image processing to extract the fiber orientation, tissue geometry, lesion location, and different tissue types from the OCT volumetric data was implemented in MATLAB (The MathWorks, Natick, MA) or carried out manually using IMOD [138].

4.2.3.1 Fiber Orientation Extraction

Full details of the fiber orientation extraction algorithm have been described previously [95], but will be briefly summarized here. Fiber orientation in three dimensions was extracted from fresh tissue samples, without optical clearing. We used an automated algorithm that first detected the fiber angles in the *en face* plane and then projected them to 3D based on the detected tissue surface orientation. Identification of the fiber angles in the *en face* images was carried out by determining the dominant gradient within small sub-regions spanning each *en face* image. Afterwards, the tissue surface was detected from the OCT B-scans, and for each voxel, the *en face* fiber angle was

84

projected onto a plane parallel to the tissue surface. The fiber orientation data was median filtered by a 3 x 3 kernel to smooth the angles prior to fitting to the models.

4.2.3.2 Extraction of Tissue Geometry

The surfaces of the cardiac tissues were detected semi-automatically from the OCT B-scans to extract the tissue geometry. Surface detection consisted of image smoothing to reduce the effect of speckle noise, and then detection of the maximum gradient magnitude in the axial direction. Filtering parameters were tuned manually between datasets or different tissue regions due to varying image quality caused by saturation artifacts, distance of the varying tissue topology from the imaging surface, use of different imaging systems, or image stitching artifacts. The details of the tissue geometry detection are described for each dataset below.

For the left atrium fiber-1 dataset, to detect the upper, epicardial surface, a 10 x 10 median filter was applied to smooth speckle noise, before the maximum magnitude of the gradient in the axial direction was detected. To detect the lower, endocardial surface, the upper tissue surface was first cropped from the image volume. A 20 x 20 median filter and morphological opening with a disk-shaped structuring element of radius 15 were applied to smooth noise. The image was then thresholded, and morphological closing on the binary image was applied with a disk-shaped structuring element of radius 15 to close gaps in the detected surface. The minimum magnitude of the gradient in the axial dimension was detected. For the left atrium fiber-2 data set, the dataset was first downsampled by 3. To smooth speckle noise, a 10 x 10 median filter was applied. The maximum of the gradient magnitude in the axial direction was detected. A 15 x 15 median filter was applied to the detected surface to smooth remaining errors.

For the non-transmural lesion dataset, a 20 x 20 median filter was applied to smooth speckle noise, and morphological opening with a 30 x 50 rectangular structuring element was applied to minimize vertical streak-like saturation artifacts. The gradient magnitude was computed. The background signal of the OCT image and blank regions induced by stitching created areas of high gradient magnitude that interfered with the detection of the tissue surface. These areas were removed after calculation of the gradient magnitude by the following steps. First, a 10 x 10 average filter to the original image was applied and the image was thresholded. A dilation of the resulting binary image, with a disk-shaped structuring element of radius 20, was applied to create a binary mask that was zero over the erroneous boundaries. The gradient magnitude matrix was multiplied by this binary mask. Afterwards, the gradient magnitude was thresholded and detected. The detected surface from each B-scan was median filtered with a kernel size of 15 to smooth the resulting surface. For the transmural lesion dataset, the dataset was downsampled by 3. A 5 x 5 median filter was applied. The maximum axial gradient magnitude was detected after removal of erroneous areas of high gradient magnitude in the axial direction caused by stitching, with an equivalent procedure as described above for the non-transmural lesion dataset. The detected surface was median filtered with a 15 x 15 kernel size. For the ablated tissue data, the epicardial surface was outside of the OCT system's imaging depth. Therefore, a flat bottom surface for the ablated tissue data was assumed. The maximum thicknesses of the ablated tissues were approximated from histology or white light images of the gross specimen cross-section.

For the human left atrial dataset, the tissue surface and endocardial, myocardial and adipose tissue regions were segmented manually in IMOD [138] from the B-scans. A binary mask was generated for each different tissue type. The lower boundary of the endocardium was determined based on the high contrast between the high intensity endocardium and underlying, low intensity

myocardium. The presence of adipose was determined by a brightly spotted or "honeycomb" pattern, typically with a background of decreased intensity than surrounding myocardium. A representative segmented B-scan is given in Figure 4.2. Because the epicardial surface could not be seen in the volume given the imaging depth of the OCT system, a tissue thickness of 1.5 mm was estimated from histology.
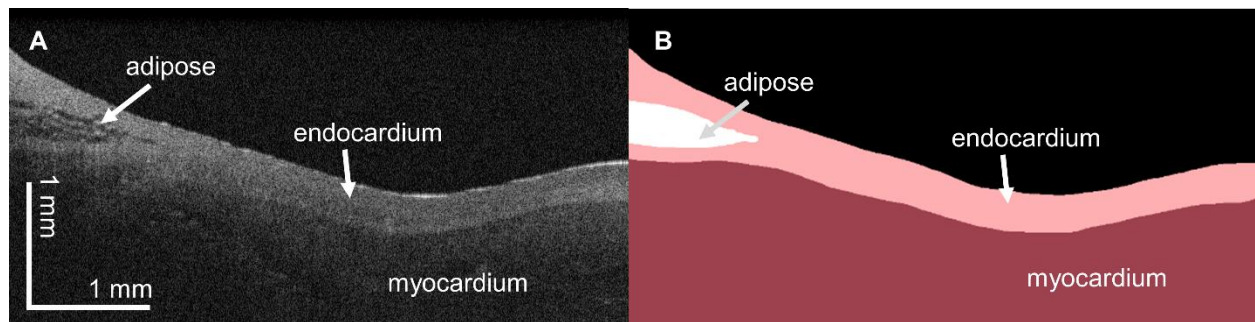
Figure 4.2. Tissue segmentation. A, OCT B-scan from the human left atrial dataset. B, Segmented B-scan corresponding to A.

The resulting, combined adipose and endocardial thickness for the imaged sample is given in Figure 4.3, revealing the thickest regions of adipose and endocardium in the lower right corner.
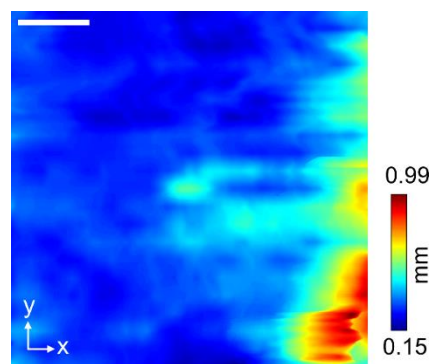
Figure 4.3. Extracted adipose and collagen thickness map in the human left atrium OCT image volume. Scale bar indicates 1 mm.

87

4.2.3.3 Extraction of Ablation Lesion Region

The boundaries of the ablation lesions were identified by the appearance of the birefringence artifact for the non-transmural lesion, and by changes in the tissue features as visualized by OCT for the transmural lesion. The appearance of the non-transmural lesion and the birefringence artifact seen in OCT is shown in Figure 4.4. A method based on that described in [115] was used to detect the lesion boundaries for the non-transmural lesion. To detect the birefringence artifact, a region of interest up to 50 pixels below the tissue surface was first defined. Within this region, the image was then filtered by a 50 x 50 Laplacian of Gaussian (LoG) filter with a standard deviation of 1. The maximum was taken from each A-line within the LoG filtered image and the 1D vector of maximum gradient values was median filtered by 20 to smooth the extracted trend. Finally, the maximum gradient values were thresholded to separate regions based on whether the birefringence artifact was present or not. This enabled the detection of the boundary of the lesion within each B-scan based on the birefringence artifact. In the OCT image volume of the transmural lesion, the birefringence artifact could not be seen in this particular dataset. In this case, the decreased contrast between the endocardium and myocardium as well as the disappearance of collagen fibers within the lesion were used as markers for the boundary of the lesion, as shown in Figure 4.4C and D. The lesion boundary was segmented manually through visual inspection.
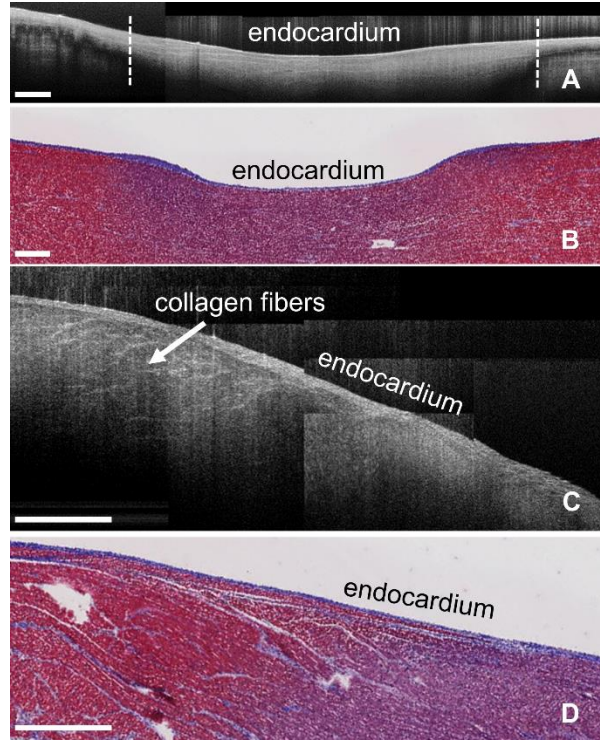
Figure 4.4 Visualization of ablation lesions in OCT. A, Representative stitched B-scan from ablated right atrial tissue with birefringence artifact. Dotted white lines indicate the boundaries of the lesion as detected by the fall-off of the birefringence artifact. B, Corresponding Trichrome histology of ablated right atrial tissue. Purple indicates necrotic tissue while red indicates healthy tissue. C, Representative stitched B-scan from ablated right atrial tissue, where the ablation lesion can be observed by the loss of collagen fiber structure and decreased contrast between the myocardial and endocardial layers. D, Corresponding Trichrome histology. The scale bars indicate 0.5 mm.

4.2.4 Electrophysiology Simulation

4.2.4.1 Mesh Generation for Electrophysiology Simulation

For the left atrium fiber-1, lesion, and human left atrial models, three-dimensional hexahedral finite element models corresponding to the tissue geometry were generated from the OCT-derived structural data as seen in Figure 4.5. The spatial discretization for all models was $\Delta x = \Delta y = 0.1$ mm and $\Delta z \leq 0.1$ mm. For the left atrium fiber-1 model, the fiber orientation was fitted to the model using the fitting module within Continuity 6, which uses a least-squares fitting approach.

For the lesion and human left atrial models, conduction relative to fiber direction was assumed to be isotropic as the fiber orientation could not be extracted throughout the tissue, limited by imaging depth or interference from the birefringence artifact. For the lesion models, the location of the lesions were also fitted to the geometric model via the fitting module in Continuity 6.
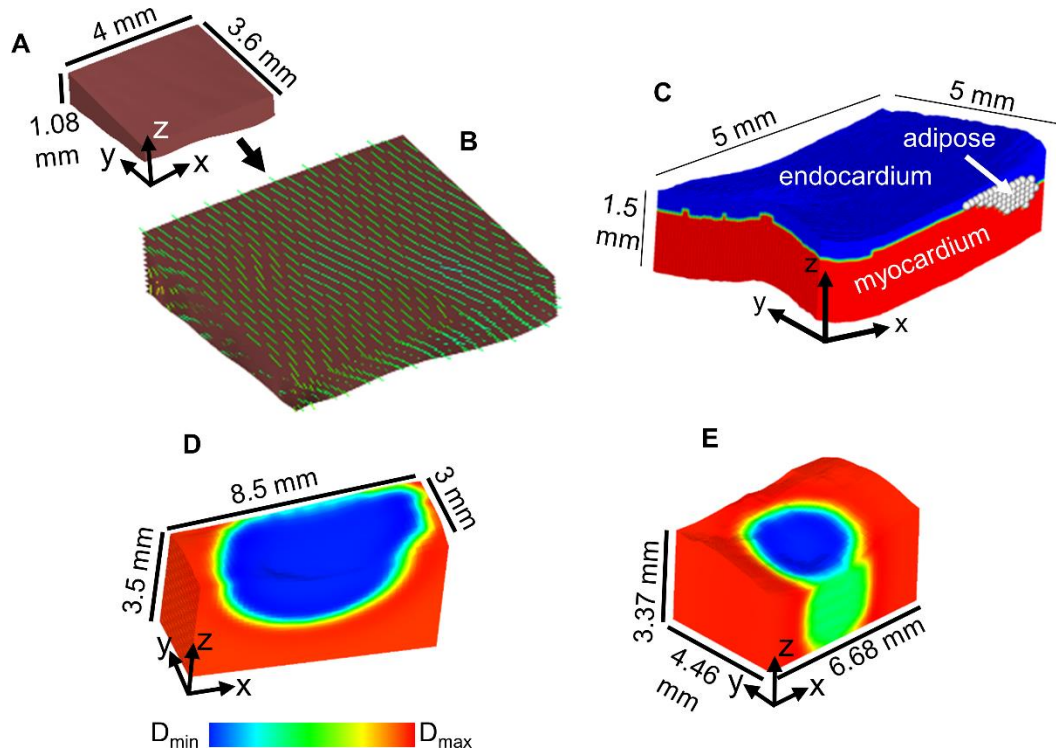
Figure 4.5 Finite element, hexahedral models for electrophysiological simulation, generated from OCT data of atrial tissues. A, Left atrium fiber-1 model, shown enlarged in B to show fitted fiber orientation superimposed on the model. C, Human left atrial model. D, Non-transmural lesion model. E, Transmural lesion model. For the lesion models, the fitted ablation lesion region is shown by a color map of assigned diffusivity (D) parameters.

For the left atrium fiber-2 model, a slab tissue geometry with uniform thickness was assumed, but incorporated the fiber orientation data within a 9.8 x 5.3 x 0.35 mm volume of myocardium. This volume of myocardium was extracted from the image volume starting 0.47 mm underneath the endocardial tissue surface to ensure extraction of information from the myocardium and not the

endocardium. Representative images of the extracted fiber orientation data from OCT and the fiber orientation fitted to the model are shown in Figure 4.6. Due to the simplistic geometry used, interpolation of the fiber data to the nodal locations of the model was deemed sufficient to fit the fiber angles to the model.
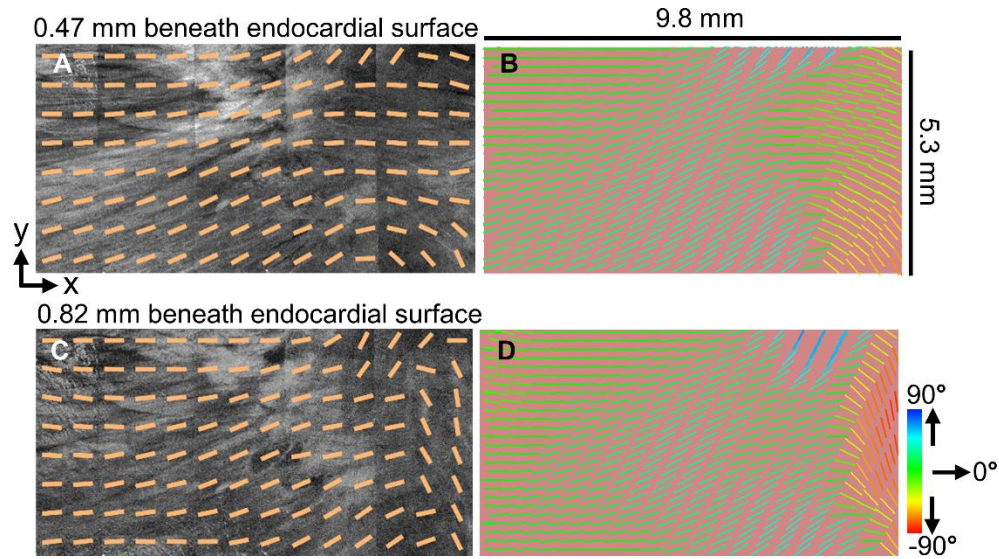
Figure 4.6 Left atrium fiber-2 slab model incorporating fitted fiber orientation as extracted from a 9.8 x 5.3 x 0.35 mm volume of myocardium imaged by OCT. *En face* OCT images with superimposed, extracted fiber angles at depths of A, 0.47 mm and C, 0.82 mm from the tissue surface. Corresponding fiber fields from A and C are shown fitted to the model in B and D, respectively.

To investigate the influence of detailed OCT-derived fiber orientation, two simplified variants of the left atrium fiber-1 and left atrium fiber-2 models were developed with less fiber complexity. First, the left atrium fiber-1 and left atrium fiber-2 models were developed without depth-resolved changes in fiber orientation, hereafter called transmurally uniform fiber orientation. For these models, the fiber orientation in the uppermost layer of elements on the model's stimulated surface was assigned to all layers underneath, thus retaining the spatial fiber orientation heterogeneity in the lateral dimensions but creating homogeneous fiber orientation transmurally. Second, the left

atrium fiber-1 and left atrium fiber-2 models were simplified to a uniform fiber orientation. To generate uniform fiber orientation, all fiber angles were aligned to the y-axis in the left atrium-1 model, and to the x-axis in the left atrium-2 model. This was based on which axis was closer to the dominant fiber orientation direction within each model. Additionally, to investigate the effect of tissue geometry on the electrical and optical signals, a uniform thickness model was developed with the same lateral dimensions as the left atrium fiber-1 model and with a uniform thickness equal to the average thickness of the left atrium fiber-1 model.

4.2.4.2 Electrophysiology Model and Simulation Parameters

For the left atrium fiber-1 and left atrium fiber-2 models, including their variants, anisotropic diffusivity was assigned such that the ratio of the longitudinal to the transverse conduction velocity was about 1.8, based on prior literature [16, 163]. For the ablated tissue models, isotropic conduction was assigned. The longitudinal conduction velocity was adjusted to 0.75 m/s [164] with diffusivity set to 0.1331 mm^2/ms. The transverse conduction velocity was adjusted to 0.42 m/s with diffusivity set to 0.0411 mm^2/ms. For isotropic conduction, a conduction velocity of 0.75 m/s was used. For the ablated tissue regions, the diffusivity and Fenton Karma ionic model excitability parameter, g_{fi}, were reduced to a minimum of ~0.1% in the lesion region to induce the non-conducting property of the lesion. For the human left atrial model, the conduction was isotropic and set to a velocity of 0.65 m/s, corresponding to a diffusivity of 0.1 mm^2/ms. The adipose and endocardium regions were modeled by decreasing the diffusivity and ionic excitability of the tissue to about $1/7^{th}$ to $1/10^{th}$ of the myocardium. To investigate the influence of different tissue electrophysiological properties, a simulation was run with the human left atrial model having conduction parameters of myocardium homogeneously throughout the model. For all electrophysiology simulations, point stimulation was applied on the surface of the models.

4.2.5 Light Scattering Simulation

4.2.5.1 Mesh Generation for Light Scattering Simulation

The tetrahedral meshes are shown in Figure 4.7. The refractive index of atrial myocardium was set to 1.4, or 1.46 if within the ablation lesion region to approximate structural changes such as increased collagen content [165, 166]. The refractive index of adipose tissue was set to 1.467, and the refractive index of the endocardium was set to 1.5, approximated from literature. [167-169] The mean element edge lengths for the swine left atrium fiber and uniform thickness models were about 0.06 mm, while the mean element edge length for the non-transmural and transmural lesion models were about 0.09 mm and 0.07 mm respectively. The mean element edge length for the human left atrial model was 0.06 mm.
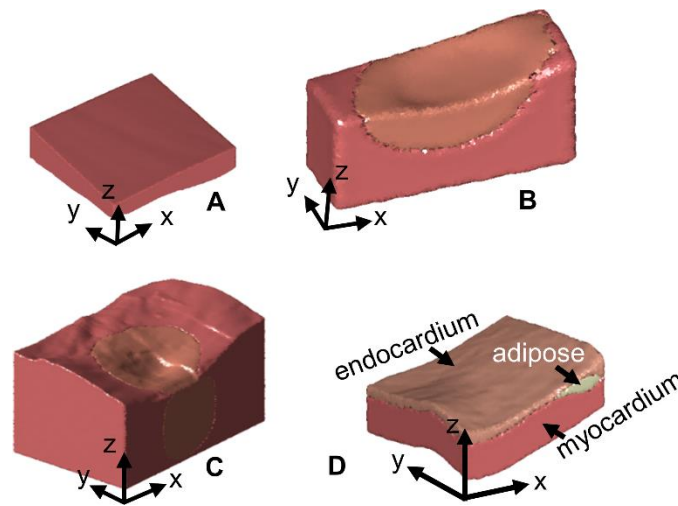
Figure 4.7 Tetrahedral models for optical simulation. A, Left atrium fiber-1 model. B, Non-transmural lesion model. C, Transmural lesion model. D, Human left atrial model.

4.2.5.2 Simulation of Tissue Illumination

The excitation wavelength, 488 nm, was chosen to match the wavelength of light used to excite the commonly used voltage-sensitive fluorescent dye, Di-4-ANEPPS. The optical parameters

(absorption coefficient μ_a, scattering coefficient μ_s, and anisotropy coefficient, g) used in the models for 488 nm are shown in Table 4.1. An approximation of the optical parameters of swine ablated and un-ablated tissue were obtained experimentally by diffuse reflectance measurements of swine atrial tissue samples and an inverse Monte Carlo procedure as described in a prior study [170]. The human myocardial, adipose, and endocardial tissue optical properties were approximated from literature. [167, 171, 172] To investigate the change in excitation photon density distribution caused by the lesion optical properties, an illumination simulation was also run for the non-transmural lesion model with the entirety of the model having the optical parameters of un-ablated tissue only.

Table 4.1 Optical Properties of Tissue Models at Excitation Wavelength 488 nm

Tissue Type	μ_a (mm^{-1})	μ_s (mm^{-1})	g
Swine Myocardium	0.62	17.2	0.95
Swine Ablation Lesion	0.68	19.2	0.95
Human Myocardium	0.52	23.0	0.94
Human Adipose	0.16	14.1	0.98
Human Endocardium	0.11	93.5	0.8

4.2.5.3 Simulation of Fluorescence Emission

The emission wavelength, 669 nm, was chosen to match the wavelength of light commonly measured with the voltage-sensitive fluorescent dye, Di-4-ANEPPS. The optical parameters used in the models for 669 nm are shown in Table 4.2 and were obtained with the same methods used to obtain the optical properties at the excitation wavelength.

Table 4.2 Optical Properties of Tissue Models at Emission Wavelength 669 nm

Tissue Type	μ_a (mm^{-1})	μ_s (mm^{-1})	g
Swine Myocardium	0.075	13.6	0.95
Swine Ablation Lesion	0.104	16.2	0.95
Human Myocardium	0.1	21.8	0.96
Human Adipose	0.12	63.0	0.978
Human Endocardium	0.02	11.3	0.85

4.2.6 Data Analysis and Computational Resources

Activation time, transmural activation time, action potential upstroke duration, and fractional level of maximum upstroke velocity were computed to quantify the simulated electrical and optical action potentials. Activation time was computed as the time of the upstroke's maximal derivative [173]. Total activation time was defined as the latest activation time. Transmural activation time was defined as the difference between the activation times on the stimulated surface of the model from the activation times on the opposing surface of the model. Specifically, the transmural activation time at a particular x-y coordinate was computed by subtracting the activation time at the x-y point on the stimulated surface of the model from the activation time at the point on the opposite surface of the model with the same x-y coordinates. Action potential duration was calculated as the time between 10% and 90% depolarization. The action potential upstroke duration is reported as mean ($\pm$ 1 SD). The fractional level of maximum optical upstroke velocity, V_{f*}, is a parameter that has been established in past optical mapping studies [145, 153], where it was used to describe changes in optical upstroke morphology with respect to direction of electrical propagation. The parameter quantifies the time of the maximum upstroke velocity and ranges from 0 to 1. A higher value of V_{f*} indicates the location of the maximum upstroke velocity is near the apex of the upstroke, while a lower value indicates the maximum upstroke velocity is near the foot of the upstroke [145, 153]. V_{f*} was detected within the 10% to 90% depolarization interval. To compute the derivatives of the upstroke, the upstrokes were first interpolated with piecewise cubic polynomials to a discretization of about 6.5 μs, before a first order, one-sided finite difference method was applied. Simulations were run on Columbia University's Yeti Shared High Performance Computing Cluster and the Rocce cluster from the National Biomedical Computation Resource.

4.3 Results

4.3.1 Electrophysiology Results

4.3.1.1 Fiber Orientation Models

Electrical activation maps, transmural electrical activation maps, and differences between transmural electrical activation maps for the left atrium fiber-1 and left atrium fiber-2 models are given in Figure 4.8. The difference in surface electrical activation pattern with tissue-specific fiber orientation compared to activation with uniform fiber orientation is apparent when comparing Figure 4.8A to Figure 4.8C, and Figure 4.8I to Figure 4.8K. As expected, the surface activation between the tissue-specific and transmurally uniform fiber orientation models were nearly identical, as seen Figure 4.8A-B and Figure 4.8I-J. Total activation time tended to increase with increasing complexity of fiber orientation. The left atrium fiber-1 model had a total activation time of 7.7 ms with tissue-specific fitted fiber orientation, 7.6 ms with transmurally uniform fiber orientation, and 7.3 ms with uniform fiber orientation. For the left atrium fiber-2 model, the total activation time of the model with tissue-specific fitted fiber orientation and transmurally uniform fiber orientation were the same, with a total activation time of 12.0 ms. The total activation time of the left atrium fiber-2 model with uniform fiber orientation was 11.2 ms. For the left atrium fiber-1 model, subtle differences can be observed between the transmural activation maps of the model's variants, as shown in Figure 4.8D-F. To more clearly show these differences, Figure 4.8G-H show the transmural activation times of the simplified fiber models subtracted from the transmural activation times of the tissue-specific fiber model, showing differences up to about 0.4 ms. For the left atrium fiber-2 model, the transmural activation times were low due to the thinness of the mesh. However, the tissue-specific fiber orientation induced non-zero transmural activation time up to about 0.2 ms as seen in Figure 4.8L, while the transmurally uniform and uniform fiber orientation models had zero transmural activation time throughout the majority of the model, as

shown in Figure 4.8M-N. Accordingly, the difference maps of Figure 4.8O-P closely resemble the transmural activation time map from the fully fitted left atrium fiber-2 model of Figure 4.8L.
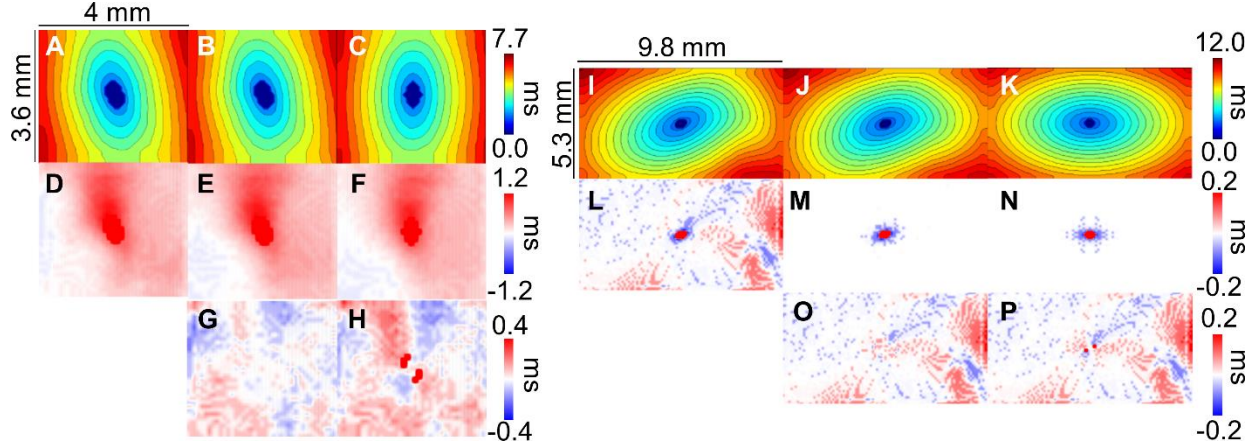
Figure 4.8 Electrical activation maps, transmural electrical activation maps, and differences between transmural electrical activation maps for the left atrium fiber-1 model, left atrium fiber-2 model, and their variants. Isochronal activation maps of the stimulated surface for left atrium fiber-1 model with A, tissue-specific fitted fiber orientation, B, transmurally uniform fiber orientation, and C, uniform fiber orientation. Black isolines indicate 0.5 ms intervals. Transmural activation maps for the left atrium fiber-1 model with D, tissue-specific fitted fiber orientation, E, transmurally uniform fiber orientation, and F, uniform fiber orientation. Difference in transmural activation times between the left atrium fiber-1 model with tissue-specific fiber orientation and G, transmurally uniform fiber orientation and H, uniform fiber orientation. Isochronal activation maps of the stimulated surface for left atrium fiber-2 model with I, tissue-specific fitted fiber orientation, J, transmurally uniform fiber orientation, and K, uniform fiber orientation. Black isolines indicate 0.5 ms intervals. Transmural activation maps for the left atrium fiber-2 model with L, tissue-specific fitted fiber orientation, M, transmurally uniform fiber orientation, and N, uniform fiber orientation. Difference in transmural activation time between the left atrium fiber-2 model with tissue-specific fiber orientation and with O, transmurally uniform fiber orientation and P, uniform fiber orientation.

4.3.1.2 Human Left Atrial Model

Electrical activation time maps of the surface opposing the stimulated surface in the human left atrial model are given in Figure 4.9. Comparing the results from the model containing

heterogeneous tissue types, given in Figure 4.9A, to the results from the model containing homogeneous tissue types, as shown in Figure 4.9B, it can be seen that the activation time is less uniform in the heterogeneous model, no longer having a simple ellipsoidal shape radiating from the stimulus point. Additionally, the activation of the entire model took longer in the model with heterogeneous endocardium, myocardium, and adipose parameters, with the total activation time being 19.6 ms for the heterogeneous model and 11.2 ms for the homogeneous model. The difference between the activation times shown in Figure 4.9A and B is given in Figure 4.9C. The most difference occurred in the bottom-right corner, where there was significant adipose and endocardial thickness.
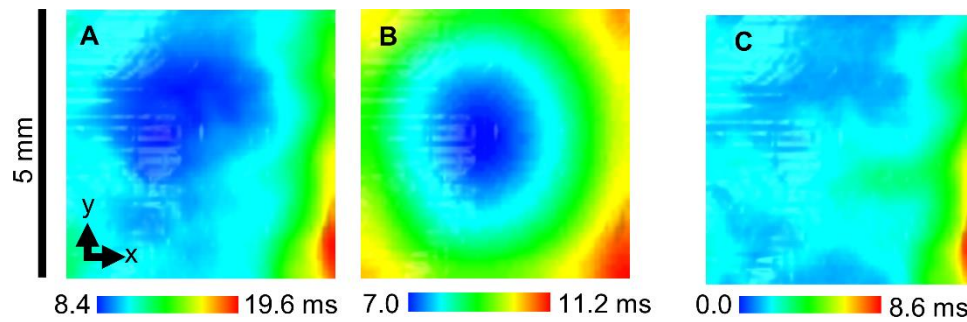
Figure 4.9 Electrical activation time maps for the human left atrial model with A, myocardium, endocardium, and adipose tissue properties, and B, homogeneous myocardium properties, as seen from the stimulated surface of the model. C, Difference between electrical activation time between B and A.

4.3.2 Illumination Results

4.3.2.1 Fiber Orientation Models

The distribution of excitation photon density was slightly different between the left atrium fiber-1 model containing tissue geometry and the uniform thickness model. In the epicardial distributions of excitation photon density as shown in Figure 4.10A and Figure 4.10B, the photon density distribution in the tissue-specific model was greater towards the left region of the model while it

was more symmetric in the uniform thickness model. In transmural cross-sections, the illuminating light was not fully attenuated through the thin tissues upon reaching the endocardial surface of the pictured cross-sections, as illustrated in Figure 4.10C and D.
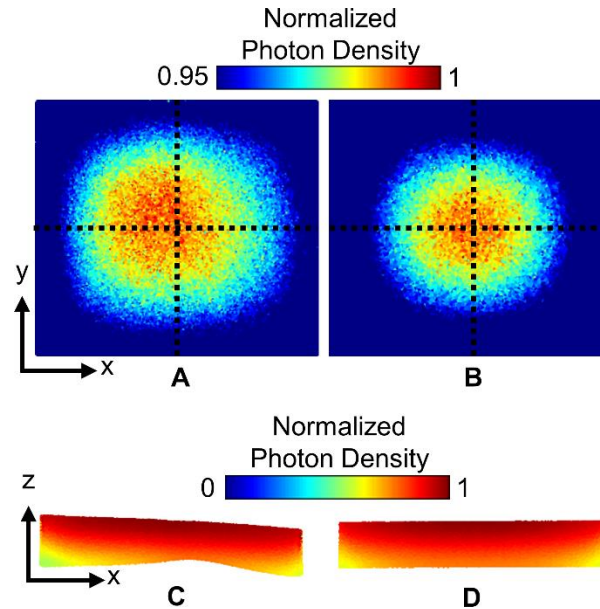
Figure 4.10 Excitation photon density on the left atrium fiber-1 model and uniform thickness model. The photon density is normalized with respect to the maximum density in each model, exempting values on the lateral boundaries of the models due to boundary effects. A, Epicardial map and C, cross-sectional view at y = 1.8 mm, on the left atrium fiber-1 model. B, Epicardial map and D, cross-sectional view at y = 1.8 mm, on the uniform thickness model. The epicardial map color values are shown starting from 95% of the maximum photon density to enhance the contrast of the surface photon density distribution. Crosshairs on the epicardial maps depict the center of the surface.

4.3.2.2 Lesion Models

For the non-transmural lesion model, the excitation photon scattering was simulated with and without the lesion region to determine the effect of the lesion optical properties on the penetration of excitation light. The difference between the excitation photon density within the model with and without the lesion, scaled to the maximum excitation photon density in the model without the lesion, is shown in Figure 4.11. The inclusion of the lesion region, which had increased scattering

and absorption compared to un-ablated tissue, caused a slight increase in the excitation photon density close to the ablated tissue surface, and a decrease throughout the rest of the lesion area.
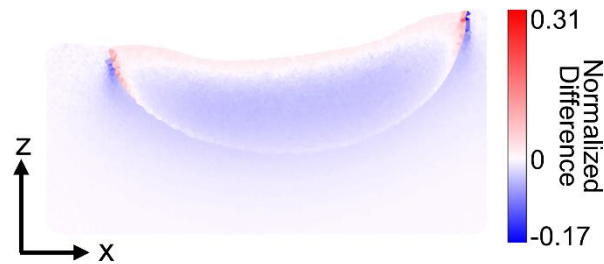
Figure 4.11 Cross-sectional view of the difference between the excitation photon density in the non-transmural lesion model with and without the lesion region included, at y = 1.5 mm. The difference is scaled to the maximum excitation photon density in the model without the lesion.

4.3.2.3 Human Left Atrial Model

A representative view of the excitation photon density in the human left atrial model after illumination is provided in Figure 4.12A, with the corresponding distribution of tissue types shown in Figure 4.12B for comparison. Most of the excitation photon density was concentrated within the endocardial and adipose tissue layers, with a decrease in excitation photon density at the boundary between the two other tissue types and the myocardium.
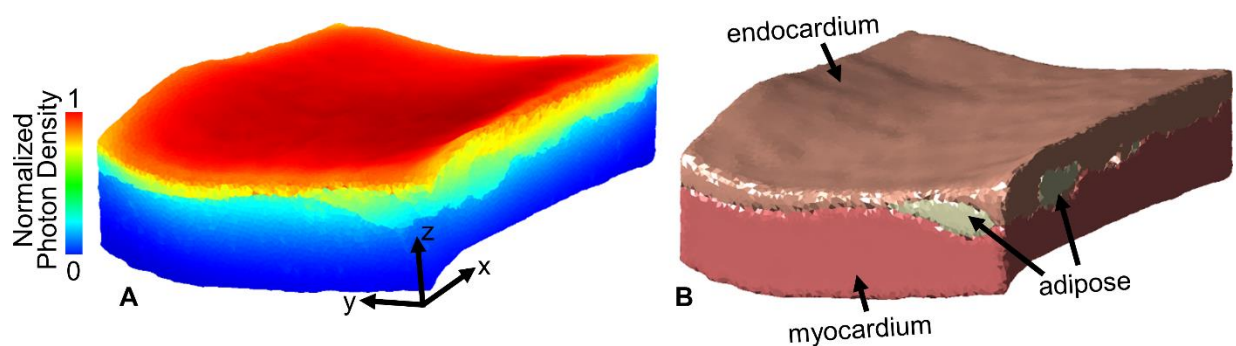
Figure 4.12 Excitation photon density on the human left atrial model with myocardium, adipose, and endocardium parameters. A, Excitation photon density over the model. B, Model showing the distribution of adipose, myocardium and endocardium tissues.

4.3.3 Fluorescent Emission Results

4.3.3.1 Fiber Orientation Models

As in the illumination simulation, the optical mapping signal amplitude between the tissue-specific left atrium fiber-1 model and the uniform thickness model had different distributions, reflecting the influence of the thin tissue geometry. The epicardial maps of the optical mapping signals in Figure 4.13A and Figure 4.13B show the asymmetric distribution within the tissue-specific model in contrast to the uniform thickness model. In comparison to the tissue thickness map shown in Figure 4.13C, the signal amplitude in the tissue-specific model was generally lower within approximate regions of thinner tissue and higher around thicker regions.
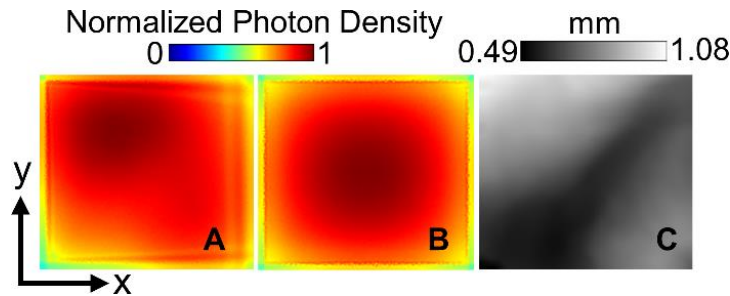
Figure 4.13 Tissue thickness and optical mapping signal distribution for the left atrium fiber-1 model and uniform thickness model. A, Epicardial distribution of the optical mapping signal in the left atrium fiber-1 model, at t = 9 ms. B, Epicardial distribution of the optical mapping signal in the uniform thickness model, at t = 9 ms. C, Tissue thickness of the left atrium fiber-1 model. The photon density is normalized to the maximum photon density on the top surface of the model.

Optical activation time maps and distributions of the fractional level of maximum upstroke velocity V_{f*} for the left atrium fiber-1 model are shown in Figure 4.14. The trends of optical

activation time seen in Figure 4.14A-C correspond to that of the electrical activation times shown in Figure 4.8A-C. The fractional level of maximum upstroke velocity is a parameter that has been used in prior studies to characterize the correlation between the optical upstroke morphology and the angle of propagation of the subsurface electrical wavefront with respect to the tissue surface [145, 153]. In agreement with past studies, the values of V_{f*} increased from the point of stimulation. The pattern of V_{f*} followed the surface activation pattern from the electrophysiological simulation. Differences in V_{f*} up to about 60% were observed between the V_{f*} maps of the tissue-specific fitted fiber model when compared to the V_{f*} maps of the transmurally uniform fiber model or uniform fiber model. These differences were especially apparent at the areas where the propagation of the electrical wavefront transitioned from moving away from the stimulated surface to an angle moving towards the stimulated surface. Differences were minimal at regions where V_{f*} had reached a maximum. Comparing Figure 4.14G-H to Figure 4.8G-H, correlation of the differences in V_{f*} between the different fiber distributions to the differences in transmural activation times were not apparent.
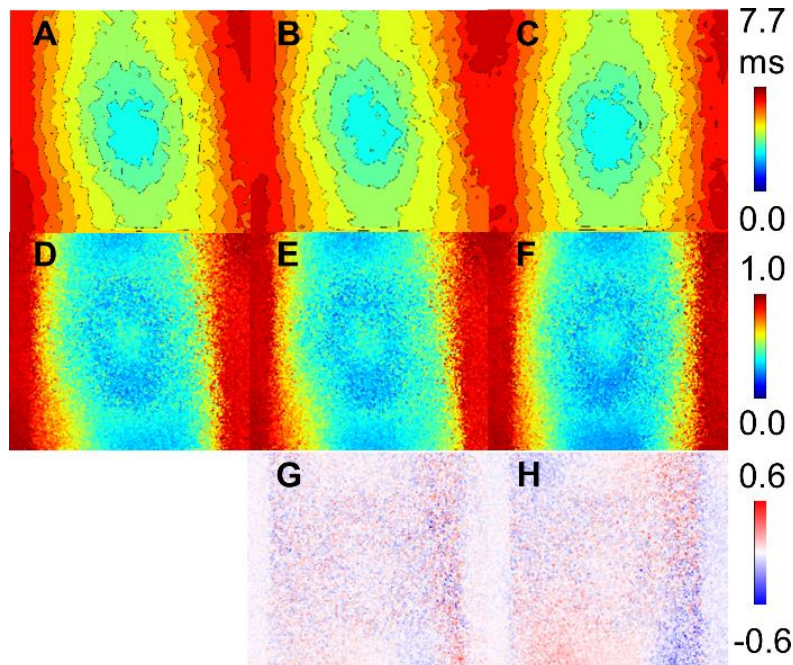
Figure 4.14 Optical activation and V_{f*} maps for the left atrium fiber-1 model and its variants. Isochronal optical activation maps of the stimulated surface for A, tissue-specific fitted fiber model, B, transmurally uniform fiber model, and C, uniform fiber model. Black isolines indicate 0.5 ms intervals. V_{f*} maps for D, tissue-specific fitted fiber model, E, transmurally uniform fiber model, and F, uniform fiber model. Difference in V_{f*} between tissue-specific fitted fiber model and G, transmurally uniform fiber model and H, uniform fiber model.

Optical upstroke prolongation was observed. For the left atrium fiber-1 model, the electrical upstroke duration was 1.1 ($\pm$ 0.3) ms, while the optical upstroke duration was 3.1 ($\pm$ 0.3) ms.

4.3.3.2 Lesion Models

For the lesion models, the blurring of optical signals into regions that were electrically inactivated could be observed. As seen within the optical mapping signal snapshots shown in Figure 4.15A and B, the minimum normalized optical mapping signal amplitude was higher within the transmural lesion. To better understand the relative contribution of fluorescent signal throughout the tissue, Figure 4.15C and D show the density of emitted fluorescent photons for the same time points as the optical mapping snapshots in a transmural cross-section of the tissue. The density of emitted photons is weighted by the distribution of excitation photon density and transmembrane potential, and the absence of emitted photons within the electrically inactivated lesion area can be seen by the darkened regions near the upper tissue surface. The density of emitted photons can also be seen to decrease with depth due to the decay of excitation intensity. As seen in Figure 4.15C, electrical propagation occurring underneath the non-transmural lesion did not contribute heavily to the fluorescent signal due to the low intensity of illumination at that depth.
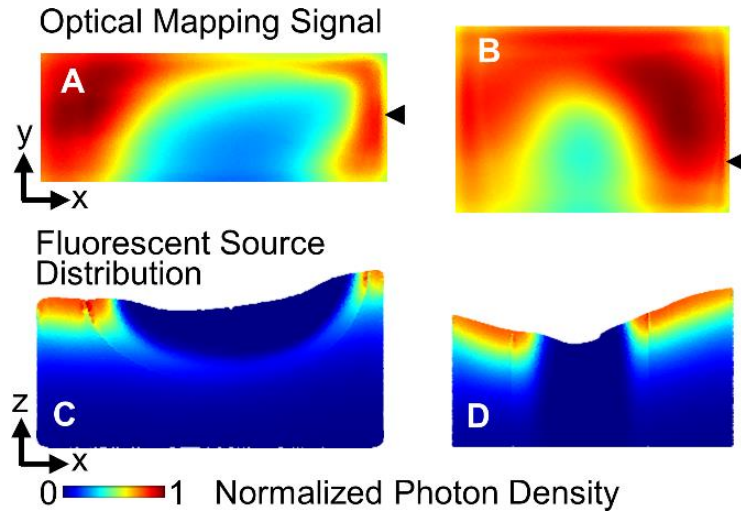
Figure 4.15 Optical mapping results in the lesion models. A, Endocardial map of optical mapping signal distribution and C, transmural cross-section of emitted fluorescent photon density distribution at y = 1.5 mm, at t = 23 ms, in the non-transmural lesion model. B, Endocardial map of optical mapping signal distribution and D, transmural cross-section of emitted fluorescent photon density distribution at y = 1.2 mm, at t = 21 ms, in the transmural lesion model. The optical mapping signal photon density is normalized to the maximum photon density on the top surfaces of the models. The emitted fluorescent photon density distribution is normalized to the maximum photon density within the cross-section. Black arrows indicate the location of the transmural cross-sections along the y axis.

4.3.3.3 Human Left Atrial Model

Snapshots of the optical mapping signal, and corresponding electrical signal, on the heterogeneous and homogeneous human left atrial model are given in Figure 4.16. Blurring in the optical mapping signal significantly masked the heterogeneity of the electrical signal distribution. Comparing Figure 4.16A to Figure 4.16B, the distribution of the transmembrane potential is more non-uniform in the heterogeneous model shown in Figure 4.16A. However, in the corresponding optical mapping signal in Figure 4.16C, the non-uniformity is smoothed out to a similar ellipsoidal morphology as seen in the optical signal of the homogeneous model in Figure 4.16D.
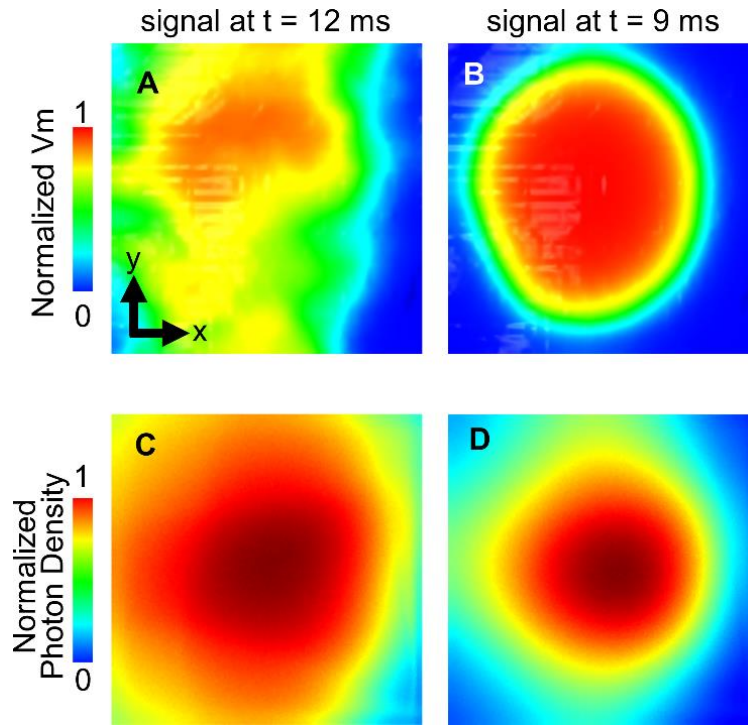
Figure 4.16 Snapshots of electrical and optical mapping signals as seen from the surface opposing the stimulated surface of the model. A, Normalized transmembrane potential (Vm) from the model with myocardium, collagen, and adipose properties, at t = 12 ms. B, Vm from model with only myocardial properties, at t = 9 ms. C, Optical mapping signal from model with myocardium, collagen, and adipose properties, at t = 12 ms. D, Optical mapping signal from model with only myocardial properties, at t = 9 ms. The optical mapping signal distribution is normalized with respect to the maximum optical signal in the model at the given time.

4.4 Discussion

This study demonstrated the first applications of OCT-derived atrial tissue models for electrophysiology and optical mapping simulations. Five different models were developed containing tissue structural characteristics extracted from OCT imaging, including tissue geometry, fiber orientation, ablated tissue location, and different tissue types. The effects of the incorporated tissue structure on the simulated electrical and optical signals were analyzed. Our objective for developing tissue-specific atrial models is to facilitate deeper investigation of the

relationship between atrial electrophysiological function and detailed tissue-specific structure to improve the understanding and treatment of atrial fibrillation.

4.4.1 Influence of Depth-Resolved Fiber Orientation

OCT offers depth-resolved, micrometer-scale information on fiber orientation, which can be useful when considering transmural electrophysiological dynamics. Depth-resolved variation in fiber orientation led to changes in transmural activation time. This was observed in the left atrium fiber-1 and left atrium fiber-2 models by the differences in transmural activation time between the tissue-specific fitted fiber orientation models and their simplified fiber variants. With recent interest in the difference between epicardial and endocardial electrical activation during atrial fibrillation [14], high resolution and depth-resolved fiber orientation information offered by OCT may be helpful in understanding arrhythmia dynamics.

We also investigated the ability of optical mapping signals to reflect such changes in electrophysiological transmural activation. Optical mapping simulations and experimental studies by Hyatt et al. demonstrated that the subsurface orientation of the propagating electrical wavefront with respect to the tissue surface is correlated to the optical upstroke morphology [145]. However, it has been demonstrated in anatomic optical mapping models [72, 76] and experiments [153] that patterns of electrical propagation and consequently extracted V_{f*} can become more complex due to tissue heterogeneities and fiber orientation. Changes in the surface electrical activation patterns due to anisotropic conduction along fibers were reflected in the V_{f*} maps. As seen within the difference maps of Figure 4.14G and H, varying depth-resolved fiber orientation altered the optical upstroke distribution and emphasizes the influence of structure on electrophysiological propagation and subsequently optical mapping signal characteristics. These differences appeared

to be more significant closer to the stimulus point and particularly as the wavefront transitioned from traveling away to traveling towards the tissue surface.

4.4.2 Ablation Lesion Geometry and Fluorescence

In addition to incorporation of fiber orientation, we were also able to build OCT-derived tissue-specific models of ablation lesions and simulate optical mapping in the models to observe the interaction between the electrical and optical signals and the lesions. The blurring of the optical signal compared to the electrical signal around the boundaries of the lesion was observed. In particular, the minimum, normalized optical signal intensity was higher in the transmural lesion within our simulations. There was a low contribution to the optical mapping signal from the electrical propagation occurring underneath the non-transmural lesion due to the decay of excitation intensity. Thus, the lateral scattering from the regions surrounding the lesion contributed more significantly to the optical mapping signal. Due to the smaller diameter of the transmural lesion, this can explain the higher optical signal intensity within the transmural lesion and emphasizes the need to be aware of the origin of the optical signal when relating lesion depth to optical signal amplitude. Modeling of light propagation in tissue-specific conditions could assist in the development of optical techniques to monitor lesion formation, such as those using endogenous nicotinamide adenine dinucleotide (NADH) fluorescence [174] or near infrared-spectroscopy [170]. Tissue-specific ablation models could be used to evaluate and analyze the behavior of the optical techniques in a realistic model containing heterogeneities that would otherwise complicate use of the techniques.

4.4.3 Influence of Heterogeneous Tissue Types

Finally, we generated a human atrial tissue model containing heterogeneous tissue types including endocardium and adipose tissue. It was shown that the inclusion of these different tissue

107

types led to non-uniformity of conduction and slowing of activation time. Alteration in conduction properties caused by heterogeneous tissue composition could be associated with arrhythmic dynamics, and the structural detail provided by OCT could lead to more realistic models of electrical propagation within the atria and provide valuable insights on structure-function relationships. Furthermore, it was shown that the characteristic blurring of the optical mapping signal obscures details of the heterogeneous electrical propagation. Therefore, optical mapping models of heterogeneous tissues could better define the interpretation of optical mapping results.

4.4.4 Limitations and Future Work

This study demonstrated a framework for developing OCT-derived atrial tissue models and showed influences of OCT-derived structural features on the electrophysiological and optical signals. However, a larger imaged tissue region would be helpful to enable a more thorough investigation of arrhythmia dynamics in large animals or human hearts and the influences on electrical and optical signals with respect to detailed structural information. The lateral field of view can be enlarged by stitching a larger number of OCT volumes, while the imaging depth of OCT could be expanded by imaging and stitching both sides of the tissue, imaging thick serial sections of the tissue, or through optical clearing combined with imaging by a swept-source (SS)-OCT system. SS-OCT systems offer higher imaging depths due to the use of longer wavelength light sources and could enable high-resolution imaging of deeper tissue structure without complications of image registration or potential artifacts from sectioning. However, future work remains in obtaining the best balance between tissue contrast and depth penetration with optical clearing.

Limitations of this study include lack of experimental validation, which would require registration of optical mapping data from the tissue to its OCT-derived model. Although the optical

mapping signal characteristics observed within this study, such as the optical signal blurring and morphology changes, are in line with prior experimental and modeling results, direct experimental comparison would be necessary to fully validate tissue-specific effects and parameters. In this study, electrophysiological and optical parameters were informed by literature. Additionally, while optical absorption and scattering parameters were obtained from a swine tissue sample through an inverse Monte Carlo method, the reduced scattering coefficient, as opposed to the scattering coefficient, was obtained. The scattering coefficient was estimated from the reduced scattering coefficient and an approximate value of the anisotropy coefficient, near the range found in prior literature [172], due to lack of existing information on swine atrial optical properties. The tissue was also not stained with voltage-sensitive dye when the optical parameters were measured. With regards to lesion imaging and modeling, OCT was unable to detect the lesion depth. Furthermore, changes in endocardial and myocardial contrast as the marker for lesion boundaries may vary in alignment between the lesion necrotic core and border zone. Establishing a more accurate framework for electrophysiological and optical modeling of the lesion in detail is a focus for future investigation. Lastly, due to the different algorithms used for generation of the hexahedral and tetrahedral meshes and different simulation approaches of the electrical and light propagation, registration between the two models have slight differences, primarily in the lesion model which has a smoothly transitioning lesion boundary in the electrophysiological model but a sharp boundary within the photon scattering model.

The next steps for OCT-derived optical mapping atrial models include the modeling of larger tissue regions, including the incorporation of more varying tissue types such as fibrosis, and ultimately working towards a comprehensive visualization and model of the whole atria utilizing stitched OCT image volumes. Future studies will also include further study of OCT-derived lesion

models, including simulation of electrical propagation with multiple ablation lesions of varying sizes and configurations, and inclusion of transmural myofiber orientation to allow a more detailed understanding of varying electrophysiological conduction and block around ablated areas in different conditions. In the future, OCT imaging could also be registered with MRI or CT-derived data for a multi-modality imaging approach.

4.5 Conclusion

OCT-derived atrial models have the potential to provide additional, high resolution, tissue-specific structural detail in simulations of cardiac electrophysiology and optical mapping. This study has demonstrated the framework for OCT-derived tissue-specific, optical mapping models of the atria, which has the potential to enable a more direct comparison between simulation and experimental results. Optical mapping models of atrial tissue as derived from OCT have the potential to guide deeper investigation of the relationship between cardiac function and detailed tissue microstructure.

Chapter 5 Summary and Future Work

5.1 Conclusion

The underlying principles of atrial fibrillation remain incompletely understood, and it is clear from years of research that the mechanisms of this highly prevalent arrhythmia are heterogeneous, complex, and patient-specific. Detailed understanding of the tissue structure that contributes to atrial fibrillation dynamics can improve understanding of abnormal electrophysiological patterns and ultimately inform better treatments. Within this work, we explored the use of OCT in identifying tissue microstructure of the entire human left atrium for the first time, and established a framework for applying OCT to tissue-specific models for studying cardiac electrophysiology.

In Chapter 2, we studied comprehensive OCT imaging of human left atrial tissue within the context of human left atrial anatomy, as well as discussed the whole human heart OCT imaging atlas. Large, centimeter-scale OCT imaging maps were registered to a model of the human left atrium to correlate imaging features to left atrial geometry. Imaging features for various tissue types within the human left atrium were established through correlation to Trichrome histology, including endocardium, myointimal thickening, collagen fibers, adipose tissue, and venous media. The distribution of OCT-imaged adipose tissue and fiber orientation through human left atria, as well as the transition of myocardial sleeves within the pulmonary veins to regions of only venous media and adventitia, were identified. Notably, the ability of OCT to identify specific densities and distributions of collagen fibers within the myocardium was also demonstrated, showing promise for OCT to provide an improved understanding of the interaction between different types of fibrotic regions and electrophysiology. The data from this study enable an improved understanding of the microstructure of human left atrial tissue, and could guide the

111

application of real-time, structural substrate identification using OCT-integrated catheters or *ex vivo*, cardiac OCT imaging studies. More generally, the human cardiac OCT atlas could also guide OCT applications to the study of cardiac disease throughout the human heart.

In Chapter 3, a modeling protocol for the development OCT-based tissue-specific models of atrial tissue was established. Electrophysiological simulations using a hexahedral, finite element modeling scheme were combined with a tetrahedral-based, Monte Carlo photon scattering model to simulate optical mapping in tissue-specific models of heterogeneous tissue structure. Tissue-specific features such as myofiber orientation, ablation lesions, and varying tissue types could be extracted from the OCT image volumes and incorporated into the finite element models through fitting and interpolation. This workflow provides a basis for OCT-derived optical mapping models.

In Chapter 4, applications of OCT-informed models for optical mapping simulation were demonstrated. Five different models were generated: two models containing OCT-extracted myofiber orientation, two models containing ablation lesions, and one model containing heterogeneous tissue types. Changes in transmural activation time were seen when incorporating tissue-specific, depth-resolved fiber orientation, which translated into changes in the distribution of the morphology of the correlated optical mapping upstrokes. Modeling tissue-specific ablation lesions enabled a better understanding of the distribution of fluorescent signals corresponding to non-transmural and transmural lesions with respect to lesion geometry as well as the scattering and absorption of illumination and fluorescent light. Finally, we were able to observe that the inherent blurring of optical mapping signals obscured non-uniformity in the electrophysiological signal in the presence of heterogeneous tissue microstructure. It is possible that with the

combination of optical mapping models derived from tissue-specific OCT images, better understanding of the relationships between tissue structure and function could be made.

5.2 Future Work

Work remains in relating OCT-derived imaging of atrial tissue structure to the understanding of arrhythmia. Future work of particular interest include correlations of imaging data to disease, augmentations in the imaging protocol to provide increased depth penetration, more advanced image processing to maximize the utility of the obtained imaging data, more comprehensive OCT-informed cardiac models, and explorations *in vivo* to further establish the applicability of structural substrate characterization during ablation using OCT-integrated catheters.

5.2.1 Correlation of Imaging Data to Disease

The large volume of OCT imaging data in the human left atrium and across human hearts accumulated within this study provides a large amount of information about cardiac tissue structure that may be able to be correlated to disease. As OCT is able to provide detailed information about tissue structure unable to be previously captured by other imaging modalities; such as endocardial thickness, fibrosis organization and density, myointimal thickening, and intra-myocardial adipose infiltrations; identifying any correlations with these OCT-identified tissue structures with cardiac pathologies may offer new insights on disease mechanisms.

5.2.2 Increasing Imaging Depth

Although the work carried out within this study was done without processing the tissue to better understand the usefulness of OCT *in vivo*, the high-resolution imaging provided by OCT can also be used as an alternative to histology, which may be expensive and time-consuming. However, OCT is limited by its penetration depth, which practically provides useful imaging data about 1

mm into the tissue. This can be circumvented through serial sectioning methods as well as optical clearing, which have both been successfully applied in small animal hearts to improve imaging depth. [94, 97] As a preliminary example, Figure 5.1 shows a B-scan of swine left atrial tissue optically cleared by a 2,2'-thiodiethanol (TDE)-based aqueous solution [175] and imaged by a custom-built SS-OCT system [176], showing tissue contrast throughout the tissue thickness of about 2 mm. Combined with increased optical depth penetration induced by optical clearing, imaging with an SS-OCT system could enable high-resolution imaging of deeper tissue structure.
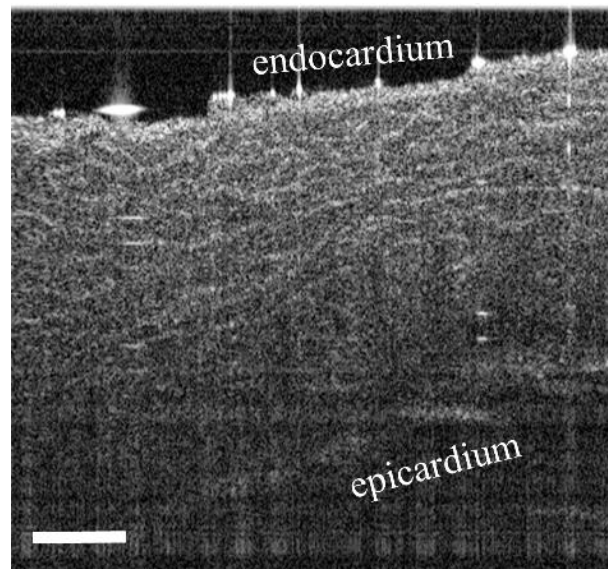
Figure 5.1. Representative SS-OCT B-scan from a swine left atrial sample optically cleared by a TDE-based aqueous solution. Scale bar indicates 0.5 mm.

5.2.3 Automatic Tissue Classification

Due to the large volume of data collected by OCT over the whole human left atrium, automatic image processing algorithms would assist in interpretation of the data and in providing more quantitative measurements. While work in automated tissue classification of human left atrial tissue has been developed and tested [118], it is limited to an assumption of a layered tissue

structure. During the work of this thesis, however, initial studies were carried out on the automated detection of adipose tissue, fiber orientation, and endocardial thickness. An initial study on the detection of adipose tissue within larger imaged regions of human left atrial tissue was conducted by adopting an algorithm that was used to identify adipose tissue in breast tissue, shown in Figure 5.2. [177] The results show promise of being able to automatically detect distributions of tissue composition over a widespread area.
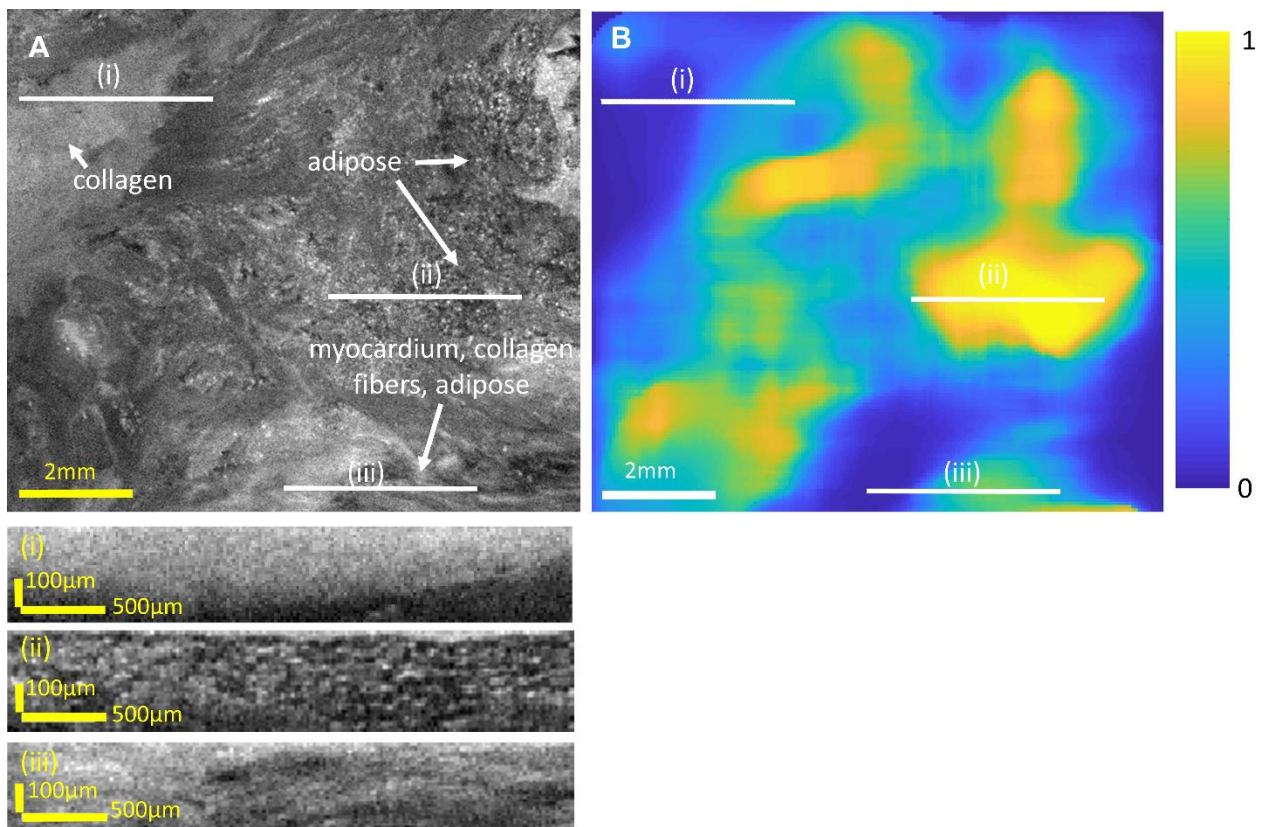
Figure 5.2. Automatic detection of adipose tissue in a stitched human left atrial image map. A, *En face* OCT image, shown 0.27 mm from the endocardial surface; B, adipose map with a probability of containing adipose tissue in the A-line of each lateral location; (i) OCT B-scan with collagen; (ii) OCT B-scan with adipose tissue; (iii) OCT B-scan with a mix of fibrotic myocardium and adipose tissue. Figs (i-iii) correspond to the white lines shown in A and B.

Preliminary results on the detection of endocardial thickness are provided in Figure 5.3, using a modified version of the layer detection algorithm described in a prior study. [118] Manual measurements by segmentation in IMOD are shown as a comparison. However, due to the highly laborious nature of manual measurements, interpolation was carried out across individually segmented B-scans, blurring the manual measurements and incurring its own inaccuracies. As demonstrated in the figure, the algorithm provides a good approximation of endocardial thickness where the endocardial thickness changes drastically. However, limitations remain in accurate representation of endocardial thickness from automated segmentation due to the gradual fall-off of intensity in regions where the endocardial thickness is beyond the penetration depth of OCT. Such ambiguity can cause difficulties in segmentation even with manual measurements. Therefore, it is likely that a confidence parameter will need to be incorporated into the algorithm in future developments. Detection of tissue composition such as endocardium can also, alternatively, be explored using a deep learning approach.

116
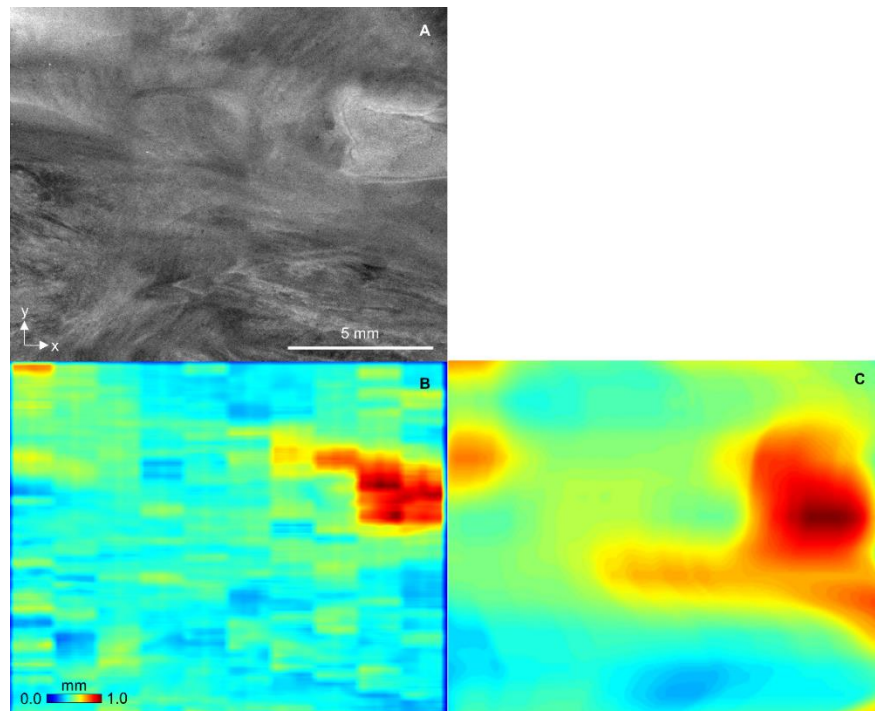
Figure 5.3. Automated endocardial thickness segmentation from an OCT *en face* image map. A, *En face* OCT image, shown 0.46 mm from the endocardial surface. B, Extracted endocardial thickness map from automated algorithm. C, Manually segmented endocardial thickness map.

Fiber directionality was extracted using a previously described OCT fiber tracking algorithm, [137] which captured the overall trend of the fibers. However, further filtering is required to remove regions of artifact incurred by areas of thick endocardium.
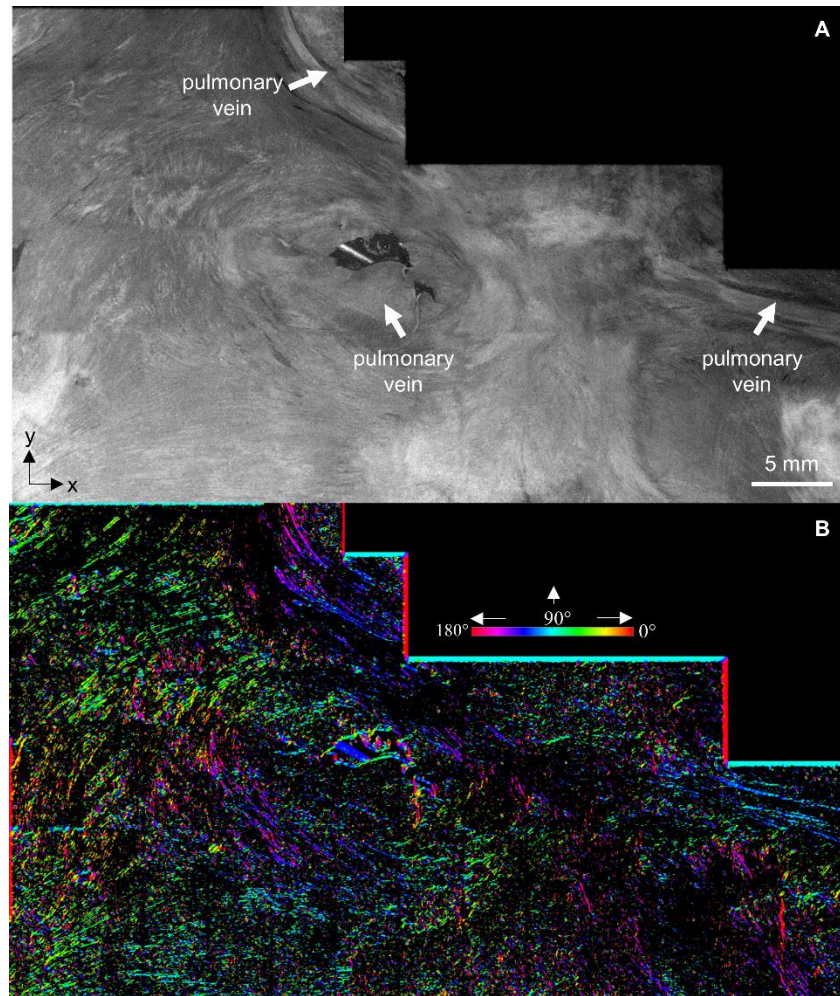
Figure 5.4. Automated detection fiber orientation. A, *En face* OCT image of myofiber orientation seen 0.51 mm beneath the endocardial surface. B, Fiber orientation extracted using a pixel-wise algorithm.

The preliminary results shows great promise, although further work remains in testing the robustness of the algorithms over the large OCT dataset comprising the whole human left atrial tissue. Additionally, the appropriate processing of new features of interest such as fibrosis density and pulmonary sleeve length have not yet been investigated

5.2.4 Improved Modeling Protocol

The OCT imaging data was wrapped to a single, representative atrial mesh with minor changes to its anatomy. In reality, different left atria are of different sizes and morphology, including varying orientation of pulmonary veins. Therefore, for more accurate mapping, it would be useful to obtain a personalized mesh of left atrial anatomy for each specimen, such as could be acquired from MRI or CT. This would enable more accurate registration, improved interpretation and personalization of the tissue structure imaged by OCT.

Additionally, combined with changes in the imaging protocol to improve imaging depth, modeling can be carried out in larger regions of cardiac tissue to better simulate arrhythmia dynamics. It is possible that a new modeling scheme would be required to more appropriately balance the tradeoff between computational burden and structural detail, as well as optimize model properties for tissues that have not before been incorporated in cardiac modeling. It will also be necessary to compare the results of the models to real optical mapping data to provide validation of the simulated results and extract further conclusions on structure-function relationships.

5.2.5 OCT-Integrated Catheters

In an *in vivo* setting, further challenges will occur due to heart motion, presence of blood, and requirements for faster data acquisition. However, OCT-integrated catheters have already been developed and tested *in vivo*, and were shown to be able to identify tissue microstructure such as the endocardium and tears within the myocardium, showing great promise towards the goal of

OCT-guided ablation procedures [113] Registration of OCT imaging to an anatomical mesh in real time, such as is done with current electroanatomic mapping technologies, would also be useful to incorporate OCT imaging into current clinical practice and requires further investigation.

Bibliography

[1]   C. R. Wyndham, "Atrial fibrillation: the most common arrhythmia," *Tex Heart Inst J,* vol. 27, pp. 257-67, 2000.

[2]   S. S. Chugh, R. Havmoeller, K. Narayanan, D. Singh, M. Rienstra, E. J. Benjamin*, et al.*, "Worldwide Epidemiology of Atrial Fibrillation: A Global Burden of Disease 2010 Study," *Circulation,* vol. 129, pp. 837-847, 12/17 2014.

[3]   P. A. Wolf, R. D. Abbott, and W. B. Kannel, "Atrial fibrillation as an independent risk factor for stroke: the Framingham Study," *Stroke,* vol. 22, pp. 983-8, Aug 1991.

[4]   E. J. Benjamin, P. A. Wolf, R. B. D'Agostino, H. Silbershatz, W. B. Kannel, and D. Levy, "Impact of Atrial Fibrillation on the Risk of Death," *The Framingham Heart Study,* vol. 98, pp. 946-952, 1998.

[5]   M. H. Kim, S. S. Johnston, B.-C. Chu, M. R. Dalal, and K. L. Schulman, "Estimation of Total Incremental Health Care Costs in Patients With Atrial Fibrillation in the United States," *Circulation: Cardiovascular Quality and Outcomes,* vol. 4, pp. 313-320, 2011.

[6]   Y. Miyasaka, M. E. Barnes, B. J. Gersh, S. S. Cha, K. R. Bailey, W. P. Abhayaratna*, et al.*, "Secular trends in incidence of atrial fibrillation in Olmsted County, Minnesota, 1980 to 2000, and implications on the projections for future prevalence," *Circulation,* vol. 114, pp. 119-125, 2006.

[7]   A. S. Go, E. M. Hylek, K. A. Phillips, Y. Chang, L. E. Henault, J. V. Selby*, et al.*, "Prevalence of diagnosed atrial fibrillation in adults: national implications for rhythm management and stroke prevention: the AnTicoagulation and Risk Factors in Atrial Fibrillation (ATRIA) Study," *Jama,* vol. 285, pp. 2370-5, May 9 2001.

[8]   S. Nattel, B. Burstein, and D. Dobrev, "Atrial Remodeling and Atrial Fibrillation: Mechanisms and Implications," *Circulation: Arrhythmia and Electrophysiology,* vol. 1, pp. 62-73, April 1, 2008 2008.

[9]   G. K. Moe and J. A. Abildskov, "Atrial fibrillation as a self-sustaining arrhythmia independent of focal discharge," *Am Heart J,* vol. 58, pp. 59-70, Jul 1959.

[10]   T. Lewis, "Oliver-Sharpey Lectures ON THE NATURE OF FLUTTER AND FIBRILLATION OF THE AURICLE," *British Medical Journal,* vol. 1, pp. 551-555, 1921.

[11]   T. Kurotobi, K. Iwakura, K. Inoue, R. Kimura, A. Okamura, Y. Koyama*, et al.*, "Multiple arrhythmogenic foci associated with the development of perpetuation of atrial fibrillation," *Circ Arrhythm Electrophysiol,* vol. 3, pp. 39-45, Feb 2010.

[12]   J. Jalife, "Rotors and spiral waves in atrial fibrillation," *J Cardiovasc Electrophysiol,* vol. 14, pp. 776-80, Jul 2003.

[13]   J. Eckstein, B. Maesen, D. Linz, S. Zeemering, A. van Hunnik, S. Verheule*, et al.*, "Time course and mechanisms of endo-epicardial electrical dissociation during atrial fibrillation in the goat," *Cardiovasc Res,* vol. 89, pp. 816-24, Mar 1 2011.

[14]   B. J. Hansen, J. Zhao, T. A. Csepe, B. T. Moore, N. Li, L. A. Jayne*, et al.*, "Atrial fibrillation driven by micro-anatomic intramural re-entry revealed by simultaneous sub-epicardial and sub-endocardial optical mapping in explanted human hearts," *European Heart Journal,* 2015-06-09 00:00:00 2015.

[15]   J. Zhao, B. J. Hansen, T. A. Csepe, P. Lim, Y. Wang, M. Williams*, et al.*, "Integration of High-Resolution Optical Mapping and 3-Dimensional Micro-Computed Tomographic Imaging to Resolve the Structural Basis of Atrial Conduction in the Human Heart,"

Circulation: Arrhythmia and Electrophysiology, vol. 8, pp. 1514-1517, December 1, 2015 2015.

[16] B. Maesen, S. Zeemering, C. Afonso, J. Eckstein, R. A. Burton, A. van Hunnik*, et al.*, "Rearrangement of atrial bundle architecture and consequent changes in anisotropy of conduction constitute the 3-dimensional substrate for atrial fibrillation," *Circ Arrhythm Electrophysiol,* vol. 6, pp. 967-75, Oct 2013.

[17] M. Haissaguerre, A. J. Shah, H. Cochet, M. Hocini, R. Dubois, I. Efimov*, et al.*, "Intermittent drivers anchoring to structural heterogeneities as a major pathophysiological mechanism of human persistent atrial fibrillation," *Journal of Physiology,* vol. 594, pp. 2387-2398, 2016.

[18] S. N. Hatem and P. Sanders, "Epicardial adipose tissue and atrial fibrillation," *Cardiovascular Research,* vol. 102, pp. 205-213, 2014-05-01 00:00:00 2014.

[19] C. T. January, L. S. Wann, J. S. Alpert, H. Calkins, J. E. Cigarroa, J. J. C. Cleveland*, et al.*, "2014 AHA/ACC/HRS Guideline for the Management of Patients With Atrial Fibrillation: Executive SummaryA Report of the American College of Cardiology/American Heart Association Task Force on Practice Guidelines and the Heart Rhythm Society," *Journal of the American College of Cardiology,* vol. 64, pp. 2246-2280, 2014.

[20] T. M. Sundt, C. J. Camillo, and J. L. Cox, "THE MAZE PROCEDURE FOR CURE OF ATRIAL FIBRILLATION," *Cardiology Clinics,* vol. 15, pp. 739-748, 1997/11/01/ 1997.

[21] V. C. Babaliaros, J. T. Green, S. Lerakis, M. Lloyd, and P. C. Block, "Emerging applications for transseptal left heart catheterization old techniques for new procedures," *J Am Coll Cardiol,* vol. 51, pp. 2116-22, Jun 3 2008.

[22] N. F. Marrouche, D. O. Martin, O. Wazni, A. M. Gillinov, A. Klein, M. Bhargava*, et al.*, "Phased-array intracardiac echocardiography monitoring during pulmonary vein isolation in patients with atrial fibrillation: impact on outcome and complications," *Circulation,* vol. 107, pp. 2710-6, Jun 3 2003.

[23] M. J. Earley, "How to perform a transseptal puncture," *Heart,* vol. 95, pp. 85-92, Jan 2009.

[24] M. Haïssaguerre , P. Jaïs , D. C. Shah , A. Takahashi , M. Hocini , G. Quiniou *, et al.*, "Spontaneous Initiation of Atrial Fibrillation by Ectopic Beats Originating in the Pulmonary Veins," *New England Journal of Medicine,* vol. 339, pp. 659-666, 1998.

[25] R. Proietti, P. Santangeli, L. Di Biase, J. Joza, M. L. Bernier, Y. Wang*, et al.*, "Comparative effectiveness of wide antral versus ostial pulmonary vein isolation: a systematic review and meta-analysis," *Circ Arrhythm Electrophysiol,* vol. 7, pp. 39-45, Feb 2014.

[26] I. M. Robbins, E. V. Colvin, T. P. Doyle, W. E. Kemp, J. E. Loyd, W. S. McMahon*, et al.*, "Pulmonary Vein Stenosis After Catheter Ablation of Atrial Fibrillation," *Circulation,* vol. 98, pp. 1769-1775, 1998.

[27] C. Pappone, S. Rosanio, G. Oreto, M. Tocchi, F. Gugliotta, G. Vicedomini*, et al.*, "Circumferential radiofrequency ablation of pulmonary vein ostia: A new anatomic approach for curing atrial fibrillation," *Circulation,* vol. 102, pp. 2619-28, Nov 21 2000.

[28] D. Bhakta and J. M. Miller, "Principles of electroanatomic mapping," *Indian pacing and electrophysiology journal,* vol. 8, pp. 32-50, 2008.

[29] B. D. Powell and D. L. Packer, "Does image integration improve atrial fibrillation ablation outcomes, or are other aspects of the ablation the key to success?," *Europace,* vol. 11, pp. 973-4, Aug 2009.

[30] A. Kolandaivelu, "Role of Cardiac Imaging (CT/MR) Before and After RF Catheter Ablation in Patients with Atrial Fibrillation," *Journal of atrial fibrillation,* vol. 5, pp. 523-523, 2012.

[31] S. Knecht, M. Hocini, M. Wright, N. Lellouche, M. D. O'Neill, S. Matsuo*, et al.*, "Left atrial linear lesions are required for successful treatment of persistent atrial fibrillation," *Eur Heart J,* vol. 29, pp. 2359-66, Oct 2008.

[32] A. Verma, C.-y. Jiang, T. R. Betts, J. Chen, I. Deisenhofer, R. Mantovan*, et al.*, "Approaches to Catheter Ablation for Persistent Atrial Fibrillation," *New England Journal of Medicine,* vol. 372, pp. 1812-1822, 2015/05/07 2015.

[33] J. Vogler, S. Willems, A. Sultan, D. Schreiber, J. Lüker, H. Servatius*, et al.*, "Pulmonary Vein Isolation Versus DefragmentationThe CHASE-AF Clinical Trial," *Journal of the American College of Cardiology,* vol. 66, pp. 2743-2752, 2015.

[34] R. Latchamsetty and A. G. Kocheril, "Review of Dominant Frequency Analysis in Atrial Fibrillation," *Journal of atrial fibrillation,* vol. 2, pp. 204-204, 2009.

[35] K. Nademanee, J. McKenzie, E. Kosar, M. Schwab, B. Sunsaneewitayakul, T. Vasavakul*, et al.*, "A new approach for catheter ablation of atrial fibrillation: mapping of the electrophysiologic substrate," *J Am Coll Cardiol,* vol. 43, pp. 2044-53, Jun 2 2004.

[36] D. Katritsis, F. M. Merchant, T. Mela, J. P. Singh, E. K. Heist, and A. A. Armoundas, "Catheter ablation of atrial fibrillation the search for substrate-driven end points," *J Am Coll Cardiol,* vol. 55, pp. 2293-8, May 25 2010.

[37] F. Atienza, J. Almendral, J. M. Ormaetxe, Á. Moya, J. D. Martínez-Alday, A. Hernández-Madrid*, et al.*, "Comparison of Radiofrequency Catheter Ablation of Drivers and Circumferential Pulmonary Vein Isolation in Atrial Fibrillation: A Noninferiority Randomized Multicenter RADAR-AF Trial," *Journal of the American College of Cardiology,* vol. 64, pp. 2455-2467, 2014/12/16/ 2014.

[38] H. Calkins, G. Hindricks, R. Cappato, Y. H. Kim, E. B. Saad, L. Aguinaga*, et al.*, "2017 HRS/EHRA/ECAS/APHRS/SOLAECE expert consensus statement on catheter and surgical ablation of atrial fibrillation," *Heart Rhythm,* vol. 14, pp. e275-e444, Oct 2017.

[39] B. J. Hansen, J. Zhao, and V. V. Fedorov, "Fibrosis and Atrial Fibrillation: Computerized and Optical Mapping: A View Into the Human Atria at Submillimeter Resolution," *JACC: Clinical Electrophysiology,* vol. 3, pp. 531-546, 2017.

[40] H. Kottkamp, J. Berg, R. Bender, A. Rieger, and D. Schreiber, "Box Isolation of Fibrotic Areas (BIFA): A Patient-Tailored Substrate Modification Approach for Ablation of Atrial Fibrillation," *J Cardiovasc Electrophysiol,* vol. 27, pp. 22-30, Jan 2016.

[41] R. S. Oakes, T. J. Badger, E. G. Kholmovski, N. Akoum, N. S. Burgon, E. N. Fish*, et al.*, "Detection and quantification of left atrial structural remodeling with delayed-enhancement magnetic resonance imaging in patients with atrial fibrillation," *Circulation,* vol. 119, pp. 1758-1767, 2009.

[42] N. F. Marrouche, D. Wilber, G. Hindricks, P. Jais, N. Akoum, F. Marchlinski*, et al.*, "Association of atrial tissue fibrosis identified by delayed enhancement MRI and atrial fibrillation catheter ablation: the DECAAF study," *Jama,* vol. 311, pp. 498-506, Feb 5 2014.

[43] D. E. Krummen, V. Swarup, and S. M. Narayan, "The role of rotors in atrial fibrillation," *Journal of thoracic disease,* vol. 7, pp. 142-151, 2015.

[44] S. M. Narayan, D. E. Krummen, and W.-J. Rappel, "Clinical mapping approach to diagnose electrical rotors and focal impulse sources for human atrial fibrillation," *Journal of cardiovascular electrophysiology,* vol. 23, pp. 447-454, 2012.

[45] M. Rodrigo, M. S. Guillem, A. M. Climent, J. Pedrón-Torrecilla, A. Liberos, J. Millet*, et al.*, "Body surface localization of left and right atrial high-frequency rotors in atrial fibrillation patients: a clinical-computational study," *Heart rhythm,* vol. 11, pp. 1584-1591, 2014.

[46] A. N. Ganesan, N. J. Shipp, A. G. Brooks, P. Kuklik, D. H. Lau, H. S. Lim*, et al.*, "Long-term outcomes of catheter ablation of atrial fibrillation: a systematic review and meta-analysis," *J Am Heart Assoc,* vol. 2, p. e004549, Apr 2013.

[47] G. J. Wynn, M. El-Kadri, I. Haq, M. Das, S. Modi, R. Snowdon*, et al.*, "Long-term outcomes after ablation of persistent atrial fibrillation: an observational study over 6 years," *Open Heart,* vol. 3, p. e000394, 2016.

[48] S. M. Narayan, M. Wright, N. Derval, A. Jadidi, A. Forclaz, I. Nault*, et al.*, "Classifying fractionated electrograms in human atrial fibrillation using monophasic action potentials and activation mapping: Evidence for localized drivers, rate acceleration, and nonlocal signal etiologies," *Heart Rhythm,* vol. 8, pp. 244-253, 2011.

[49] P. I. Gardner, P. C. Ursell, J. J. Fenoglio, and A. L. Wit, "Electrophysiologic and anatomic basis for fractionated electrograms recorded from healed myocardial infarcts," *Circulation,* vol. 72, pp. 596-611, 1985/09/01 1985.

[50] B. J. Hansen, J. Zhao, and V. V. Fedorov, "Fibrosis and Atrial Fibrillation: Computerized and Optical Mapping," *A View Into the Human Atria at Submillimeter Resolution,* vol. 3, pp. 531-546, 2017.

[51] J. Freudenberg, T. Schiemann, U. Tiede, and K. H. Hohne, "Simulation of cardiac excitation patterns in a three-dimensional anatomical heart atlas," *Comput Biol Med,* vol. 30, pp. 191-205, Jul 2000.

[52] G. Seemann, C. Hoper, F. B. Sachse, O. Dossel, A. V. Holden, and H. Zhang, "Heterogeneous three-dimensional anatomical and electrophysiological model of human atria," *Philos Trans A Math Phys Eng Sci,* vol. 364, pp. 1465-81, Jun 15 2006.

[53] J. Zhao, T. D. Butters, H. Zhang, A. J. Pullan, I. J. LeGrice, G. B. Sands*, et al.*, "An image-based model of atrial muscular architecture effects of structural anisotropy on electrical activation," *Circulation: Arrhythmia and Electrophysiology,* vol. 5, pp. 361-370, 2012.

[54] K. S. McDowell, F. Vadakkumpadan, R. Blake, J. Blauer, G. Plank, R. S. MacLeod*, et al.*, "Methodology for patient-specific modeling of atrial fibrosis as a substrate for atrial fibrillation," *J Electrocardiol,* vol. 45, pp. 640-5, Nov-Dec 2012.

[55] M. W. Krueger, G. Seemann, K. Rhode, D. U. Keller, C. Schilling, A. Arujuna*, et al.*, "Personalization of atrial anatomy and electrophysiology as a basis for clinical modeling of radio-frequency ablation of atrial fibrillation," *IEEE Trans Med Imaging,* vol. 32, pp. 73-84, Jan 2013.

[56] M. J. Gonzales, K. P. Vincent, W. J. Rappel, S. M. Narayan, and A. D. McCulloch, "Structural contributions to fibrillatory rotors in a patient-derived computational model of the atria," *Europace,* vol. 16 Suppl 4, pp. iv3-iv10, Nov 2014.

[57] T. E. Fastl, C. Tobon-Gomez, A. Crozier, J. Whitaker, R. Rajani, K. P. McCarthy*, et al.*, "Personalized computational modeling of left atrial geometry and transmural myofiber architecture," *Med Image Anal,* vol. 47, pp. 180-190, Jul 2018.

[58] F. Pashakhanloo, D. A. Herzka, H. Ashikaga, S. Mori, N. Gai, D. A. Bluemke, *et al.*, "Myofiber Architecture of the Human Atria as Revealed by Submillimeter Diffusion Tensor Imaging," *Circ Arrhythm Electrophysiol,* vol. 9, p. e004133, Apr 2016.

[59] J. Zhao, B. J. Hansen, Y. Wang, T. A. Csepe, L. V. Sul, A. Tang, *et al.*, "Three-dimensional Integrated Functional, Structural, and Computational Mapping to Define the Structural "Fingerprints" of Heart-Specific Atrial Fibrillation Drivers in Human Heart Ex Vivo," *Journal of the American Heart Association,* vol. 6, 2017.

[60] O. V. Aslanidi, M. A. Colman, M. Varela, J. Zhao, B. H. Smaill, J. C. Hancox, *et al.*, "Heterogeneous and anisotropic integrative model of pulmonary veins: computational study of arrhythmogenic substrate for atrial fibrillation," *Interface Focus,* vol. 3, p. 20120069, Apr 6 2013.

[61] K. S. McDowell, S. Zahid, F. Vadakkumpadan, J. Blauer, R. S. MacLeod, and N. A. Trayanova, "Virtual electrophysiological study of atrial fibrillation in fibrotic remodeling," *PLoS One,* vol. 10, p. e0117110, 2015.

[62] S. Nakamori, M. Nezafat, L. H. Ngo, W. J. Manning, and R. Nezafat, "Left Atrial Epicardial Fat Volume Is Associated With Atrial Fibrillation: A Prospective Cardiovascular Magnetic Resonance 3D Dixon Study," *Journal of the American Heart Association,* vol. 7, p. e008232, 2018.

[63] L. Zhao, D. L. Harrop, A. C. T. Ng, and W. Y. S. Wang, "Epicardial Adipose Tissue Is Associated With Left Atrial Dysfunction in People Without Obstructive Coronary Artery Disease or Atrial Fibrillation," *Canadian Journal of Cardiology,* vol. 34, pp. 1019-1025, 2018.

[64] K. Bouazizi, A. Rahhal, S. Kusmia, M. Evin, C. Defrance, P. Cluzel, *et al.*, "Differentiation and quantification of fibrosis, fat and fatty fibrosis in human left atrial myocardium using ex vivo MRI," *PLOS ONE,* vol. 13, p. e0205104, 2018.

[65] L. G. Tereshchenko, P. Rizzi, N. Mewton, G. J. Volpe, S. Murthy, D. G. Strauss, *et al.*, "Infiltrated atrial fat characterizes underlying atrial fibrillation substrate in patients at risk as defined by the ARIC atrial fibrillation risk score," *International journal of cardiology,* vol. 172, pp. 196-201, 01/22 2014.

[66] C. J. McGann, E. G. Kholmovski, R. S. Oakes, J. J. Blauer, M. Daccarett, N. Segerson, *et al.*, "New magnetic resonance imaging-based method for defining the extent of left atrial wall injury after the ablation of atrial fibrillation," *J Am Coll Cardiol,* vol. 52, pp. 1263-71, Oct 7 2008.

[67] T. Zghaib, A. A. Malayeri, E. G. Ipek, M. Habibi, D. Huang, M. A. Balouch, *et al.*, "Visualization of acute edema in the left atrial myocardium after radiofrequency ablation: Application of a novel high-resolution 3-dimensional magnetic resonance imaging sequence," *Heart Rhythm,* 2018.

[68] J. A. Cabrera, D. Sanchez-Quintana, J. Farre, F. Navarro, J. M. Rubio, F. Cabestrero, *et al.*, "Ultrasonic characterization of the pulmonary venous wall: echographic and histological correlation," *Circulation,* vol. 106, pp. 968-73, Aug 20 2002.

[69] P. G. Guerra, B. Thibault, M. Dubuc, M. Talajic, D. Roy, J. Crépeau, *et al.*, "Identification of atrial tissue in pulmonary veins using intravascular ultrasound," *Journal of the American Society of Echocardiography,* vol. 16, pp. 982-987, 2003/09/01/ 2003.

[70] I. R. Efimov and T. N. Mazgalev, "High-resolution, three-dimensional fluorescent imaging reveals multilayer conduction pattern in the atrioventricular node," *Circulation,* vol. 98, pp. 54-7, Jul 7 1998.

124

[71]   C. J. Hyatt, S. F. Mironov, M. Wellner, O. Berenfeld, A. K. Popp, D. A. Weitz, *et al.*, "Synthesis of voltage-sensitive fluorescence signals from three-dimensional myocardial activation patterns," *Biophysical Journal,* vol. 85, pp. 2673-2683, 2003.

[72]   M. J. Bishop, B. Rodriguez, J. Eason, J. P. Whiteley, N. Trayanova, and D. J. Gavaghan, "Synthesis of voltage-sensitive optical signals: Application to panoramic optical mapping," *Biophysical Journal,* vol. 90, pp. 2938-2945, 2006.

[73]   M. J. Bishop, B. Rodriguez, N. Trayanova, and D. J. Gavaghan, "Inference of Intramural Wavefront Orientation from Optical Recordings in Realistic Whole-Heart Models," *Biophysical Journal,* vol. 91, pp. 3957-3958, 08/25 2006.

[74]   M. J. Bishop, D. J. Gavaghan, N. A. Trayanova, and B. Rodriguez, "Photon scattering effects in optical mapping of propagation and arrhythmogenesis in the heart," *J Electrocardiol,* vol. 40, pp. S75-80, Nov-Dec 2007.

[75]   M. J. Bishop, B. Rodriguez, F. Qu, I. R. Efimov, D. J. Gavaghan, and N. A. Trayanova, "The role of photon scattering in optical signal distortion during arrhythmia and defibrillation," *Biophysical Journal,* vol. 93, pp. 3714-3726, 2007.

[76]   M. J. Bishop and G. Plank, "Simulating photon scattering effects in structurally detailed ventricular models using a Monte Carlo approach," *Front Physiol,* vol. 5, p. 338, 2014.

[77]   D. Sánchez-Quintana, G. Pizarro, J. R. López-Mínguez, S. Y. Ho, and J. A. Cabrera, "Standardized Review of Atrial Anatomy for Cardiac Electrophysiologists," *Journal of Cardiovascular Translational Research,* vol. 6, pp. 124-144, April 01 2013.

[78]   S. R. Gutbrod, R. Walton, S. Gilbert, V. Meillet, P. Jaïs, M. Hocini, *et al.*, "Quantification of the transmural dynamics of atrial fibrillation by simultaneous endocardial and epicardial optical mapping in an acute sheep model," *Circulation. Arrhythmia and electrophysiology,* vol. 8, pp. 456-465, 2015.

[79]   S. Y. Ho, R. H. Anderson, and D. Sánchez-Quintana, "Atrial structure and fibres: Morphologic bases of atrial conduction," *Cardiovascular Research,* vol. 54, pp. 325-336, 2002.

[80]   D. Huang, E. A. Swanson, C. P. Lin, J. S. Schuman, W. G. Stinson, W. Chang, *et al.*, "Optical coherence tomography," *Science,* vol. 254, pp. 1178-81, Nov 22 1991.

[81]   J. G. Fujimoto, C. Pitris, S. A. Boppart, and M. E. Brezinski, "Optical coherence tomography: an emerging technology for biomedical imaging and optical biopsy," *Neoplasia,* vol. 2, pp. 9-25, Jan-Apr 2000.

[82]   A. Rollins, S. Yazdanfar, M. Kulkarni, R. Ung-Arunyawee, and J. Izatt, "In vivo video rate optical coherence tomography," *Opt Express,* vol. 3, pp. 219-29, Sep 14 1998.

[83]   C. W. Sun, Y. M. Wang, L. S. Lu, C. W. Lu, I. J. Hsu, M. T. Tsai, *et al.*, "Myocardial tissue characterization based on a polarization-sensitive optical coherence tomography system with an ultrashort pulsed laser," *J Biomed Opt,* vol. 11, p. 054016, Sep-Oct 2006.

[84]   M. Adhi and J. S. Duker, "Optical coherence tomography--current and future applications," *Current opinion in ophthalmology,* vol. 24, pp. 213-221, 2013.

[85]   T. Roleder, J. Jąkała, G. L. Kałuża, Ł. Partyka, K. Proniewska, E. Pociask, *et al.*, "The basics of intravascular optical coherence tomography," *Postepy w kardiologii interwencyjnej = Advances in interventional cardiology,* vol. 11, pp. 74-83, 2015.

[86]   J. Welzel, "Optical coherence tomography in dermatology: a review," *Skin Res Technol,* vol. 7, pp. 1-9, Feb 2001.

[87]   M. Kirillin, T. Motovilova, and N. Shakhova, "Optical coherence tomography in gynecology: a narrative review," *J Biomed Opt,* vol. 22, pp. 1-9, Dec 2017.

[88] M. A. Choma, M. V. Sarunic, C. Yang, and J. A. Izatt, "Sensitivity advantage of swept source and Fourier domain optical coherence tomography," *Optics Express,* vol. 11, pp. 2183-2189, 2003/09/08 2003.

[89] J. F. de Boer, B. Cense, B. H. Park, M. C. Pierce, G. J. Tearney, and B. E. Bouma, "Improved signal-to-noise ratio in spectral-domain compared with time-domain optical coherence tomography," *Optics Letters,* vol. 28, pp. 2067-2069, 2003/11/01 2003.

[90] R. Leitgeb, C. Hitzenberger, and A. Fercher, "Performance of fourier domain vs. time domain optical coherence tomography," *Opt Express,* vol. 11, pp. 889-94, Apr 21 2003.

[91] J. A. Izatt and M. A. Choma, "Theory of Optical Coherence Tomography," in *Optical Coherence Tomography: Technology and Applications*, W. Drexler and J. G. Fujimoto, Eds., ed Berlin, Heidelberg: Springer Berlin Heidelberg, 2008, pp. 47-72.

[92] C. P. Fleming, C. M. Ripplinger, B. Webb, I. R. Efimov, and A. M. Rollins, "Quantification of cardiac fiber orientation using optical coherence tomography," *J Biomed Opt,* vol. 13, p. 030505, May-Jun 2008.

[93] C. M. Ambrosi, V. V. Fedorov, R. B. Schuessler, A. M. Rollins, and I. R. Efimov, "Quantification of fiber orientation in the canine atrial pacemaker complex using optical coherence tomography," *J Biomed Opt,* vol. 17, p. 071309, Jul 2012.

[94] C. J. Goergen, H. Radhakrishnan, S. Sakadzic, E. T. Mandeville, E. H. Lo, D. E. Sosnovik*, et al.*, "Optical coherence tractography using intrinsic contrast," *Opt Lett,* vol. 37, pp. 3882-4, Sep 15 2012.

[95] Y. Gan and C. P. Fleming, "Extracting three-dimensional orientation and tractography of myofibers using optical coherence tomography," *Biomed Opt Express,* vol. 4, pp. 2150-65, 2013.

[96] C. J. Goergen, H. H. Chen, S. Sakadžić, V. J. Srinivasan, and D. E. Sosnovik, "Microstructural characterization of myocardial infarction with optical coherence tractography and two-photon microscopy," *Physiological Reports,* vol. 4, p. e12894, 2016.

[97] A. Castonguay, J. Lefebvre, P. Pouliot, P. Avti, M. Moeini, and F. Lesage, "Serial optical coherence scanning reveals an association between cardiac function and the heart architecture in the aging rodent heart," *Biomed Opt Express,* vol. 8, pp. 5027-5038, Nov 1 2017.

[98] Z. Li, Q. Tang, T. Dickfeld, and Y. Chen, "Depth-resolved mapping of muscular bundles in myocardium pulmonary junction using optical coherence tomography," *J Biomed Opt,* vol. 23, pp. 1-5, Jul 2018.

[99] C. Fan and G. Yao, "Imaging myocardial fiber orientation using polarization sensitive optical coherence tomography," *Biomed Opt Express,* vol. 4, pp. 460-5, Mar 1 2013.

[100] Y. Wang and G. Yao, "Optical tractography of the mouse heart using polarization-sensitive optical coherence tomography," *Biomedical Optics Express,* vol. 4, pp. 2540-2545, 2013/11/01 2013.

[101] Y. Wang, K. Zhang, N. B. Wasala, X. Yao, D. Duan, and G. Yao, "Histology validation of mapping depth-resolved cardiac fiber orientation in fresh mouse heart using optical polarization tractography," *Biomed Opt Express,* vol. 5, pp. 2843-55, Aug 1 2014.

[102] Y. Wang, K. Zhang, D. Duan, and G. Yao, "Heart structural remodeling in a mouse model of Duchenne cardiomyopathy revealed using optical polarization tractography [Invited]," *Biomedical Optics Express,* vol. 8, pp. 1271-1276, 2017/03/01 2017.

[103] Y. Wang, M. Ravanfar, K. Zhang, D. Duan, and G. Yao, "Automatic quantification of microscopic heart damage in a mouse model of Duchenne muscular dystrophy using optical polarization tractography," *Journal of Biophotonics,* vol. 11, p. e201700284, 2018.

[104] M. Cua, E. Lin, L. Lee, X. Sheng, K. S. Wong, G. F. Tibbits*, et al.*, "Morphological phenotyping of mouse hearts using optical coherence tomography," *J Biomed Opt,* vol. 19, p. 116007, 2014.

[105] M. Jenkins, R. S. Wade, Y. Cheng, A. M. Rollins, and I. R. Efimov, "Optical coherence tomography imaging of the purkinje network," *J Cardiovasc Electrophysiol,* vol. 16, pp. 559-60, May 2005.

[106] M. Gupta, A. M. Rollins, J. A. Izatt, and I. R. Efimov, "Imaging of the atrioventricular node using optical coherence tomography," *Journal of Cardiovascular Electrophysiology,* vol. 13, pp. 95-95, Jan 2002.

[107] W. J. Hucker, C. M. Ripplinger, C. P. Fleming, V. V. Fedorov, A. M. Rollins, and I. R. Efimov, "Bimodal biophotonic imaging of the structure-function relationship in cardiac tissue," *J Biomed Opt,* vol. 13, p. 054012, Sep-Oct 2008.

[108] S. Wang, A. L. Lopez, 3rd, Y. Morikawa, G. Tao, J. Li, I. V. Larina*, et al.*, "Noncontact quantitative biomechanical characterization of cardiac muscle using shear wave imaging optical coherence tomography," *Biomed Opt Express,* vol. 5, pp. 1980-92, Jul 1 2014.

[109] C. P. Fleming, K. J. Quan, and A. M. Rollins, "Toward guidance of epicardial cardiac radiofrequency ablation therapy using optical coherence tomography," *J Biomed Opt,* vol. 15, p. 041510, Jul-Aug 2010.

[110] C. P. Fleming, H. Wang, K. J. Quan, and A. M. Rollins, "Real-time monitoring of cardiac radio-frequency ablation lesion formation using an optical coherence tomography forward-imaging catheter," *J Biomed Opt,* vol. 15, p. 030516, May-Jun 2010.

[111] X. Fu, Z. Wang, H. Wang, Y. T. Wang, M. W. Jenkins, and A. M. Rollins, "Fiber-optic catheter-based polarization-sensitive OCT for radio-frequency ablation monitoring," *Optics Letters,* vol. 39, pp. 5066-5069, 2014/09/01 2014.

[112] X. Zhao, X. Fu, C. Blumenthal, Y. T. Wang, M. W. Jenkins, C. Snyder*, et al.*, "Integrated RFA/PSOCT catheter for real-time guidance of cardiac radio-frequency ablation," *Biomedical Optics Express,* vol. 9, pp. 6400-6411, 2018/12/01 2018.

[113] C. P. Fleming, N. Rosenthal, A. M. Rollins, and M. M. Arruda, "First in vivo Real-Time Imaging of Endocardial Radiofrequency Ablation by Optical Coherence Tomography: Implications on Safety and The Birth of ''Electro-structural'' Substrate-Guided Ablation," *Innovations in Cardiac Rhythm Management,* vol. 2, pp. 199-201, 2011.

[114] H. Wang, W. Kang, T. Carrigan, A. Bishop, N. Rosenthal, M. Arruda*, et al.*, "In vivo intracardiac optical coherence tomography imaging through percutaneous access: toward image-guided radio-frequency ablation," *Journal of Biomedical Optics,* vol. 16, p. 110505, Nov 2011.

[115] C. P. Fleming, K. J. Quan, H. Wang, G. Amit, and A. M. Rollins, "In vitro characterization of cardiac radiofrequency ablation lesions using optical coherence tomography," *Opt Express,* vol. 18, pp. 3079-92, Feb 1 2010.

[116] X. Yao, Y. Gan, Y. Ling, C. C. Marboe, and C. P. Hendon, "Multicontrast endomyocardial imaging by single-channel high-resolution cross-polarization optical coherence tomography," *J Biophotonics,* vol. 11, p. e201700204, Apr 2018.

[117] C. M. Ambrosi, N. Moazami, A. M. Rollins, and I. R. Efimov, "Virtual histology of the human heart using optical coherence tomography," 2009, p. 7.

[118] Y. Gan, D. Tsay, S. B. Amir, C. C. Marboe, and C. P. Hendon, "Automated classification of optical coherence tomography images of human atrial tissue," *J Biomed Opt,* vol. 21, p. 101407, Oct 2016.

[119] X. Yao, Y. Gan, C. C. Marboe, and C. P. Hendon, "Myocardial imaging using ultrahigh-resolution spectral domain optical coherence tomography," *Journal of Biomedical Optics,* vol. 21, pp. 061006-061006, 2016.

[120] J. Eckstein, S. Zeemering, D. Linz, B. Maesen, S. Verheule, A. van Hunnik*, et al.*, "Transmural conduction is the predominant mechanism of breakthrough during atrial fibrillation: evidence from simultaneous endo-epicardial high-density activation mapping," *Circ Arrhythm Electrophysiol,* vol. 6, pp. 334-41, Apr 2013.

[121] S. Y. Ho, D. Sanchez-Quintana, J. A. Cabrera, and R. H. Anderson, "Anatomy of the left atrium: implications for radiofrequency ablation of atrial fibrillation," *J Cardiovasc Electrophysiol,* vol. 10, pp. 1525-33, Nov 1999.

[122] H. Nathan and M. Eliakim, "The Junction Between the Left Atrium and the Pulmonary Veins: An Anatomic Study of Human Hearts," *Circulation,* vol. 34, pp. 412-422, 1966.

[123] K. Tanaka, S. Zlochiver, K. L. Vikstrom, M. Yamazaki, J. Moreno, M. Klos*, et al.*, "Spatial distribution of fibrosis governs fibrillation wave dynamics in the posterior left atrium during heart failure," *Circ Res,* vol. 101, pp. 839-47, Oct 12 2007.

[124] S. Verheule, E. Tuyls, A. Gharaviri, S. Hulsmans, A. van Hunnik, M. Kuiper*, et al.*, "Loss of continuity in the thin epicardial layer because of endomysial fibrosis increases the complexity of atrial fibrillatory conduction," *Circ Arrhythm Electrophysiol,* vol. 6, pp. 202-11, Feb 2013.

[125] N. Angel, L. Li, R. S. MacLeod, N. Marrouche, R. Ranjan, and D. J. Dosdall, "Diverse Fibrosis Architecture and Premature Stimulation Facilitate Initiation of Reentrant Activity Following Chronic Atrial Fibrillation," *Journal of Cardiovascular Electrophysiology,* vol. 26, pp. 1352-1360, 2015.

[126] H. M. Tsao, W. C. Hu, M. H. Wu, C. T. Tai, Y. J. Lin, S. L. Chang*, et al.*, "Quantitative analysis of quantity and distribution of epicardial adipose tissue surrounding the left atrium in patients with atrial fibrillation and effect of recurrence after ablation," *Am J Cardiol,* vol. 107, pp. 1498-503, May 15 2011.

[127] S. Ho, J. Cabrera, V. Tran, J. Farre, R. Anderson, and D. Sanchez-Quintana, "Architecture of the pulmonary veins: relevance to radiofrequency ablation," *Heart,* vol. 86, pp. 265-270, 2001.

[128] R. J. Hassink, H. T. Aretz, J. Ruskin, and D. Keane, "Morphology of atrial myocardium in human pulmonary veins: a postmortem analysis in patients with and without atrial fibrillation," *J Am Coll Cardiol,* vol. 42, pp. 1108-14, Sep 17 2003.

[129] S. Y. Ho, J. A. Cabrera, and D. Sanchez-Quintana, "Left Atrial Anatomy Revisited," *Circulation: Arrhythmia and Electrophysiology,* vol. 5, pp. 220-228, 2012.

[130] T. Saito, K. Waki, and A. E. Becker, "Left atrial myocardial extension onto pulmonary veins in humans: anatomic observations relevant for atrial arrhythmias," *J Cardiovasc Electrophysiol,* vol. 11, pp. 888-94, Aug 2000.

[131] S. S. Po, Y. Li, D. Tang, H. Liu, N. Geng, W. M. Jackman*, et al.*, "Rapid and stable re-entry within the pulmonary vein as a mechanism initiating paroxysmal atrial fibrillation," *J Am Coll Cardiol,* vol. 45, pp. 1871-7, Jun 7 2005.

[132] A. Hamabe, Y. Okuyama, Y. Miyauchi, S. Zhou, H. N. Pak, H. S. Karagueuzian*, et al.*, "Correlation between anatomy and electrical activation in canine pulmonary veins," *Circulation,* vol. 107, pp. 1550-5, Mar 25 2003.

[133] M. Hocini, S. Y. Ho, T. Kawara, A. C. Linnenbank, M. Potse, D. Shah*, et al.*, "Electrical conduction in canine pulmonary veins: electrophysiological and anatomic correlation," *Circulation,* vol. 105, pp. 2442-8, May 21 2002.

[134] N. Naqvi, K. P. McCarthy, and S. Y. Ho, "Anatomy of the atrial septum and interatrial communications," *Journal of thoracic disease,* vol. 10, pp. S2837-S2847, 2018.

[135] M. D. Radu, "The Clinical Atlas of Intravascular Optical Coherence Tomography for iPad," *Eur Heart J,* vol. 33, pp. 1174-5, May 2012.

[136] D. A. Landry, *Optical Coherence Tomography: A Clinical Atlas of Retinal Images*, 1 ed.: Bryson Taylor Publishing 2011.

[137] Y. Gan, W. Yao, K. M. Myers, J. Y. Vink, R. J. Wapner, and C. P. Hendon, "Analyzing three-dimensional ultrastructure of human cervical tissue using optical coherence tomography," *Biomedical Optics Express,* vol. 6, pp. 1090-1108, 2015/04/01 2015.

[138] J. R. Kremer, D. N. Mastronarde, and J. R. McIntosh, "Computer visualization of three-dimensional image data using IMOD," *J Struct Biol,* vol. 116, pp. 71-6, Jan-Feb 1996.

[139] M. J. Gonzales, G. Sturgeon, A. Krishnamurthy, J. Hake, R. Jonas, P. Stark*, et al.*, "A three-dimensional finite element model of human atrial anatomy: new methods for cubic Hermite meshes with extraordinary vertices," *Med Image Anal,* vol. 17, pp. 525-37, Jul 2013.

[140] C. Xu, J. M. Schmitt, S. G. Carlier, and R. Virmani, "Characterization of atherosclerosis plaques by measuring both backscattering and attenuation coefficients in optical coherence tomography," *J Biomed Opt,* vol. 13, p. 034003, May-Jun 2008.

[141] R. De Ponti, R. Cappato, A. Curnis, P. Della Bella, L. Padeletti, A. Raviele*, et al.*, "Trans-septal catheterization in the electrophysiology laboratory: data from a multicenter survey spanning 12 years," *J Am Coll Cardiol,* vol. 47, pp. 1037-42, Mar 7 2006.

[142] H. E. Lim, H. C. Park, J.-E. Ban, J.-I. Choi, S. W. Park, Y. M. Park*, et al.*, "Interatrial septal thickness is associated with the extent of left atrial complex fractionated atrial electrograms and acute procedural outcome in patients with persistent atrial fibrillation," *EP Europace,* vol. 17, pp. 1700-1707, 2015.

[143] W. Yao, Y. Gan, K. M. Myers, J. Y. Vink, R. J. Wapner, and C. P. Hendon, "Collagen Fiber Orientation and Dispersion in the Upper Cervix of Non-Pregnant and Pregnant Women," *PLOS ONE,* vol. 11, p. e0166709, 2016.

[144] J. Yan, J. K. Thomson, W. Zhao, V. G. Fast, T. Ye, and X. Ai, "Voltage and calcium dual channel optical mapping of cultured HL-1 atrial myocyte monolayer," *Journal of visualized experiments : JoVE,* p. 52542, 2015.

[145] C. J. Hyatt, S. F. Mironov, F. J. Vetter, C. W. Zemlin, and A. M. Pertsov, "Optical action potential upstroke morphology reveals near-surface transmural propagation direction," *Circulation Research,* vol. 97, pp. 277-284, 2005.

[146] C. Gloschat, K. Aras, S. Gupta, N. R. Faye, H. Zhang, R. A. Syunyaev*, et al.*, "RHYTHM: An Open Source Imaging Toolkit for Cardiac Panoramic Optical Mapping," *Scientific Reports,* vol. 8, p. 2921, 2018/02/13 2018.

[147] M. Attin and W. T. Clusin, "Basic concepts of optical mapping techniques in cardiac electrophysiology," *Biol Res Nurs,* vol. 11, pp. 195-207, Oct 2009.

[148] I. R. Efimov, V. P. Nikolski, and G. Salama, "Optical imaging of the heart," *Circ Res,* vol. 95, pp. 21-33, Jul 9 2004.

[149] J. I. Laughner, F. S. Ng, M. S. Sulkin, R. M. Arthur, and I. R. Efimov, "Processing and analysis of cardiac optical mapping data obtained with potentiometric dyes," *Am J Physiol Heart Circ Physiol,* vol. 303, pp. H753-65, Oct 1 2012.

[150] S. D. Girouard, K. R. Laurita, and D. S. Rosenbaum, "Unique properties of cardiac action potentials recorded with voltage-sensitive dyes," *J Cardiovasc Electrophysiol,* vol. 7, pp. 1024-38, Nov 1996.

[151] A. Pertsov, R. D. Walton, and O. Bernus, "Optical imaging of cardiac action potential," in *Membrane Potential Imaging in the Nervous System and Heart*, ed, 2015, pp. 299-311.

[152] I. R. Efimov, V. Sidorov, Y. Cheng, and B. Wollenzier, "Evidence of three-dimensional scroll waves with ribbon-shaped filament as a mechanism of ventricular tachycardia in the isolated rabbit heart," *J Cardiovasc Electrophysiol,* vol. 10, pp. 1452-62, Nov 1999.

[153] C. W. Zemlin, O. Bernus, A. Matiukas, C. J. Hyatt, and A. M. Pertsov, "Extracting intramural wavefront orientation from optical upstroke shapes in whole hearts," *Biophysical Journal,* vol. 95, pp. 942-950, 2008.

[154] C. J. Hyatt, C. W. Zemlin, R. M. Smith, A. Matiukas, A. M. Pertsov, and O. Bernus, "Reconstructing subsurface electrical wave orientation from cardiac epi-fluorescence recordings: Monte Carlo versus diffusion approximation," *Optics Express,* vol. 16, pp. 13758-13772, 2008.

[155] F. H. Wittkampf, R. N. Hauer, and E. O. Robles de Medina, "Control of radiofrequency lesion size by power regulation," *Circulation,* vol. 80, pp. 962-8, Oct 1989.

[156] K. P. Vincent, M. J. Gonzales, A. K. Gillette, C. T. Villongco, S. Pezzuto, J. H. Omens*, et al.*, "High-order finite element methods for cardiac monodomain simulations," *Front Physiol,* vol. 6, p. 217, 2015.

[157] H. Shen and G. Wang, "A study on tetrahedron-based inhomogeneous Monte Carlo optical simulation," *Biomed Opt Express,* vol. 2, pp. 44-57, Dec 3 2010.

[158] Q. Fang and D. A. Boas, "Tetrahedral mesh generation from volumetric binary and grayscale images," in *Biomedical Imaging: From Nano to Macro, 2009. ISBI '09. IEEE International Symposium on*, 2009, pp. 1142-1145.

[159] M. J. Bishop and G. Plank, "Biophotonic modelling of cardiac optical imaging," in *Advances in Experimental Medicine and Biology* vol. 859, ed, 2015, pp. 367-404.

[160] F. Fenton and A. Karma, "Vortex dynamics in three-dimensional continuous myocardium with fiber rotation: Filament instability and fibrillation," *Chaos,* vol. 8, pp. 20-47, Mar 1998.

[161] A. M. Goodman, R. A. Oliver, C. S. Henriquez, and P. D. Wolf, "A membrane model of electrically remodelled atrial myocardium derived from in vivo measurements," *Europace,* vol. 7 Suppl 2, pp. 135-45, Sep 2005.

[162] O. Bernus, K. S. Mukund, and A. M. Pertsov, "Detection of intramyocardial scroll waves using absorptive transillumination imaging," *J Biomed Opt,* vol. 12, p. 014035, Jan-Feb 2007.

[163] K. C. Roberts-Thomson, I. Stevenson, P. M. Kistler, H. M. Haqqani, S. J. Spence, J. C. Goldblatt*, et al.*, "The role of chronic atrial stretch and atrial fibrillation on posterior left atrial wall conduction," *Heart Rhythm,* vol. 6, pp. 1109-17, Aug 2009.

[164] M. M. Rahme, B. Cotter, E. Leistad, M. K. Wadhwa, R. Mohabir, A. P. Ford*, et al.*, "Electrophysiological and antiarrhythmic effects of the atrial selective 5-HT(4) receptor antagonist RS-100302 in experimental atrial flutter and fibrillation," *Circulation,* vol. 100, pp. 2010-7, Nov 9 1999.

[165] P. Kovoor, M. Daly, M. Mikhail, V. Eipper, B. Dewsnap, and D. L. Ross, "Change in size of lesions over 3 weeks after radiofrequency ablation of left ventricle," *J Cardiovasc Electrophysiol,* vol. 17, pp. 411-4, Apr 2006.

[166] I. Meglinski and A. Doronin, "Monte Carlo Modeling of Photon Migration for the Needs of Biomedical Optics and Biophotonics," ed, 2012, pp. 1-72.

[167] S. L. Jacques, "Optical properties of biological tissues: a review," *Phys Med Biol,* vol. 58, pp. R37-61, Jun 7 2013.

[168] G. J. Tearney, M. E. Brezinski, J. F. Southern, B. E. Bouma, M. R. Hee, and J. G. Fujimoto, "Determination of the refractive index of highly scattering human tissue by optical coherence tomography," *Optics Letters,* vol. 20, pp. 2258-2260, 1995/11/01 1995.

[169] R. K. Wang and V. V. Tuchin, *Advanced Biophotonics: Tissue Optical Sectioning*. Boca Raton, FL: CRC Press, 2016.

[170] R. P. Singh-Moon, C. C. Marboe, and C. P. Hendon, "Near-infrared spectroscopy integrated catheter for characterization of myocardial tissues: preliminary demonstrations to radiofrequency ablation therapy for atrial fibrillation," *Biomedical Optics Express,* vol. 6, pp. 2494-2511, 2015/07/01 2015.

[171] A. N. Bashkatov, E. A. Genina, V. I. Kochubey, and V. V. Tuchin, "Optical properties of human skin, subcutaneous and mucous tissues in the wavelength range from 400 to 2000 nm," *Journal of Physics D: Applied Physics,* vol. 38, pp. 2543-2555, 2005/07/22 2005.

[172] L. Ding, R. Splinter, and S. B. Knisley, "Quantifying spatial localization of optical mapping using Monte Carlo simulations," *IEEE Trans Biomed Eng,* vol. 48, pp. 1098-107, Oct 2001.

[173] R. D. Walton, R. M. Smith, B. G. Mitrea, E. White, O. Bernus, and A. M. Pertsov, "Extracting surface activation time from the optically recorded action potential in three-dimensional myocardium," *Biophysical Journal,* vol. 102, pp. 30-38, 2012.

[174] M. Mercader, L. Swift, S. Sood, H. Asfour, M. Kay, and N. Sarvazyan, "Use of endogenous NADH fluorescence for real-time in situ visualization of epicardial radiofrequency ablation lesions and gaps," *American Journal of Physiology - Heart and Circulatory Physiology,* vol. 302, pp. H2131-H2138, 2012.

[175] T. Staudt, M. C. Lang, R. Medda, J. Engelhardt, and S. W. Hell, "2,2′-Thiodiethanol: A new water soluble mounting medium for high resolution optical microscopy," *Microscopy Research and Technique,* vol. 70, pp. 1-9, 2007.

[176] Y. Ling, X. Yao, and C. P. Hendon, "Highly phase-stable 200 kHz swept-source optical coherence tomography based on KTN electro-optic deflector," *Biomedical Optics Express,* vol. 8, pp. 3687-3699, 2017/08/01 2017.

[177] X. Yao, Y. Gan, E. Chang, H. Hibshoosh, S. Feldman, and C. Hendon, "Visualization and tissue classification of human breast cancer images using ultrahigh-resolution OCT," *Lasers Surg Med,* vol. 49, pp. 258-269, Mar 2017.

Appendix

Optical Coherence Tomography Cardiac Atlas: Interpretation Guidelines

1. Categories

(**1**) *Endocardium*: Always the uppermost tissue layer. Seen as blue or purple in histology and typically is the brightest layer within OCT. Thickness can vary greatly, but can be extremely thin in the ventricles. May appear to have multiple layers due to varying compositions of connective tissue.
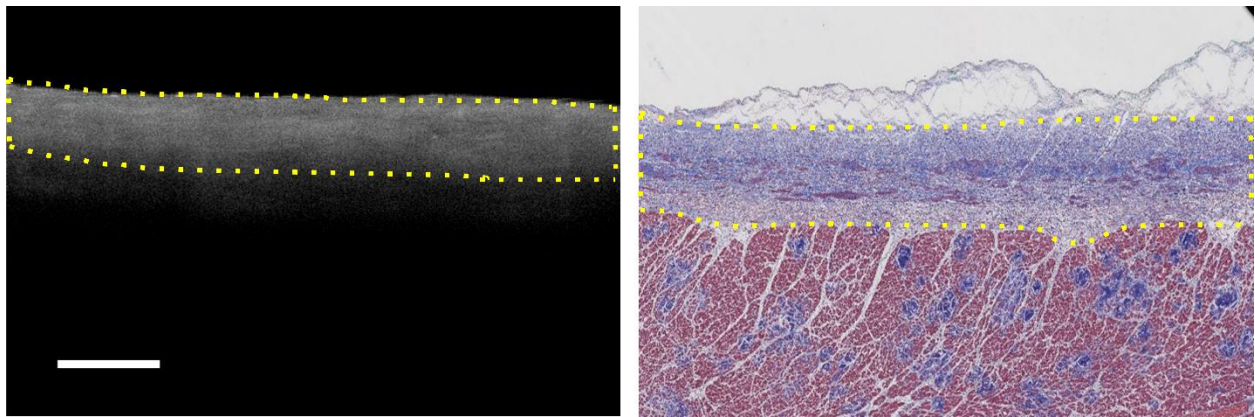
(**2**) *Myocardium*: Always below the endocardium (unless endocardial layer is absent). Seen as red in histology and is typically a darker grey in OCT. Note that if the endocardium is very thick, the myocardium may not be visible due to limited penetration depth.
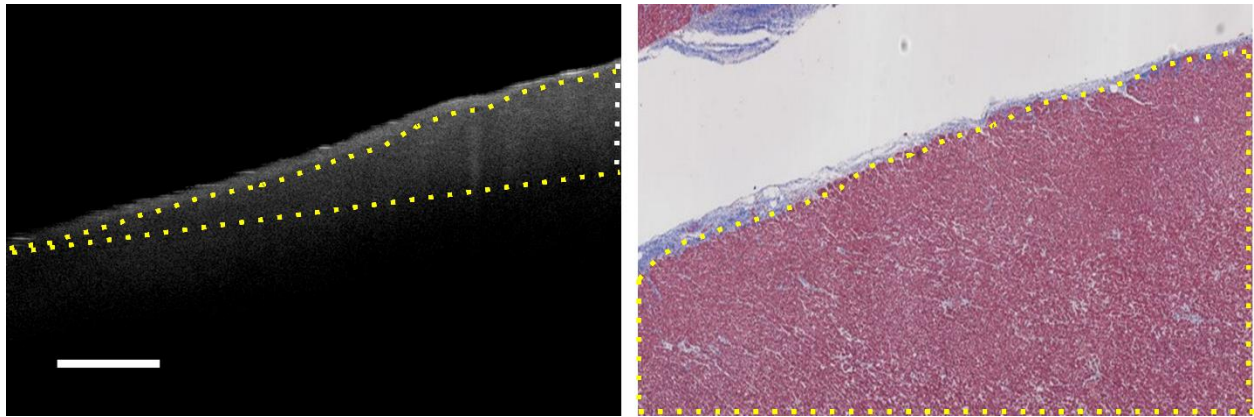
(3-6) *Fibrotic Myocardium*: Myocardium with collagen content. Seen as red myocardium with blue collagen in histology. Corresponding OCT features can vary. In some cases, the OCT region may contain heterogeneous variations in intensity (like below). In other cases, there may be no particular features that look like fibrosis in OCT (i.e. just looks like normal myocardium), but regardless should be labeled as fibrosis if histology shows a significant amount of it. If the fibrotic region is minor and does not cover the majority of the region, simply label as myocardium.
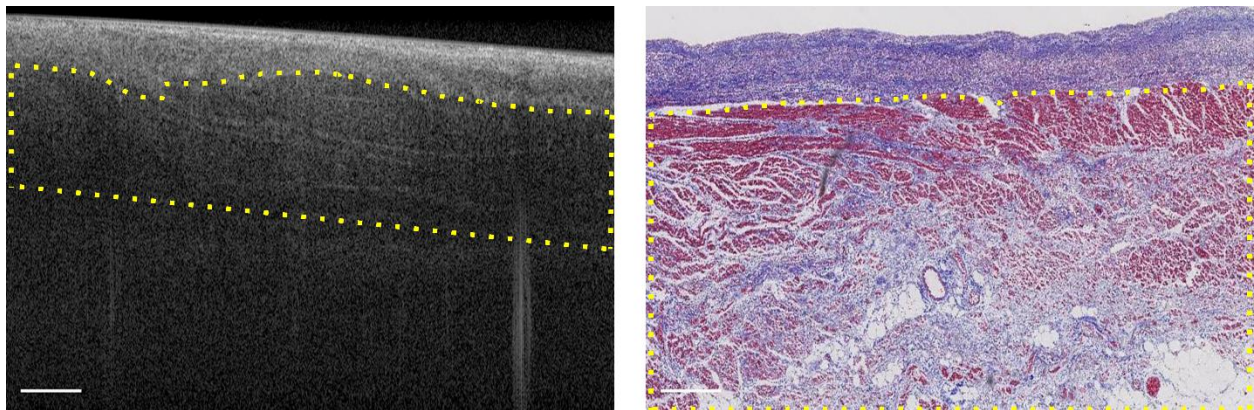

(7) *Adipose*: Seen as white in histology, and as a speckled or "honeycomb" pattern in OCT. Note that depending on the depth at which adipose tissue is located, adipose tissue may have a clear "honeycomb" structure in OCT (top example), or may have a more spotted appearance that becomes increasingly vague the deeper in the tissue it is located (bottom examples). The location

of adipose seen in OCT may not correspond exactly to that seen in histology, but it should be relatively clear to identify adipose in OCT based on its unique texture.
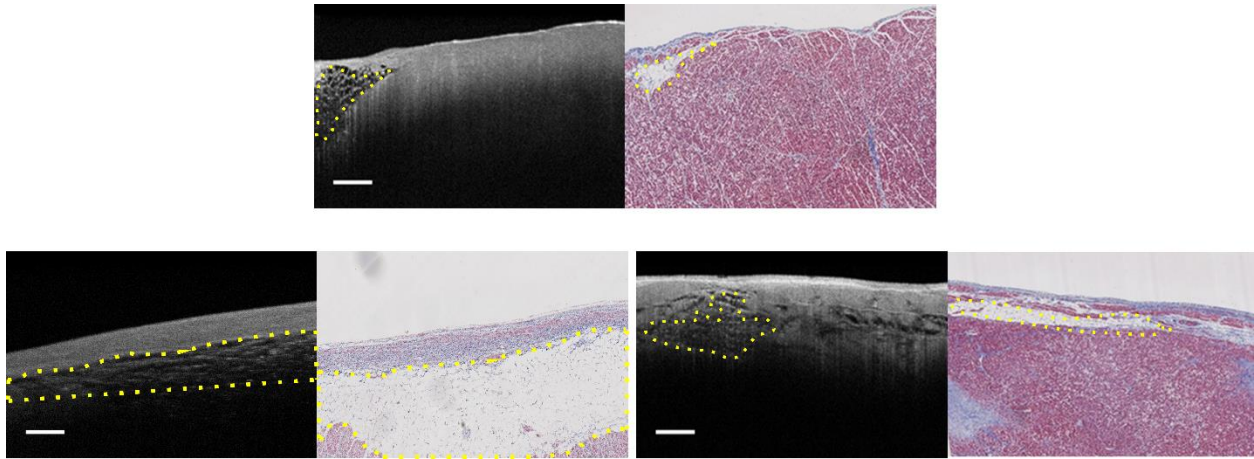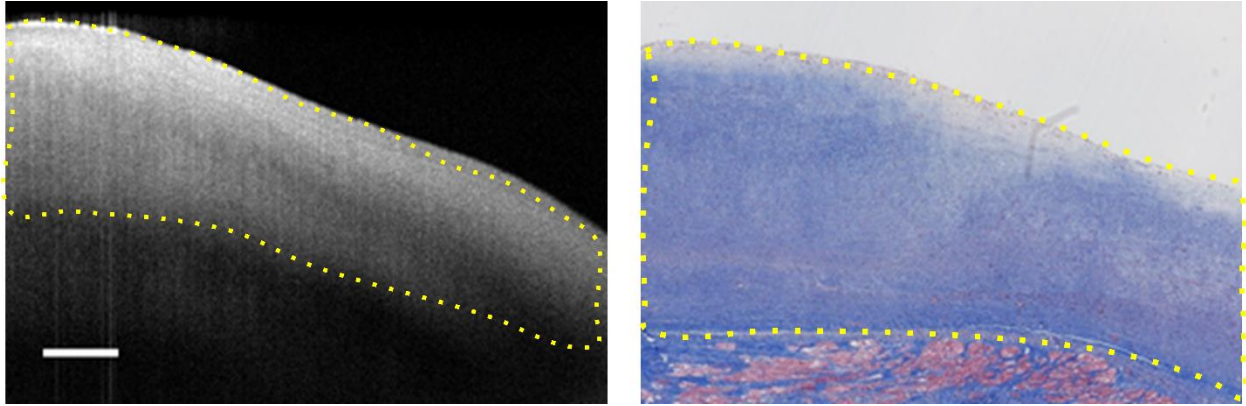

(8) *Right-Side Endocardium at Septum*

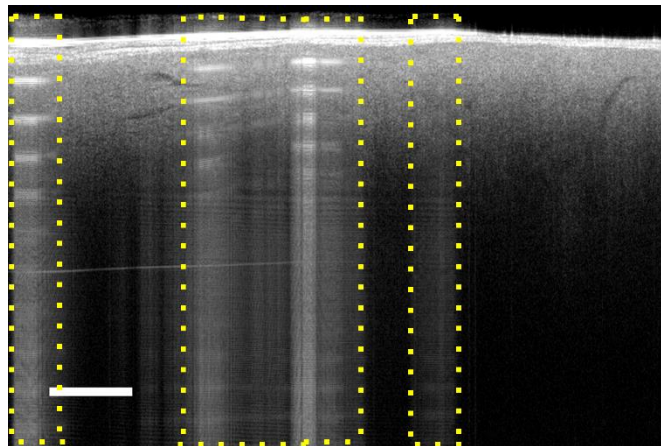A lower wall similar to the endocardium seen in certain areas of the left atrium.
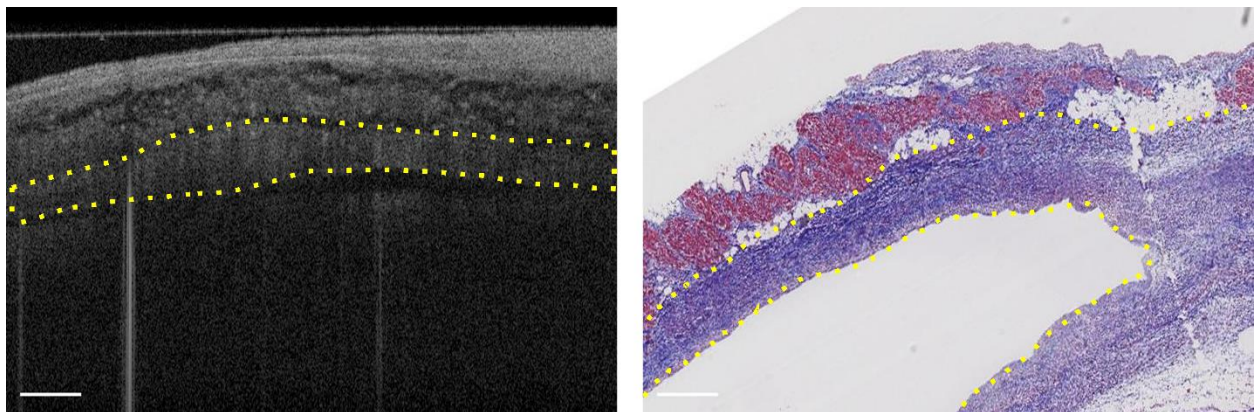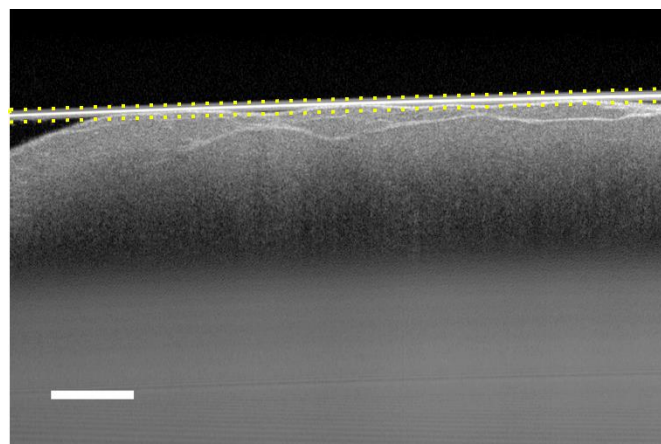

(9) *Endocardial Scar/Thickening*

Significantly thicker endocardium, especially in the ventricles
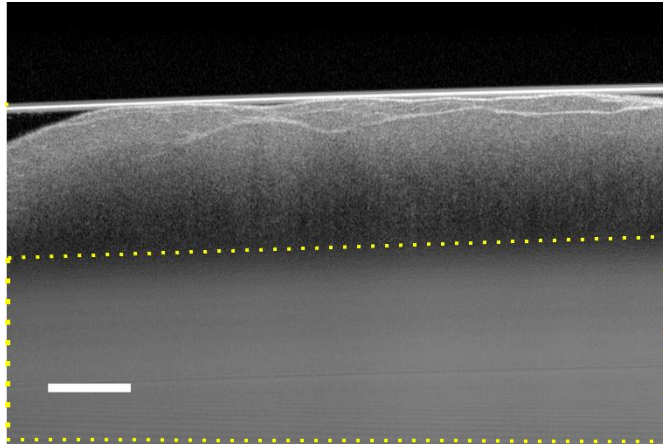
(10) *Saturation Artifact*: Caused by an over-reflective surface. Appears as vertical stripes.
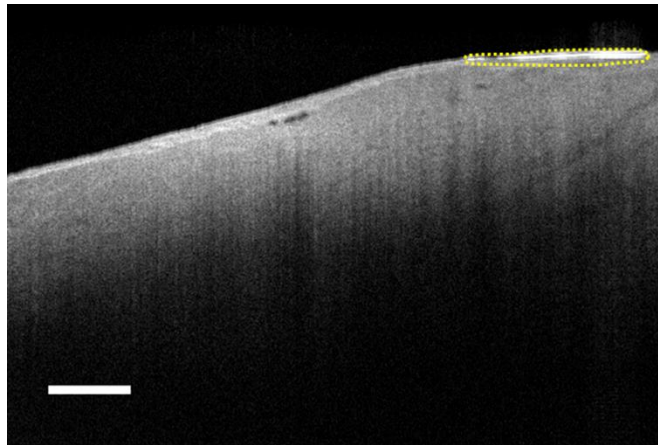

(11) *Immersion Lens*: A thin line in the OCT image that comes from the lens used during imaging for certain volumes. It is always a straight line.


135

(12) *Autocorrelation Artifact*: Artifact produced by the lens. Always seen at the bottom of the image as a smooth grey region.

(13) *Reflection Artifact*: Area of high reflection caused by water or a wet surface.
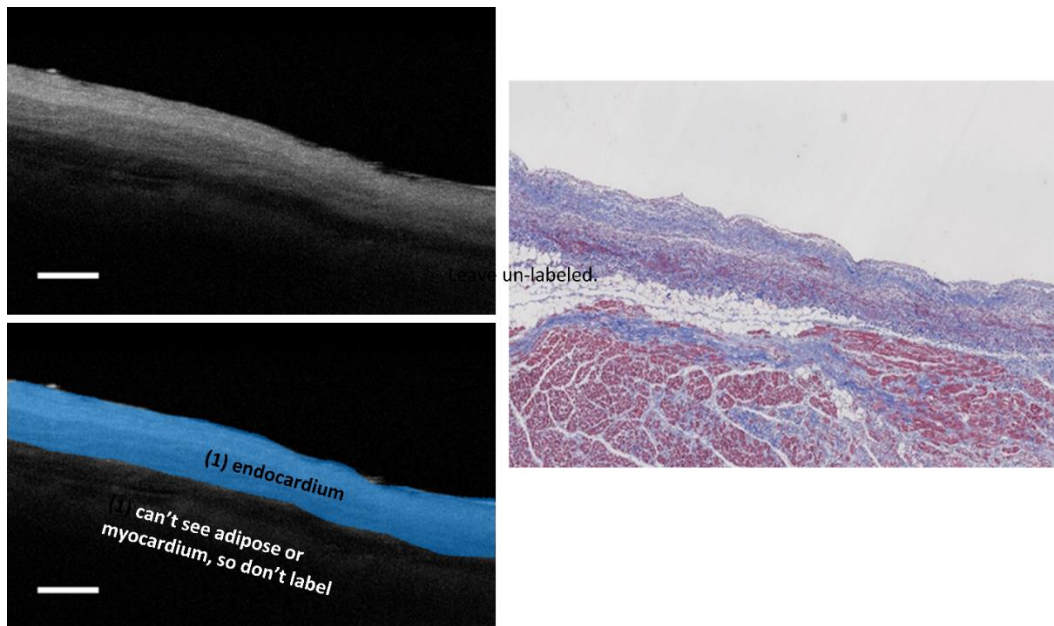

(14) *Blood Vessel*: Circular shape with darker intensity region seen with slightly brighter outline in OCT; circular shape seen in histology filled with smooth muscle or blood cells.
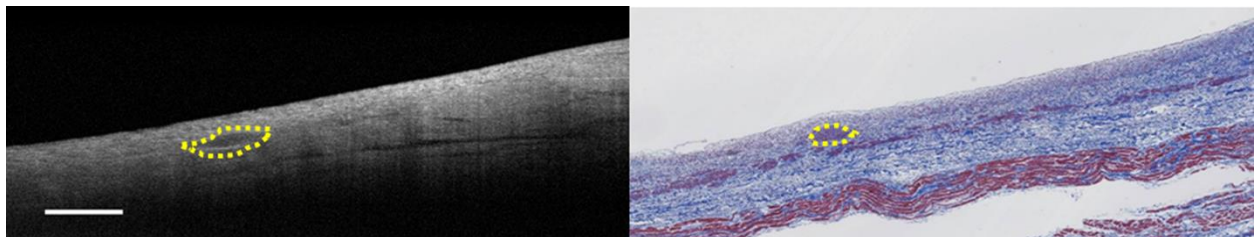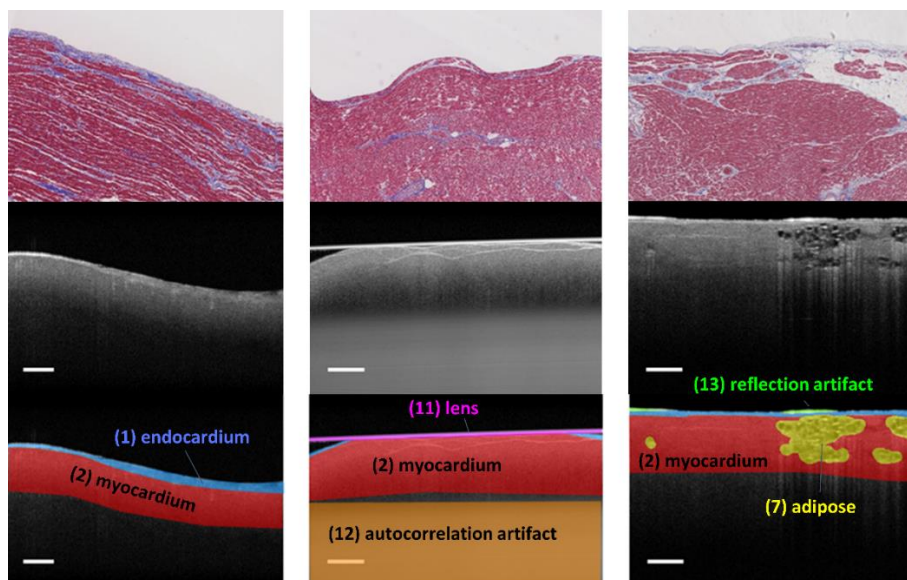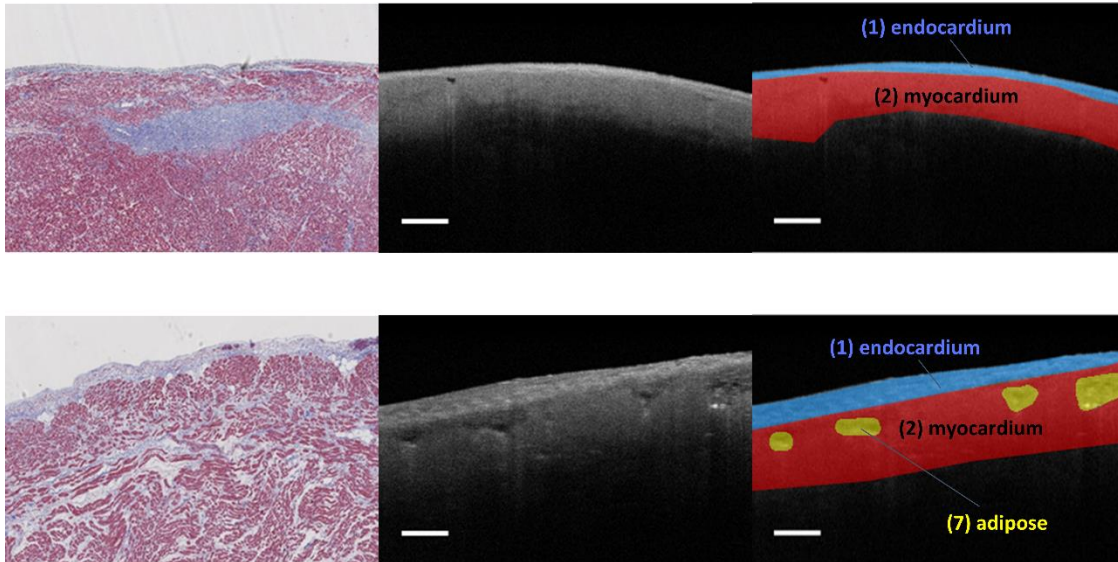
2. Example Segmentations and Notes

(**1**) Leave regions beyond the penetration depth un-labeled.
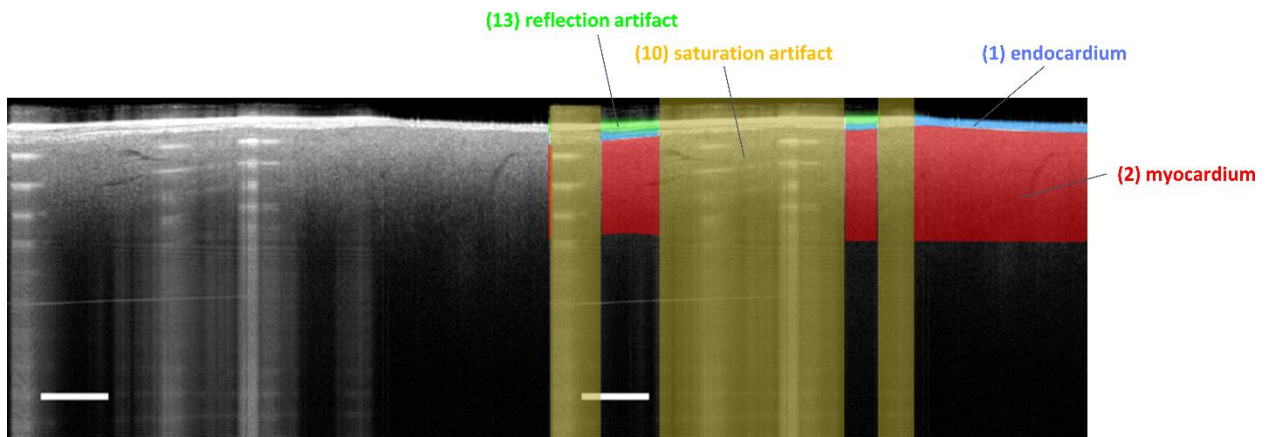

(**2**) If the fibrotic region is minor and does not cover the majority of the region, simply label as myocardium.

(3) If the fibrotic region appears to be beyond the imaging depth, do not label as fibrosis.

(4) Label artifacts lying on top of tissue regions as artifact.

Publications, Proceedings, Presentations, and Awards

1. Publications

[1] Theresa H. Lye, K. P. Vincent, A. D. McCulloch, and C. P. Hendon. 2018. Tissue-Specific Optical Mapping Models of Swine Atria Informed by Optical Coherence Tomography. Biophysical Journal 114:1477-1489.

[2] Theresa H. Lye, V. Iyer, C. C. Marboe, and C. P. Hendon. 2019. Mapping the human pulmonary venoatrial junction with optical coherence tomography. Biomed. Opt. Express 10:434-448.

[3] Y. Gan*, Theresa H. Lye*, C. C. Marboe, and C. P. Hendon, *indicates equal contribution. 2019. Characterization of the human myocardium by optical coherence tomography. Journal of Biophotonics. Under review.

[4] Theresa H. Lye, C. C. Marboe, and C. P. Hendon. 2019. Comprehensive Imaging of the Human Left Atrium with Optical Coherence Tomography. Under review.

[5] C. P. Hendon, Theresa H. Lye, X. Yao, Y. Gan, and C. C. Marboe. 2019. Optical Coherence Tomography Imaging of Cardiac Substrates. Advanced Optical Imaging in Biomedicine. Under review.

[6] J. P. McLean, Y. Gan, Theresa H. Lye, D. Qu, H. H. Lu, and C. P. Hendon. 2019. Computationally efficient collagen fiber modeling and orientation quantification for Optical Coherence Tomography imaging. Optics Express. Under review.

2. Conference Proceedings

[1] Y. Gan, Theresa H. Lye, X. Yao, C. C. Marboe, and C. P. Hendon, "Characterization of human endomyocardium using a human cardiac optical coherence tomography atlas," Biophotonics Congress: Biomedical Optics Congress 2018 (Microscopy/Translational/Brain/OTS) OSA Technical Digest (Optical Society of America, 2018), OTh2D.6, 2018. doi: 10.1364/OTS.2018.OTh2D.6. [Online]. Available: https://www.osapublishing.org/abstract.cfm?URI=OTS-2018-OTh2D.6.

[2] R. N. Rivas, Theresa H. Lye, and C. P. Hendon, "Impact of radiofrequency ablation geometry on electrical conduction," Proc. SPIE, vol. 10471, 2018. doi: 10.1117/12.2287917. [Online]. Available: https://doi.org/10.1117/12.2287917.

[3] Theresa H. Lye, Y. Gan, and C. P. Hendon, "Mapping the human atria with optical coherence tomography," Proc. SPIE, vol. 10042, 2017. doi: 10.1117/12.2251048. [Online]. Available: http://dx.doi.org/10.1117/12.2251048.

[4] Theresa H. Lye, K. P. Vincent, A. D. McCulloch, and C. P. Hendon, "Normal and radiofrequency ablated atrial models enabled by optical coherence tomography tissue characterization," Biomedical Optics 2016 OSA Technical Digest (Optical Society of America, 2016), OTh2B.3, 2016. doi: 10.1364/OTS.2016.OTh2B.3. [Online]. Available: http://www.osapublishing.org/abstract.cfm?URI=OTS-2016-OTh2B.3.

3. Conference Presentations

[1] Theresa H. Lye, Y. Gan, K. P. Vincent, A. D. McCulloch, and C. P. Hendon, "Comprehensive Mapping and Modeling of the Human Left Atrium with Optical Coherence

Tomography," in SPIE Photonics West BiOS, San Francisco, CA, Feb. 2019, Platform Presentation.

[2] Y. Gan, Theresa H. Lye, X. Yao, C. C. Marboe, and C. P. Hendon, "Cardiac optical coherence tomography atlas," in SPIE Photonics West BiOS, San Francisco, CA, Feb. 2019, Poster Presentation.

[3] Theresa H. Lye, V. Iyer, and C. P. Hendon, "Mapping Of Human Atrial-Pulmonary Vein Junctions With Optical Coherence Tomography," in Heart Rhythm, Boston, MA, May. 2018, Poster Presentation.

[4] Theresa H. Lye and C. P. Hendon, "Mapping the human left atrium and pulmonary veins with optical coherence tomography," in SPIE Photonics West BiOS, San Francisco, CA, Jan. 2018, Platform Presentation.

[5] Theresa H. Lye, K. P. Vincent, A. D. McCulloch, and C. P. Hendon, "Optical mapping models of human atria including heterogeneous tissue types as informed by optical coherence tomography," in SPIE Photonics West BiOS, San Francisco, CA, Jan. 2018, Platform Presentation.

[6] R. N. Rivas, Theresa H. Lye, and C. P. Hendon, "Impact of radiofrequency ablation geometry on electrical conduction," in SPIE Photonics West BiOS, San Francisco, CA, Jan. 2018, Platform Presentation.

[7] Theresa H. Lye, Y. Gan, and C. P. Hendon, "Mapping the human atria with optical coherence tomography," in SPIE Photonics West BiOS, San Francisco, CA, Jan. 2017, Platform Presentation.

[8] Theresa H. Lye, K. P. Vincent, A. D. McCulloch, and C. P. Hendon, "Optical mapping models of heterogeneous atria tissue informed by optical coherence tomography," in SPIE Photonics West BiOS, San Francisco, CA, Feb. 2017, Platform Presentation.

[9] Theresa H. Lye, K. P. Vincent, A. D. McCulloch, and C. P. Hendon, "Normal and radiofrequency ablated atrial models enabled by optical coherence tomography tissue characterization," in OSA Biomedical Optics Congress, Fort Lauderdale, FL, Apr. 2016, Platform Presentation.

[10] Theresa H. Lye, A. D. McCulloch, and C. P. Hendon, "Optical mapping models of the atria enabled by OCT tissue characterization," in SPIE Photonics West BiOS, San Francisco, CA, Feb. 2016, Platform Presentation.

[11] Theresa H. Lye and C. P. Hendon, "Atria models enabled by OCT tissue characterization," in Biomedical Engineering Society (BMES) Annual Meeting, Tampa, FL, Oct. 2015, Poster Presentation.

[12] Theresa H. Lye, V. Iyer, and C. P. Hendon, "Classification of atrial fibrillation and sinus rhythm with a Gaussian mixture model," in Biomedical Engineering Society (BMES) Annual Meeting, San Antonio, TX, Oct. 2014, Poster Presentation.

4. Awards

[1] Sheldon Weinig Scholar Award, 2016

[2] Honorable Mention, National Science Foundation Graduate Research Fellowship, 2014

[3] Columbia University SEAS Presidential Fellowship, 2013